CONSIDERATIONS FOR THE DESIGN OF GAS-LUBRICATED SLIDER BEARINGS

Thesis by

Paul Wesley Smith, Jr.

In Partial Fulfillment of the Requirements

for the Degree of

Doctor of Philosophy

California Institute of Technology

Pasadena, California

1988

(Submitted February 16, 1988)

ACKNOWLEDGEMENTS

My sincere gratitude goes to Professor W. D. Iwan, whose guidance, encouragement and friendship sustained me throughout my second graduate career.

Much of the software for the pressure contour plots in this thesis was written by G. V. Kelley, and the text was reviewed initially by C. N. Smith, whose help I sincerely appreciate. I am also indebted to the California Institute of Technology, the ARCS Foundation, and Applied Magnetics Corporation for their support of this research.

For sharing in an improbable dream, and for providing the patient, loving support to make it come true, I thank my wife, Maxine.

ABSTRACT

An approach is developed that simplifies calculation of the dynamic characteristics of a self-acting, gas-lubricated slider bearing system. This technique avoids a lengthy simultaneous solution of the equations of motion of the slider and the time-dependent Reynolds' equation, while providing additional design information that is otherwise unobtainable.

The equilibrium pressure distribution in the gas film is obtained using the Bunov-Galerkin formulation of the finite element method. By considering small perturbations of the slider bearing system about equilibrium, two coupled, second-order partial differential equations are derived, which define the in-phase and out-of-phase perturbation pressures in the gas film. These perturbation pressures are integrated to obtain the frequency dependent, non-symmetrical stiffness and damping matrices for the slider bearing.

Using the stiffness and damping properties of the gas bearing and slider support, the equations of motion for the entire slider bearing system are derived. The frequency dependence of the stiffness and damping matrices renders the eigenvalue problem nonlinear, and the eigensolutions are obtained iteratively using Brent's method.

Because of the non-symmetrical stiffness and damping matrices, a similarity transformation based on the left and right modal matrices is used to decouple the equations of motion. This decoupling is approximate because of the frequency dependence of the stiffness and damping matrices, but the resulting damped natural frequencies are shown to be in excellent agreement with published experimental data. Fractions of critical damping obtained for several slider geometries also successfully predict observed instabilities.

The mode shapes of slider oscillation, unobtainable with other methods, permit calculation of the center of rotation for the coupled, pitch-heave modes; this information can be used to determine the optimum location for the magnetic transducer. Closed-form solutions are obtained for the response to disk surface displacement, and for the response to a random force applied to the slider body. These forced-response solutions are useful in identifying the critical parameters of slider design.

TABLE OF CONTENTS

LIST OF FIGURES

NOMENCLATURE

ρ	gas density
μ	gas viscosity
u, v, w	localized gas velocity components
x, y, z	Cartesian coordinates
$h(x, y)$	film thickness distribution
$p(x, y)$	gas pressure distribution
l	dimension of slider bearing in y-direction
U	bulk gas velocity in y-direction
V	bulk gas velocity in x-direction
p_a	ambient pressure
h_m	minimum bearing clearance
ω	characteristic frequency
λ	ambient molecular mean free path
$h(X, Y, \tau)$	film thickness perturbation
$p(X, Y, \tau)$	gas pressure perturbation
$\hbar(X, Y)$	shape of film thickness perturbation
α, β, γ	film thickness perturbation parameters
$p_1(X, Y)$	in-phase gas pressure perturbation distribution
$p_2(X, Y)$	out-of-phase gas pressure perturbation distribution
$P_o(X, Y)$	normalized equilibrium pressure distribution
$H_o(X, Y)$	normalized equilibrium film thickness distribution
W	weighting functions for finite element solution
N	shape functions for finite element solution
H_i	normalized film thickness at inlet of gas bearing
ξ, η	parent element corrdinates
F	gas bearing force in z-direction
M_r	gas bearing moment about y-axis
M_p	gas bearing moment about x-axis
m	slider mass
I_p	slider moment of inertia about x-axis through center of mass
I_r	slider moment of inertia about y-axis through center of mass

$[C]$ damping matrix for complete slider bearing system

$[K]$ stiffness matrix for complete slider bearing system

$[C_s]$ damping matrix for gas bearing

$[K_s]$ stiffness matrix for gas bearing

$\{\xi\}$ slider displacement vector

$\{\gamma\}$ right eigenvector

$[G]$ right modal matrix

$\{\hat{\gamma}\}$ left eigenvector

$[\hat{G}]$ left modal matrix

CHAPTER 1

INTRODUCTION TO THE SLIDER BEARING PROBLEM

Modern computer systems depend on high-speed access to large volumes of stored information. Rotating disk memories, in which data are recorded magnetically, have kept pace with other computer technologies through periodic increases in areal storage density. For optimum data packing density on the disk surface, the spacing between the disk and magnetic transducer must be approximately the same as the distance between recorded transitions, or data bits. Increases in disk-drive performance have thus been accompanied by smaller spacing between the transducer and recording medium, higher relative speed, and a demand for greater dynamic stability.

Self-acting, gas-lubricated slider bearings are routinely used in disk drives to meet these requirements (see Figure 1.1). Such bearings are well-suited for maintaining the submicron spacings required. In this application, the dynamic stability of the slider bearing, on which the magnetic transducer is mounted, is critical; small variations in spacing can cause errors in information transfer, and large excursions may result ultimately in catastrophic data loss due to high-speed contact between slider and disk surface.

Air bearings were first used as a slider support system in the IBM RAMAC drive in 1953 (1,2). These bearings were pressurized by an external compressor and successfully maintained a spacing of 20 microns over disks with dynamic runout of up to 400 times that amount. Average access time, a measure of the slider's speed in locating a particular portion of data, was just under 1 second. The RAMAC drive was such a significant milestone in the evolution of electromechanical data storage that it was designated as an International Historic Landmark by the American Society of Mechanical Engineers in February, 1984 (3).

The designers of the next generation of disk drives sought to eliminate RAMAC's bulky and costly air compressor through the use of self-acting slider bearings. By contouring the slider to form a converging channel with the moving disk surface, a load- carrying pressure was formed without external sources. This change was a significant contributor to the economic success of disk-drive products that followed. In the ensuing years, disk memories have kept up with associated computer technologies by increasing data-packing densities more than three orders of magnitude. Transducer/media spacing has been reduced to less

FIGURE 1.1: BASIC SLIDER-BEARING SYSTEM

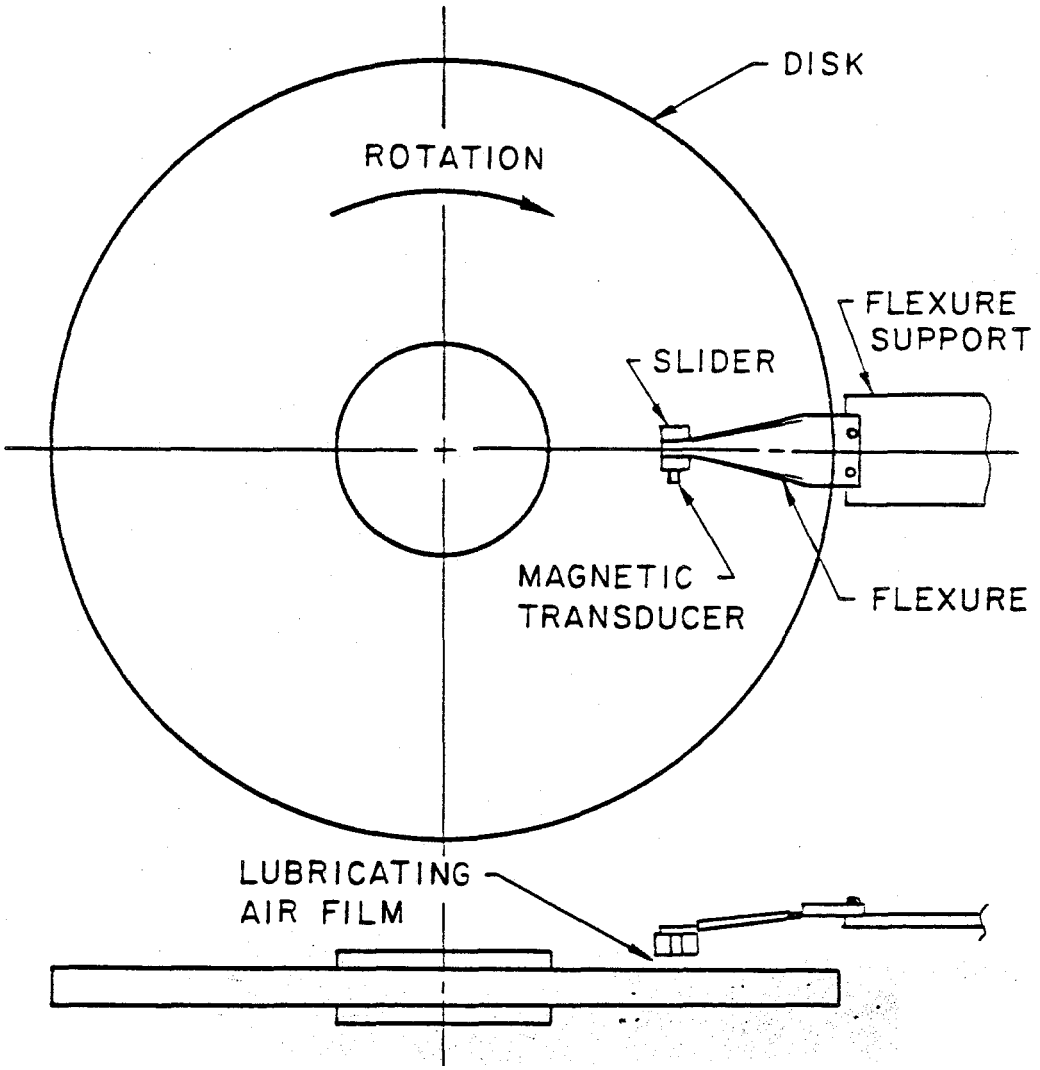

than .2 microns, and average access times of approximately 20 milliseconds are routine.

The key to future improvements in disk drive performance is the design of the gas-lubricated, self-acting slider bearing, and the associated dynamics of the slider and its suspension. While the compliance of the bearing determines the spacing variation between the transducer and the magnetic medium, its damping influences settling time, and hence the time required to access recorded information. Stiffness and damping are dependent on the frequency of relative motion between the slider and the disk, and thus are related to dynamic motion of the slider in a complex manner. Experimental optimization of slider-bearing performance would require expensive and tedious evaluation of many parameters; analytical and numerical techniques for computer-aided design offer the most economical path to enhanced performance.

The general topic of lubrication theory had its early roots in the work of Petroff (4), a 19th century Russian researcher, who made the crucial observation that the important fluid property was viscosity, not density as was previously thought. Petroff went on to show that frictional force was proportional to velocity, area, and viscosity, and inversely proportional to spacing. In 1883, Petroff's work was extended by Tower (5), whose experiments applied frictional concepts to the practical issue of bearing load-carrying capacity.

These early researchers provided the foundation for Reynolds (6), who, in 1886, contributed theory to what had previously been primarily an experimental science. In addition to the fundamental equation of lubrication theory bearing his name, Reynolds also showed that the "wedge effect," i.e., a converging channel between two surfaces in relative motion, was required to generate load-carrying capacity, and he developed important theoretical relationships between viscosity and temperature.

In 1897, Kingsbury (7) extended the theory of hydrodynamic lubrication to compressible fluids, noting that the lubricating medium could just as well be a gas as a liquid. Finally, in 1913, Harrison (8) used the perfect gas relation under isothermal conditions to write the compressible Reynolds equation in the form most widely used today.

The forces and moments acting on the slider because of the lubricant are determined by integrating the pressure within the lubricant. This pressure distribution obeys the Reynolds equation, a second-order, non-linear partial differential equation. Some of the earliest applications of the lubrication theory to self-acting, gas-lubricated slider bearings

are attributed to Gross (12,15) and Michael (13,16). Works by Castelli and Pirvics (20), and by Fuller (21), summarize the state of the art for air-bearing design through 1969. Significant contributions to this body of work were made by Elrod (14), Elrod and McCabe(22); Castelli and Stevenson (17); Coleman and Snyder (19); and Coleman (23). More recently, White and Nigam (27) have formulated improved solution techniques for the time-dependent Reynolds equation, and White (29) has published detailed analyses of current slider designs.

The dynamic measurement of submicron spacings presents an important and difficult challenge. Significant contributions to this technology were summarized in 1973 by Lin (60). Capacitance methods, which usually alter the slider dynamics slightly, were investigated by Brunner, et al. (57), and later by Briggs and Herkart (58). Measurement techniques based on optical interferometry, which involve substitution of a transparent member for either slider or disk, were reported by Lin and Sullivan (59); Sereny and Castelli (62); Fleischer and Lin (61); Nigam (63), and Hsia and Domoto (64). Capacitance and optical techniques were recently compared by Best (67). Efforts to develop an *in-situ* measurement technique that does not influence slider dynamics have led to the laser-doppler vibrometer, reported by Miu, et al. (65) and by Bouchard, et al. (66).

Dynamic analysis of a slider bearing requires simultaneous solution of the hydrodynamic lubricating film and the coupled, multidegree-of-freedom system represented by the slider and its suspension. Tang (33) was one of the first to solve simultaneously the time-dependent Reynolds equation and the equations of motion of the slider, and White (37,38), Bouchard, et al. (39), and Mizoshita, et al. (42) have recently refined this approach. Complete time-domain solutions, combined with laser-doppler measurements of slider response to disk surface imperfections, were reported by Miu (40). Frequency-domain solutions for forced response were first published by Ono (34), and subsequently extended by Ono, et al (35). A simplified version of this theory was used by Tagawa (36) to study yaw angle effects.

The preceding dynamical methods suffer from computational complexity; the slider equations of motion and the lubricating film equations must be solved simultaneously for many time steps. These methods also require some description of media surface motion as input. Neither time-domain nor frequency-domain analysis provides general insight into

the slider's dynamic behavior.

The approach presented in this thesis is based on a perturbation analysis of the lubricating film. Chapter 2 describes the perturbation method, and the finite element formulation used to solve the resulting sets of equations. Once the static solution has been found, the dynamic results are obtained directly, without iteration. This solution of the linearized form of the Reynolds equation provides stiffness and damping matrices which, in general, are non-symmetric and frequency-dependent. When assembled with stiffness and damping matrices for the slider suspension, they form the equations of motion for the slider. The solution of these equations, discussed in Chapter 3, provides estimates of effective, damped, natural frequencies, damping fractions, and mode shapes for the slider/bearing/suspension system. Using a similarity transform based on left and right modal matrices, the equations of motion are decoupled, and analytical expressions are developed for the response of a typical slider to some forcing functions of particular interest. Results obtained using this approach are compared with existing methods in Chapter 4 and then applied to some additional problems of current concern in slider design.

The approach developed in this thesis for treating slider dynamics provides an understanding of the nature of response, independent of the specific form of the forcing function. The damped natural frequencies are obtained directly, without performing a lengthy solution of the time-dependent Reynolds equation. Mode shapes, unobtainable with previously described methods, provide valuable design information, allowing the recording transducer to be located near a node to minimize spacing variations. Analytical solutions of the decoupled equations can be of great value in identifying and understanding the important parameters of slider design. These advantages are discussed in Chapter 5, as are the results obtained with the model, along with some recommendations for future investigations.

CHAPTER 2

ANALYSIS OF THE GAS-LUBRICATED BEARING

2.1 Reynolds' Equation

When two closely spaced surfaces are in relative motion, a pressure is generated in the entrained fluid. For a fixed volume of source-free fluid, over a specified interval of time, the mass of fluid entering this volume must equal the mass of fluid leaving plus the accumulated mass; that is,

$$\frac{\partial(\rho u)}{\partial x} + \frac{\partial(\rho v)}{\partial y} + \frac{\partial(\rho w)}{\partial z} + \frac{\partial \rho}{\partial t} = 0 \,. \tag{2.1}$$

Equation 2.1 represents the continuity expression for a compressible fluid. For most gas-lubricated slider bearings, the velocity in the plane of the bearing will be large compared with the normal velocity; i.e., $u, v \gg w$ (see Figure 2.1). Integrating 2.1 over the thickness of the lubricant film and interchanging the operations of integration and differentiation yield:

$$\frac{\partial}{\partial x}\int_0^h \rho u \, dz + \frac{\partial}{\partial y}\int_0^h \rho v \, dz + \frac{\partial}{\partial t}(\rho h) = 0 \,. \tag{2.2}$$

The velocity distributions required by Equation 2.2 are obtained from the momentum equations. Body forces, fluid inertia, and the variation in pressure in the vertical direction are generally neglected. Assuming a Newtonian fluid, the velocity gradient can be expressed as a linear function of shear. This leads to the following form for the momentum equations.

$$\frac{\partial p}{\partial x} = \frac{\partial}{\partial z}\left\{\mu \frac{\partial u}{\partial z}\right\} \tag{2.3}$$

$$\frac{\partial p}{\partial y} = \frac{\partial}{\partial z}\left\{\mu \frac{\partial v}{\partial z}\right\} \tag{2.4}$$

The ratio of the inertial to the viscous forces, or modified Reynolds number, determines the applicability of 2.3 and 2.4. This ratio is written as:

$$R_e^* = \rho \frac{lU}{\mu}\left(\frac{h}{l}\right)^2 \,. \tag{2.5}$$

When $R_e^* \ll 1$, viscous forces dominate, and 2.3 and 2.4 apply. For typical parameters of contemporary slider bearings, R_e^* is approximately .0001.

Unless the film velocity is extremely high, the thermally induced variations of density and viscosity are small enough that the bearing can be considered isothermal. The film

FIGURE 2.1: ANALYSIS OF THE LUBRICATING AIR FILM

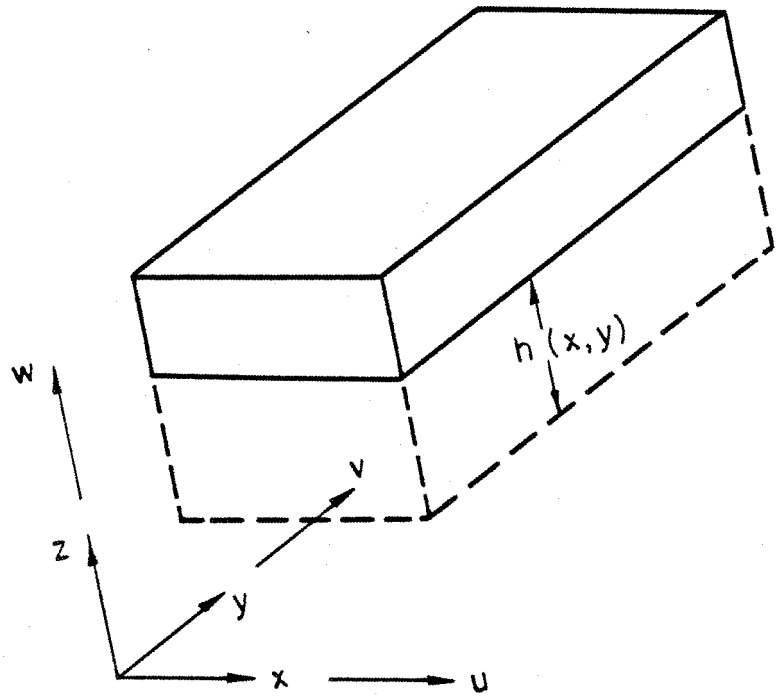

surface velocities will be identical to the velocities of the adjacent bearing surfaces unless slip is present. Assuming for the moment that slip is negligible, the boundary conditions for velocity are

$$\begin{aligned} u(x,y,0) &= u_1 \\ u(x,y,h) &= u_2 \\ v(x,y,0) &= v_1 \\ v(x,y,h) &= v_2 \\ w(x,y,0) &= w(x,y,h) = 0\,. \end{aligned} \tag{2.6}$$

Assuming constant viscosity, and subject to the above boundary conditions, the momentum Equations, 2.3 and 2.4, can be integrated across the film thickness to obtain the following velocity distributions.

$$u(x,y,z) = \left(u_1 - \frac{zh}{2\mu}\frac{\partial p}{\partial x}\right)\left(1-\frac{z}{h}\right) + \frac{u_2 z}{h} \tag{2.7}$$

$$v(x,y,z) = \left(v_1 - \frac{zh}{2\mu}\frac{\partial p}{\partial y}\right)\left(1-\frac{z}{h}\right) + \frac{v_2 z}{h} \tag{2.8}$$

If the bearing lubricant is assumed to be a perfect gas,

$$\frac{p}{\rho^n} = \text{constant} \tag{2.9}$$

where, under the assumption of isothermal conditions,

$$n = 1 \Rightarrow p \propto \rho\,. \tag{2.10}$$

Combining 2.7, 2.8, and 2.2 and performing the indicated integration, subject to 2.9 and 2.10, yield the familiar form of Reynolds' equation,

$$\frac{\partial}{\partial x}\left(ph^3\frac{\partial p}{\partial x}\right) + \frac{\partial}{\partial y}\left(ph^3\frac{\partial p}{\partial y}\right) = 12\mu\frac{\partial(ph)}{\partial t} + 6\mu U\frac{\partial(ph)}{\partial y} + 6\mu V\frac{\partial(ph)}{\partial x}\,, \tag{2.11}$$

where

$$\begin{aligned} U &= u_1 + u_2\,; \qquad U \neq f(x,y) \\ V &= v_1 + v_2\,; \qquad V \neq f(x,y) \end{aligned} \tag{2.12}$$

Reynolds' Equation 2.11 is customarily written in non-dimensional form so that the

relative size of the terms can be readily estimated. Let

$$\begin{aligned} P &= \frac{p}{p_a} \\ H &= \frac{h}{h_m} \\ X &= \frac{x}{l} \\ Y &= \frac{y}{l} \\ \tau &= \omega t \end{aligned} \qquad (2.13)$$

The non-dimensional form of the Reynolds equation resulting from 2.13 and 2.11 is a second-order, non-linear partial differential equation,

$$\frac{\partial}{\partial X}\left(PH^3\frac{\partial P}{\partial X}\right)+\frac{\partial}{\partial Y}\left(PH^3\frac{\partial P}{\partial Y}\right)=\sigma\frac{\partial(PH)}{\partial \tau}+\Lambda_y\frac{\partial(PH)}{\partial Y}+\Lambda_x\frac{\partial(PH)}{\partial X}\,, \qquad (2.14)$$

where

$$\Lambda_x = \frac{6\mu V l}{p_a h_m^2} \qquad (2.15)$$

$$\Lambda_y = \frac{6\mu U l}{p_a h_m^2} \qquad (2.16)$$

$$\sigma = \frac{12\mu\omega l^2}{p_a h_m^2}\,. \qquad (2.17)$$

Although the film velocities have been assumed equal to the adjacent bearing surface velocities, such is not always the case. As spacings become small, the continuum flow hypothesis weakens as the average molecular velocity at a surface begins to differ from the surface velocity. This phenomenon is known as slip flow, and is more pronounced for very smooth surfaces. For extremely small spacings, fully developed molecular flow will occur. These various flow regimes are governed by the Knudsen number, K_n.

$$K_n = \frac{\lambda}{h} \qquad (2.18)$$

Slip flow becomes significant when the Knudsen number falls in the range $.01 < K_n < 15$. For Knudsen numbers below .01, continuum flow assumptions are valid, while fully developed molecular flow is expected when $K_n > 15$. Since the mean-free path in air at room temperature is less than .1 micron, most modern slider bearings will require slip-flow correction.

The treatment attributed to Burgdorfer (51) is commonly used as a first approximation for slip at the boundary. This problem has also been studied by Tseng (52), Sereny and Castelli (53), and Mitsuya (54). Gans (55) has used the kinetic theory of gases to show the efficacy of Burgdorfer's correction at arbitrary Knudsen number, and Mitsuya and Ohkubo (56) performed experiments that support Gans' work.

Burgdorfer assumes the following form for the velocity at the wall:

$$U_{\text{wall}} = f(\lambda)\left.\frac{dU}{dy}\right|_{\text{wall}}, \tag{2.19}$$

where

$$f(\lambda) = \left(\frac{2-r}{r}\right)\lambda\,. \tag{2.20}$$

With r = 1 for diffuse reflection,

$$U_{\text{wall}} = \lambda\left.\frac{dU}{dy}\right|_{\text{wall}}. \tag{2.21}$$

Combining 2.21 with 2.14 leads to the modified Reynolds equation

$$\begin{aligned}\frac{\partial}{\partial X}\left\{PH^3\left(1+\frac{6K_n}{PH}\right)\frac{\partial P}{\partial X}\right\} + \frac{\partial}{\partial Y}\left\{PH^3\left(1+\frac{6K_n}{PH}\right)\frac{\partial P}{\partial Y}\right\} \\ = \Lambda_x\frac{\partial(PH)}{\partial X} + \Lambda_y\frac{\partial(PH)}{\partial Y} + \sigma\frac{\partial(PH)}{\partial \tau}\,.\end{aligned} \tag{2.22}$$

The modified Equation 2.22 predicts lower load-carrying capacity than 2.14, especially at low bearing numbers and close spacing.

Most existing computer codes solve 2.22 using the finite difference technique combined with either explicit, implicit, or semi-implicit algorithms for the time domain. Present-day slider bearings require relatively small spatial discretization because of the presence of high-pressure gradients. Since the maximum time increment in the explicit method is constrained by the square of the smallest spatial increment, explicit methods require large amounts of computer time. The implicit method, on the other hand, requires the solution of a system of equations at each time step and thus entails significant computational effort. Alternating direction, or semi-implicit techniques, combine the best features of both explicit and implicit schemes, but have been shown by Coleman (23) to cause phase shifts in the dynamical solution that inhibit accurate estimation of bearing stability.

The factored-implicit technique, developed by White and Nigam (27), is a second-order, time-accurate, finite difference scheme that reduces this phase-shifting problem. This algorithm has been used by many recent researchers, including Miu (40), who compared his dynamical calculations with experimental data from a laser-doppler vibrometer. While he found "little resemblance" between the calculated slider motions and the experimental data, Miu did discover correlation in the frequency spectra, and was able to identify experimentally two pitch-heave modes, as well as an uncoupled roll mode, of slider oscillation.

2.2 Perturbation Equations

For slider bearings used in magnetic recording, the dynamic behavior about equilibrium is the most critical factor, and this suggests that the above numerical problems might be avoided with a linearized perturbation approach. Let the normalized film thickness and the normalized pressure in the film consist of an equilibrium value plus a small, linear, time-dependent perturbation as follows: (Perturbation frequency is assumed real. See Section 3.3.)

$$H(X,Y,\tau) = H_o(X,Y) + h(X,Y,\tau) \tag{2.23}$$

$$P(X,Y,\tau) = P_o(X,Y) + p(X,Y,\tau)\,, \tag{2.24}$$

where H_o and P_o satisfy

$$\begin{aligned}\frac{\partial}{\partial X}\left\{P_o H_o^3\left(1+\frac{6K_n}{P_o H_o}\right)\frac{\partial P_o}{\partial X}\right\} + \frac{\partial}{\partial Y}\left\{P_o H_o^3\left(1+\frac{6K_n}{P_o H_o}\right)\frac{\partial P_o}{\partial Y}\right\} \\ = \Lambda_x\frac{\partial(P_o H_o)}{\partial X} + \Lambda_y\frac{\partial(P_o H_o)}{\partial Y}\,,\end{aligned} \tag{2.25}$$

and h and p have the form

$$h(X,Y,\tau) = \hbar(X,Y)\sin\tau \tag{2.26}$$

$$\hbar(X,Y) = \alpha + \beta(X_o - X) + \gamma(Y_o - Y) \tag{2.27}$$

$$p(X,Y,\tau) = p_1(X,Y)\sin\tau + p_2(X,Y)\cos\tau\,. \tag{2.28}$$

Thus, a small change in film thickness, $h(X,Y)$, results in a corresponding change of pressure, $p(X,Y)$, consisting of both an in-phase $[p_1(X,Y)]$ and an out-of-phase $[p_2(X,Y)]$ component. Substituting 2.26 and 2.28 into 2.22, and noting that the relationship in 2.25 is identically satisfied by H_o and P_o by definition, the sine and cosine terms can be collected

to give two coupled, second-order, linear, partial differential equations for $p_1(X,Y)$ and $p_2(X,Y)$.

$$\begin{aligned}
&\frac{\partial^2 p_1}{\partial X^2}+\frac{\partial^2 p_1}{\partial Y^2}+\mathbf{K}\Bigg[\left\{2H_o\frac{\partial P_o}{\partial X}+\frac{3}{H_o}\frac{\partial H_o}{\partial X}(4K_n+P_oH_o)-\frac{\Lambda_x}{H_o}\right\}\frac{\partial p_1}{\partial X}\\
&\quad+\left\{2H_o\frac{\partial P_o}{\partial Y}+\frac{3}{H_o}\frac{\partial H_o}{\partial Y}(4K_n+P_oH_o)-\frac{\Lambda_y}{H_o}\right\}\frac{\partial p_1}{\partial Y}\\
&\quad+\left\{H_o\left(\frac{\partial^2 P_o}{\partial X^2}+\frac{\partial^2 P_o}{\partial Y^2}\right)+3\left(\frac{\partial P_o}{\partial X}\frac{\partial H_o}{\partial X}+\frac{\partial P_o}{\partial Y}\frac{\partial H_o}{\partial Y}\right)\right.\\
&\quad\left.-\frac{\Lambda_y}{H_o^2}\frac{\partial H_o}{\partial Y}-\frac{\Lambda_x}{H_o^2}\frac{\partial H_o}{\partial X}\right\}p_1\\
&\quad+3\left\{\left(P_o+\frac{4K_n}{H_o}\right)\left(\frac{\partial^2 P_o}{\partial X^2}+\frac{\partial^2 P_o}{\partial Y^2}\right)+\left(\frac{\partial P_o}{\partial X}\right)^2+\left(\frac{\partial P_o}{\partial Y}\right)^2\right.\\
&\quad+\frac{2}{H_o}\left(P_o+\frac{2K_n}{H_o}\right)\left(\frac{\partial P_o}{\partial X}\frac{\partial H_o}{\partial X}+\frac{\partial P_o}{\partial Y}\frac{\partial H_o}{\partial Y}\right)-\frac{\Lambda_x}{3H_o^2}\frac{\partial P_o}{\partial X}-\frac{\Lambda_y}{3H_o^2}\frac{\partial P_o}{\partial Y}\Bigg\}\hbar\\
&\quad-\frac{3}{H_o}(4K_n+P_oH_o)\left(\beta\frac{\partial P_o}{\partial X}+\gamma\frac{\partial P_o}{\partial Y}\right)+\frac{P_o}{H_o^2}(\beta\Lambda_x+\gamma\Lambda_y)+\frac{\sigma p_2}{H_o}\Bigg]=0
\end{aligned}\tag{2.29}$$

$$\begin{aligned}
&\frac{\partial^2 p_2}{\partial X^2}+\frac{\partial^2 p_2}{\partial Y^2}+\mathbf{K}\Bigg[\left\{2H_o\frac{\partial P_o}{\partial X}+\frac{3}{H_o}\frac{\partial H_o}{\partial X}(4K_n+P_oH_o)-\frac{\Lambda_x}{H_o}\right\}\frac{\partial p_2}{\partial X}\\
&\quad+\left\{2H_o\frac{\partial P_o}{\partial Y}+\frac{3}{H_o}\frac{\partial H_o}{\partial Y}(4K_n+P_oH_o)-\frac{\Lambda_y}{H_o}\right\}\frac{\partial p_2}{\partial Y}\\
&\quad+\left\{H_o\left(\frac{\partial^2 P_o}{\partial X^2}+\frac{\partial^2 P_o}{\partial Y^2}\right)+3\left(\frac{\partial P_o}{\partial X}\frac{\partial H_o}{\partial X}+\frac{\partial P_o}{\partial Y}\frac{\partial H_o}{\partial Y}\right)\right.\\
&\quad\left.-\frac{\Lambda_x}{H_o^2}\frac{\partial H_o}{\partial X}-\frac{\Lambda_y}{H_o^2}\frac{\partial H_o}{\partial Y}\right\}p_2-\frac{\sigma}{H_o^2}(p_1H_o+\hbar P_o)\Bigg]=0\,,
\end{aligned}\tag{2.30}$$

where

$$\mathbf{K}(P_o,H_o)=\frac{1}{(6K_n+P_oH_o)}\,.$$

The solution of Equations 2.29 and 2.30 involves first solving Equation 2.25 for the equilibrium pressure distribution $P_o(X,Y)$ as a function of $H_o(X,Y)$. This solution is then used in solving for $p_1(X,Y)$ and $p_2(X,Y)$. The nominal pressure distribution $P_o(X,Y)$ can be integrated to obtain the forces and moments acting on the slider, while the perturbation pressures $p_1(X,Y)$ and $p_2(X,Y)$ are used to compute the linearized stiffness and damping matrices for the slider bearing.

When the slider undergoes a small displacement $\hbar$, defined by Equation 2.27, there is a corresponding small change in pressure which, when integrated over the bearing surface,

results in a small change in loading. By properly selecting α, β, γ, X_o and Y_o in Equation 2.27, it is thus possible to compute a change in force per unit displacement. This represents the linearized dynamic stiffness of the gas bearing. Similar computations of change in force per unit velocity provide an estimate of the linearized dynamic damping coefficients. Applying this procedure for the appropriate forces, displacements, and velocities permits the formulation of the complete stiffness and damping matrices for the slider bearing.

2.3 Finite Element Solution

In order to deal with a smoother dependent variable, a technique referred to as "natural linearization" is employed prior to attempting a solution of 2.25. This renders the pressure flow terms linear, while transferring the non-linearity to the shear flow terms in the form of $\sqrt{Q_o}$. Let the new dependent variable, Q_o, be defined as follows:

$$Q_o = P_o^2 H_o^2 \,. \tag{2.31}$$

Combining 2.31 and 2.25 leads to the following equation for $Q_o(X,Y)$:

$$\frac{\partial^2 Q_o}{\partial X^2} + \frac{\partial^2 Q_o}{\partial Y^2} - \frac{2Q_o}{H_o}\left(\frac{\partial^2 H_o}{\partial X^2} + \frac{\partial^2 H_o}{\partial Y^2}\right) - \frac{3K_n\, C(Q_o)}{Q_o\sqrt{Q_o}}\left\{\left(\frac{\partial Q_o}{\partial X}\right)^2 + \left(\frac{\partial Q_o}{\partial Y}\right)^2\right\}$$
$$- \frac{C(Q_o)}{H_o}\left\{\frac{\partial Q_o}{\partial X}\frac{\partial H_o}{\partial X} + \frac{\partial Q_o}{\partial Y}\frac{\partial H_o}{\partial Y}\right\} = \frac{2C(Q_o)}{H_o}\left(\Lambda_x \frac{\partial\sqrt{Q_o}}{\partial X} + \Lambda_y \frac{\partial\sqrt{Q_o}}{\partial Y}\right), \tag{2.32}$$

where

$$C(Q_o) = \frac{1}{1 + \dfrac{6K_n}{\sqrt{Q_o}}} \,.$$

The Knudsen number, K_n, is usually quite small compared with the bearing number Λ; hence, the non-linearity will be dominated by the Λ terms. The terms involving K_n are therefore linearized by using the value of Q_o from the previous iteration, while for the Λ terms, the dependent variable is expanded using the incremental form of Taylor's series.

$$Q_o^n = Q_o^{n-1} + \Delta Q_o \tag{2.33}$$

n = iteration count

Thus,

$$\sqrt{Q_o} \approx \frac{\sqrt{Q_o^{n-1}}}{2} + \frac{Q_o^n}{2\sqrt{Q_o^{n-1}}} \tag{2.34}$$

and

$$\frac{\partial\sqrt{Q_o}}{\partial Y} \approx \frac{1}{4\sqrt{Q_o^{n-1}}}\frac{\partial Q_o^{n-1}}{\partial Y} + \frac{1}{2\sqrt{Q_o^{n-1}}}\frac{\partial Q_o^{n}}{\partial Y} - \frac{Q_o^n}{4(Q_o^{n-1})^{3/2}}\frac{\partial Q_o^{n-1}}{\partial Y} \,. \tag{2.35}$$

Substituting 2.35 into 2.32 results in

$$\begin{aligned}\frac{\partial^2 Q_o}{\partial X^2} + \frac{\partial^2 Q_o}{\partial Y^2} - \frac{C(\bar{Q}_o)}{H_o}\left(\frac{\partial Q_o}{\partial X}\frac{\partial H_o}{\partial X} + \frac{\partial Q_o}{\partial Y}\frac{\partial H_o}{\partial Y}\right) - \frac{2Q_o}{H_o}\left(\frac{\partial^2 H_o}{\partial X^2} + \frac{\partial^2 H_o}{\partial Y^2}\right) \\ - \frac{3K_n C(\bar{Q}_o)}{\bar{Q}_o^{3/2}}\left\{\left(\frac{\partial \bar{Q}_o}{\partial X}\right)^2 + \left(\frac{\partial \bar{Q}_o}{\partial Y}\right)^2\right\} - \frac{C(\bar{Q}_o)}{H_o\sqrt{\bar{Q}_o}}\left(\Lambda_x\frac{\partial Q_o}{\partial X} + \Lambda_y\frac{\partial Q_o}{\partial Y}\right) \\ + \frac{C(\bar{Q}_o)}{2H_o\sqrt{\bar{Q}_o}}\left(\frac{Q_o}{\bar{Q}_o} - 1\right)\left(\Lambda_x\frac{\partial \bar{Q}_o}{\partial X} + \Lambda_y\frac{\partial \bar{Q}_o}{\partial Y}\right) = 0\end{aligned} \tag{2.36}$$

where

$$Q_o = Q_o^n$$
$$\bar{Q}_o = Q_o^{n-1}$$

The finite element method was chosen for the solution of 2.32, with the hope that it would provide better convergence for modern slider bearings which typically contain high pressure gradients. The capabilities of fitting curved boundaries, and of creating non-rectangular meshes, also offer some advantages when modeling certain slider geometries.

Using the Galerkin approach, the strong form of the weighted residual formulation for Equation 2.36 is written as:

$$\begin{aligned}\int_\nu W\Bigg[\frac{\partial^2 Q_o}{\partial X^2} + \frac{\partial^2 Q_o}{\partial Y^2} - \frac{C(\bar{Q})_o}{H_o}\left(\frac{\partial Q_o}{\partial X}\frac{\partial H_o}{\partial X} + \frac{\partial Q_o}{\partial Y}\frac{\partial H_o}{\partial Y}\right) - \frac{2Q_o}{H_o}\left(\frac{\partial^2 H_o}{\partial X^2} + \frac{\partial^2 H_o}{\partial Y^2}\right) \\ - \frac{3K_n C(\bar{Q}_o)}{\bar{Q}_o^{3/2}}\left\{\left(\frac{\partial \bar{Q}_o}{\partial X}\right)^2 + \left(\frac{\partial \bar{Q}_o}{\partial Y}\right)^2\right\} - \frac{C(\bar{Q}_o)}{H_o\sqrt{\bar{Q}_o}}\left(\Lambda_x\frac{\partial Q_o}{\partial X} + \Lambda_y\frac{\partial Q_o}{\partial Y}\right) \\ + \frac{C(\bar{Q}_o)}{2H_o\sqrt{\bar{Q}_o}}\left(\frac{Q_o}{\bar{Q}_o} - 1\right)\left(\Lambda_x\frac{\partial \bar{Q}_o}{\partial X} + \Lambda_y\frac{\partial \bar{Q}_o}{\partial Y}\right)\Bigg] d\nu = 0 \,.\end{aligned} \tag{2.37}$$

In the Bunov-Galerkin approach, where the weighting and shape functions are the same, it is advantageous to balance derivative orders, and hence continuity requirements, for the terms. To do this in Equation 2.37, Green's theorem is applied to the terms involving second derivatives of Q_o and H_o. The resulting weak form of the weighted residual

formulation is given in Equation 2.38.

$$\int_{\nu} \left[\frac{\partial W}{\partial X}\frac{\partial Q_o}{\partial X} + \frac{\partial W}{\partial Y}\frac{\partial Q_o}{\partial Y} + \frac{W}{H_o}\left(C(\bar{Q}_o)-2\right)\left(\frac{\partial Q_o}{\partial X}\frac{\partial H_o}{\partial X} + \frac{\partial Q_o}{\partial Y}\frac{\partial H_o}{\partial Y}\right) \right.$$
$$- \frac{2Q_o}{H_o}\left(\frac{\partial W}{\partial X}\frac{\partial H_o}{\partial X} + \frac{\partial W}{\partial Y}\frac{\partial H_o}{\partial Y}\right) + \frac{2WQ_o}{H_o^2}\left\{\left(\frac{\partial H_o}{\partial X}\right)^2 + \left(\frac{\partial H_o}{\partial Y}\right)^2\right\}$$
$$+ \frac{3K_nC(\bar{Q}_o)W}{\bar{Q}_o^{3/2}}\left\{\left(\frac{\partial \bar{Q}_o}{\partial X}\right)^2 + \left(\frac{\partial \bar{Q}_o}{\partial Y}\right)^2\right\} + \frac{WC(\bar{Q}_o)}{H_o\sqrt{\bar{Q}_o}}\left(\Lambda_x\frac{\partial Q_o}{\partial X} + \Lambda_y\frac{\partial Q_o}{\partial Y}\right) \qquad (2.38)$$
$$\left. + \frac{WC(\bar{Q}_o)}{2H_o\sqrt{\bar{Q}_o}}\left(1-\frac{Q_o}{\bar{Q}_o}\right)\left(\Lambda_x\frac{\partial \bar{Q}_o}{\partial X} + \Lambda_y\frac{\partial \bar{Q}_o}{\partial Y}\right)\right] d\nu = 0$$

The domain ν, comprising the area under the slider exclusive of the boundary, is now divided into individual subdomains or elements. The value of the dependent variable Q_o within an element is denoted by Q_o^e. In the finite element approximation, Q_o^e is expressed in terms of its nodal values, and the shape functions N^e, as follows:

$$Q_o^e \approx \langle N^e \rangle \{Q_o^e\} . \qquad (2.39)$$

For simplicity, the shape functions are also used as weighting functions; i.e.,

$$W^e = {}^iW^e = \sum\nolimits^{e_i} N_i^e . \qquad (2.40)$$

Combining 2.38, 2.39, and 2.40 results in the following equation for node i, not on B_{Q_o}:

$$\sum\nolimits^{e_i} \left\{ \int_{\nu^e} \left(\frac{\partial N_i^e}{\partial X}\left\langle\frac{\partial N^e}{\partial X}\right\rangle\{Q_o^e\} + \frac{\partial N_i^e}{\partial Y}\left\langle\frac{\partial N^e}{\partial Y}\right\rangle\{Q_o^e\}\right.\right.$$
$$+ \frac{1}{H_o}\left(C(\bar{Q}_o)-2\right)\left(\frac{\partial H_o}{\partial X}N_i^e\left\langle\frac{\partial N^e}{\partial X}\right\rangle\{Q_o^e\} + \frac{\partial H_o}{\partial Y}N_i^e\left\langle\frac{\partial N^e}{\partial Y}\right\rangle\{Q_o^e\}\right)$$
$$+ \frac{2}{H_o}\frac{\partial H_o}{\partial X}\left(\frac{1}{H_o}\frac{\partial H_o}{\partial X}N_i^e\langle N^e\rangle\{Q_o^e\} - \frac{\partial N_i^e}{\partial X}\langle N^e\rangle\{Q_o^e\}\right)$$
$$+ \frac{2}{H_o}\frac{\partial H_o}{\partial Y}\left(\frac{1}{H_o}\frac{\partial H_o}{\partial Y}N_i^e\langle N^e\rangle\{Q_o^e\} - \frac{\partial N_i^e}{\partial Y}\langle N^e\rangle\{Q_o^e\}\right)$$
$$+ \frac{3K_nC(\bar{Q}_o)}{\bar{Q}_o^{3/2}}\left\{\left(\frac{\partial \bar{Q}_o}{\partial X}\right)^2 + \left(\frac{\partial \bar{Q}_o}{\partial Y}\right)^2\right\}N_i^e \qquad (2.41)$$
$$+ \frac{C(\bar{Q})}{H_o\sqrt{\bar{Q}}}\left(\Lambda_xN_i^e\left\langle\frac{\partial N^e}{\partial X}\right\rangle\{Q_o^e\} + \Lambda_yN_i^e\left\langle\frac{\partial N^e}{\partial Y}\right\rangle\{Q_o^e\}\right)$$
$$- \frac{C(\bar{Q}_o)}{2H_o\bar{Q}_o^{3/2}}\left(\Lambda_x\frac{\partial \bar{Q}_o}{\partial X} + \Lambda_y\frac{\partial \bar{Q}_o}{\partial Y}\right)N_i^e\langle N^e\rangle\{Q_o^e\}$$
$$\left.\left. + \frac{C(\bar{Q}_o)}{2H_o\sqrt{\bar{Q}_o}}\left(\Lambda_x\frac{\partial \bar{Q}_o}{\partial X} + \Lambda_y\frac{\partial \bar{Q}_o}{\partial Y}\right)N_i^e\right) d\nu^e \right\} = 0 ,$$

where Q_o^e and ${}^iW^e$ must be C^o continuous within elements as well as between them.

Equation 2.41 can be written in the form

$$[K^e]\{Q_o^e\} = \{f_{Q_o}^e\} + \{F^e\}\,, \tag{2.42}$$

where

$$\begin{aligned}[K^e] = \int_{-1}^{1}\int_{-1}^{1} \Bigg[& \left\{\frac{\partial N^e}{\partial X}\right\}\left\langle\frac{\partial N^e}{\partial X}\right\rangle + \left\{\frac{\partial N^e}{\partial Y}\right\}\left\langle\frac{\partial N^e}{\partial Y}\right\rangle \\ & + \frac{1}{H_o}(C(\bar{Q}_o)-2)\left(\frac{\partial H_o}{\partial X}\{N^e\}\left\langle\frac{\partial N^e}{\partial X}\right\rangle + \frac{\partial H_o}{\partial Y}\{N^e\}\left\langle\frac{\partial N^e}{\partial Y}\right\rangle\right) \\ & + \frac{2}{H_o}\frac{\partial H_o}{\partial X}\left(\frac{1}{H_o}\frac{\partial H_o}{\partial X}\{N^e\}\langle N^e\rangle - \left\{\frac{\partial N^e}{\partial X}\right\}\langle N^e\rangle\right) \\ & + \frac{2}{H_o}\frac{\partial H_o}{\partial Y}\left(\frac{1}{H_o}\frac{\partial H_o}{\partial Y}\{N^e\}\langle N^e\rangle - \left\{\frac{\partial N^e}{\partial Y}\right\}\langle N^e\rangle\right) \\ & + \frac{C(\bar{Q}_o)}{H_o\sqrt{\bar{Q}_o}}\left\{\Lambda_x\{N^e\}\left\langle\frac{\partial N^e}{\partial X}\right\rangle + \Lambda_y\{N^e\}\left\langle\frac{\partial N^e}{\partial Y}\right\rangle\right. \\ & \left. - \frac{1}{2\bar{Q}_o}\left(\Lambda_x\frac{\partial\bar{Q}_o}{\partial X} + \Lambda_y\frac{\partial\bar{Q}_o}{\partial Y}\right)\{N^e\}\langle N^e\rangle\right\}\Bigg]\det[J]\,d\xi\,d\eta \end{aligned} \tag{2.43}$$

$$\begin{aligned}\{F^e\} = -\int_{-1}^{1}\int_{-1}^{1} \Bigg[& \frac{C(\bar{Q}_o)}{2H_o\sqrt{\bar{Q}_o}}\left(\Lambda_y\frac{\partial\bar{Q}_o}{\partial Y} + \Lambda_x\frac{\partial\bar{Q}_o}{\partial X}\right) \\ & + \frac{3K_nC(\bar{Q}_o)}{\bar{Q}_o^{3/2}}\left\{\left(\frac{\partial\bar{Q}_o}{\partial X}\right)^2 + \left(\frac{\partial\bar{Q}_o}{\partial Y}\right)^2\right\}\Bigg]\{N^e\}\,\det[J]\,d\xi\,d\eta \end{aligned} \tag{2.44}$$

$$\{f_{Q_o}^e\} = -[K^e]\,\{\text{ vector of zeroes and specified } Q_o \text{ values }\}\,. \tag{2.45}$$

In the above equations, $\det[J]$ is the Jacobian determinant for the mapping between parent and actual elements, and ξ and η are the coordinates in the parent element.

Solving 2.42 involves computing 2.43, 2.44, and 2.45, all of which depend on an initial guess for $\bar{Q}_o$. There are two extremes of bearing behavior that can be used to help bound such a guess. The first is the low bearing number limit where Λ approaches zero, and the film pressure becomes uniform and equal to the ambient pressure; i.e., $P_o(X,Y) = 1.0$. This results in a first guess for Q_o of

$$Q_o(X,Y) = H_o^2(X,Y)\,. \tag{2.46}$$

The second case, where the bearing number becomes infinitely large, more closely approximates the pressure distribution of sliders currently in use. The limiting solution for an infinite bearing number is given by

$$P_o(X,Y) = \frac{H_i}{H_o(X,Y)} \; ; \qquad Q_o(X,Y) = H_i^2 \; . \tag{2.47}$$

This latter expression is used as a first guess for the solutions computed in this thesis.

Evaluation of 2.43, 2.44, and 2.45 requires integration over the parent element. The elements chosen for the solution of 2.41 are 8-node, isoparametric elements, Figure 2.2, and integrations are performed numerically using 9-point Gaussian quadrature.

Having computed the equilibrium pressure solution, $P_o(X,Y)$, Equations 2.29 and 2.30 can now be solved for p_1 and p_2. Although these equations are coupled, it is possible to avoid iteration by formulating a simultaneous, partitioned solution for p_1 and p_2. Using the finite element method, the equations are first rewritten as follows:

$$\begin{aligned}
\int_{\nu^e} \Bigg[& \left\{\frac{\partial N^e}{\partial X}\right\} \left\langle \frac{\partial N^e}{\partial X} \right\rangle \{p_1^e\} + \left\{\frac{\partial N^e}{\partial Y}\right\} \left\langle \frac{\partial N^e}{\partial Y} \right\rangle \{p_1^e\} + \mathcal{F}_1\{N^e\} \left\langle \frac{\partial N^e}{\partial X} \right\rangle \{p_1^e\} \\
& + \mathcal{F}_2\{N^e\} \left\langle \frac{\partial N^e}{\partial Y} \right\rangle \{p_1^e\} + \mathcal{F}_3\{N^e\} \langle N^e \rangle \{p_1^e\} \\
& + \mathbf{K} H_o \frac{\partial P_o}{\partial X} \left\{\frac{\partial N^e}{\partial X}\right\} \langle N^e \rangle \{p_1^e\} + \mathbf{K} H_o \frac{\partial P_o}{\partial Y} \left\{\frac{\partial N^e}{\partial Y}\right\} \langle N^e \rangle \{p_1^e\} \\
& + C_1 \left(\frac{\partial P_o}{\partial X} \left\{\frac{\partial N^e}{\partial X}\right\} + \frac{\partial P_o}{\partial Y} \left\{\frac{\partial N^e}{\partial Y}\right\} \right) + \mathcal{F}_4\{N^e\} \\
& - \frac{\sigma \mathbf{K}}{H_o} \{N^e\} \langle N^e \rangle \{p_2^e\} \Bigg] \, d\nu^e = 0
\end{aligned} \tag{2.48}$$

$$\begin{aligned}
\int_{\nu^e} \Bigg[& \left\{\frac{\partial N^e}{\partial X}\right\} \left\langle \frac{\partial N^e}{\partial X} \right\rangle \{p_2^e\} + \left\{\frac{\partial N^e}{\partial Y}\right\} \left\langle \frac{\partial N^e}{\partial Y} \right\rangle \{p_2^e\} + \mathcal{F}_1\{N^e\} \left\langle \frac{\partial N^e}{\partial X} \right\rangle \{p_2^e\} \\
& + \mathcal{F}_2\{N^e\} \left\langle \frac{\partial N^e}{\partial Y} \right\rangle \{p_2^e\} + \mathcal{F}_3\{N^e\} \langle N^e \rangle \{p_2^e\} \\
& + \mathbf{K} H_o \frac{\partial P_o}{\partial X} \left\{\frac{\partial N^e}{\partial X}\right\} \langle N^e \rangle \{p_2^e\} + \mathbf{K} H_o \frac{\partial P_o}{\partial Y} \left\{\frac{\partial N^e}{\partial Y}\right\} \langle N^e \rangle \{p_2^e\} \\
& - \frac{\sigma \mathbf{K} \hbar P_o}{H_o^2} \{N^e\} + \frac{\sigma \mathbf{K}}{H_o} \{N^e\} \langle N^e \rangle \{p_1^e\} \Bigg] \, d\nu^e = 0 \, ,
\end{aligned} \tag{2.49}$$

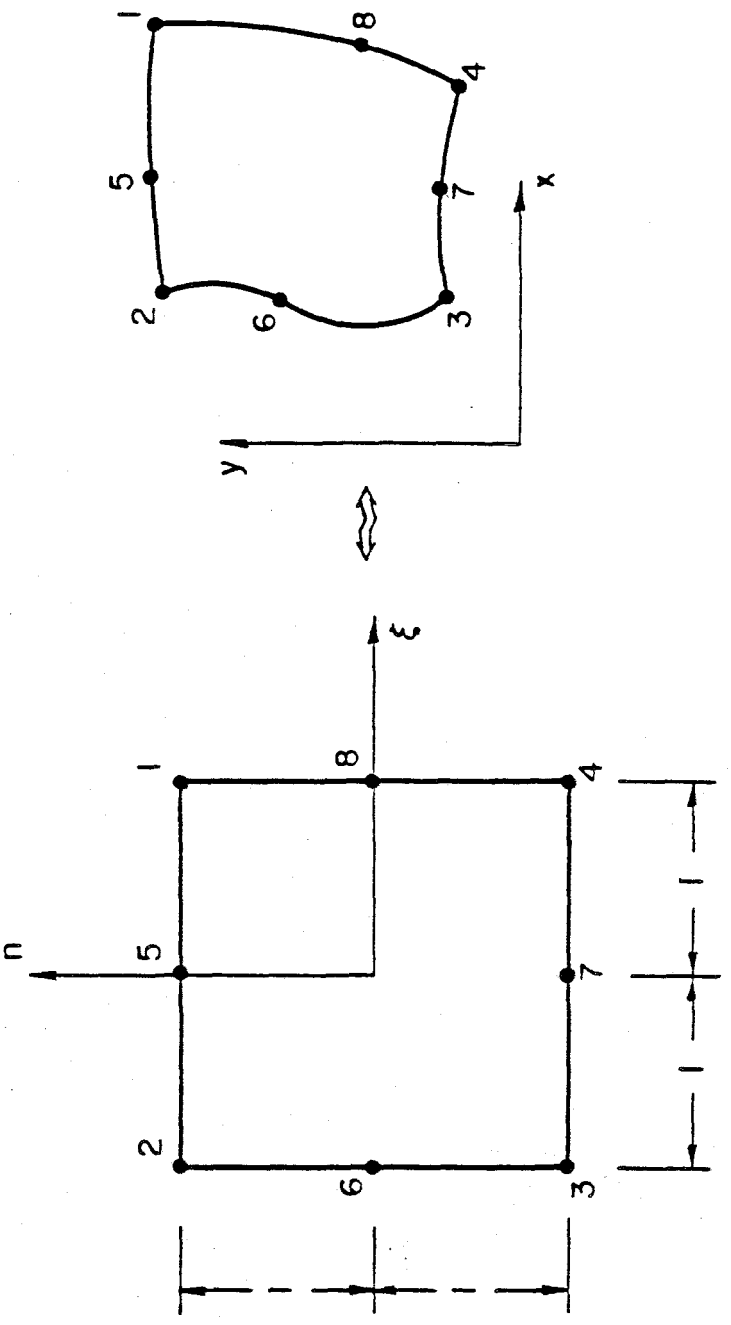

FIGURE 2.2: 8-NODE ISOPARAMETRIC MAPPED ELEMENT

where

$$C_1 = 3\mathbf{K}\hbar\left(P_o + \frac{4K_n}{H_o}\right)$$

$$C_2 = \mathbf{K}\left\{2H_o\frac{\partial P_o}{\partial X} + \frac{3}{H_o}\frac{\partial H_o}{\partial X}(4K_n + P_oH_o) - \frac{\Lambda_x}{H_o}\right\}$$

$$C_3 = \mathbf{K}\left\{2H_o\frac{\partial P_o}{\partial Y} + \frac{3}{H_o}\frac{\partial H_o}{\partial Y}(4K_n + P_oH_o) - \frac{\Lambda_y}{H_o}\right\}$$

$$C_4 = 3\mathbf{K}\left\{\frac{\partial P_o}{\partial X}\frac{\partial H_o}{\partial X} + \frac{\partial P_o}{\partial Y}\frac{\partial H_o}{\partial Y} - \frac{\Lambda_x}{3H_o^2}\frac{\partial H_o}{\partial X} - \frac{\Lambda_y}{3H_o^2}\frac{\partial H_o}{\partial Y}\right\}$$

$$\begin{aligned} C_5 = 3\mathbf{K}\hbar\Bigg\{&\left(\frac{\partial P_o}{\partial X}\right)^2 + \left(\frac{\partial P_o}{\partial Y}\right)^2 + \frac{2}{H_o}\left(P_o + \frac{2K_n}{H_o}\right)\left(\frac{\partial P_o}{\partial X}\frac{\partial H_o}{\partial X} + \frac{\partial P_o}{\partial Y}\frac{\partial H_o}{\partial Y}\right) \\ &- \frac{\Lambda_x}{3H_o^2}\frac{\partial P_o}{\partial X} - \frac{\Lambda_y}{3H_o^2}\frac{\partial P_o}{\partial Y}\Bigg\} - \frac{3\mathbf{K}}{H_o}(4K_n + P_oH_o)\left(\beta\frac{\partial P_o}{\partial X} + \gamma\frac{\partial P_o}{\partial Y}\right) \\ &+ \frac{\mathbf{K}P_o}{H_o^2}(\beta\Lambda_x + \gamma\Lambda_y) \end{aligned}$$

$$\mathcal{F}_1 = \mathbf{K}H_o\frac{\partial P_o}{\partial X} - C_2$$

$$\mathcal{F}_2 = \mathbf{K}H_o\frac{\partial P_o}{\partial Y} - C_3$$

$$\mathcal{F}_4 = \frac{\partial C_1}{\partial X}\frac{\partial P_o}{\partial X} + \frac{\partial C_1}{\partial Y}\frac{\partial P_o}{\partial Y} - C_5$$

$$\mathcal{F}_3 = \mathbf{K}\left(\frac{\partial P_o}{\partial X}\frac{\partial H_o}{\partial X} + \frac{\partial P_o}{\partial Y}\frac{\partial H_o}{\partial Y}\right) + H_o\left(\frac{\partial \mathbf{K}}{\partial X}\frac{\partial P_o}{\partial X} + \frac{\partial \mathbf{K}}{\partial Y}\frac{\partial P_o}{\partial Y}\right) - C_4\,.$$

Equations 2.48 and 2.49 can now be expressed in partitioned form.

$$\begin{bmatrix} [K_p^e] & -[\bar{K}_p^e] \\ [K_p^e] & [\bar{K}_p^e] \end{bmatrix} \begin{Bmatrix} \{p_1^e\} \\ \{p_2^e\} \end{Bmatrix} = \begin{Bmatrix} \{F_1^e\} \\ \{F_2^e\} \end{Bmatrix} \tag{2.50}$$

with the individual submatrices in 2.50 defined as follows:

$$\begin{aligned} [K_p^e] = \int_{-1}^{1}\int_{-1}^{1} \Bigg[&\left\{\frac{\partial N^e}{\partial X}\right\}\left\langle\frac{\partial N^e}{\partial X}\right\rangle + \left\{\frac{\partial N^e}{\partial Y}\right\}\left\langle\frac{\partial N^e}{\partial Y}\right\rangle + F_1\{N^e\}\left\langle\frac{\partial N^e}{\partial X}\right\rangle \\ &+ F_2\{N^e\}\left\langle\frac{\partial N^e}{\partial Y}\right\rangle + F_3\{N^e\}\langle N^e\rangle \\ &+ \mathbf{K}H_o\left(\frac{\partial P_o}{\partial X}\left\{\frac{\partial N^e}{\partial X}\right\}\langle N^e\rangle + \frac{\partial P_o}{\partial Y}\left\{\frac{\partial N^e}{\partial Y}\right\}\langle N^e\rangle\right)\Bigg] \det[J]\,d\xi\,d\eta \end{aligned} \tag{2.51}$$

$$[\bar{K}_p^e] = \int_{-1}^{1}\int_{-1}^{1}\left[\frac{\sigma\mathbf{K}}{H_o}\{N^e\}\langle N^e\rangle\right]\det[J]\,d\xi\,d\eta \tag{2.52}$$

$$\{F_1^e\} = -\int_{-1}^{1}\int_{-1}^{1} \left[C_1 \frac{\partial P_o}{\partial X}\left\{\frac{\partial N^e}{\partial X}\right\} + C_1 \frac{\partial P_o}{\partial Y}\left\{\frac{\partial N^e}{\partial Y}\right\} + F_4\{N^e\}\right] \det[J] d\xi\, d\eta \qquad (2.53)$$

$$\{F_2^e\} = -\int_{-1}^{1}\int_{-1}^{1} \left[\frac{\sigma \mathbf{K} \hbar P_o}{H_o^2}\{N^e\}\right] \det[J] d\xi\, d\eta\,. \qquad (2.54)$$

When written in terms of complex quantities, 2.50 can be seen to be of the same form as the matrix equation for the equilibrium solution, Equation 2.42. This is convenient for solution on a computer, since the same matrix reduction algorithm can be used to solve for the unknown quantities. In this fashion, the linearized dynamic stiffness and damping matrices of the slider bearing are obtained without iteration.

$$\left[K_p + i\bar{K}_p\right]\{p_1 + ip_2\} = \{F_1 + iF_2\} \qquad (2.55)$$

2.4 Properties of the Solution

Before using the linearized dynamic stiffness and damping of the gas bearing in formulating the equations of motion of the slider, it is interesting to examine the behavior of p_1 and p_2 for some special cases.

The simplest special case is the plane isothermal squeeze film, or 1-D parallel plate problem. The slider is assumed to be infinitely wide and parallel to the disk surface, and the only dimension of the problem is in the direction of lubricant flow velocity. This problem was solved analytically, for the case of zero bearing number, by Langlois (84). Equations 2.29 and 2.30 for this case reduce to the following:

$$\frac{d^2 p_2}{dY^2} = \sigma(p_1 + 1) \qquad (2.56)$$

$$\frac{d^2 p_1}{dY^2} = -\sigma p_2 \qquad (2.57)$$

The analytical solutions, due to Langlois (84), are

$$\begin{aligned} p_1(Y) = &\frac{2}{\cosh k + \cos k}\left\{\cosh\frac{k}{2}\cos\frac{k}{2}\cosh kY\cos kY\right. \\ &\left. + \sinh\frac{k}{2}\sin\frac{k}{2}\sinh kY\sin kY\right\} - 1 \end{aligned} \qquad (2.58)$$

$$p_2(Y) = \frac{2}{\cosh k + \cos k} \left\{ -\sinh \frac{k}{2} \sin \frac{k}{2} \cosh kY \cos kY + \cosh \frac{k}{2} \cos \frac{k}{2} \sinh kY \sin kY \right\}, \tag{2.59}$$

where

$$k = \left(\frac{\sigma}{2}\right)^{1/2}$$

$$f_1 = 1 - \frac{1}{k} \left\{ \frac{\sinh k + \sin k}{\cosh k + \cos k} \right\} \tag{2.60}$$

$$f_2 = \frac{1}{k} \left\{ \frac{\sinh k - \sin k}{\cosh k + \cos k} \right\} . \tag{2.61}$$

When the squeeze number, σ, is very large, the following approximations for f_1 and f_2 are obtained.

$$f_1 \approx 1 - \left(\frac{2}{\sigma}\right)^{1/2}$$
$$f_2 \approx \left(\frac{2}{\sigma}\right)^{1/2} \tag{2.62}$$

Similarly, for a very small squeeze number,

$$f_1 \approx \frac{\sigma^2}{120}$$
$$f_2 \approx \frac{\sigma}{12} . \tag{2.63}$$

Results from the finite element solution are compared with Langlois' analytical values in Figures 2.3 through 2.6. Figure 2.3 shows the correlation between the in-phase and out-of-phase perturbation pressures, p_1 and p_2, respectively, along the bearing. The resulting in-phase and out-of-phase forces are compared in Figure 2.4, as a function of the squeeze number, showing good agreement. The in-phase load for a unit perturbation in the z, or heave, direction, corresponding to the vertical stiffness of the bearing, is shown in Figure 2.5. The analytical and finite element solutions agree well over a large range of frequencies. The asymptotes from Equations 2.62 and 2.63 are also shown for comparison. The out-of-phase load for a unit vertical velocity, representing the heave damping coefficient, is shown to correlate between the two solution methods in Figure 2.6. Asymptotes from Equations 2.62 and 2.63 are also given in this figure.

A second case of interest is that of the 1-D plane wedge, similar to the parallel plate problem except that the bearing now presents a converging channel to the oncoming flow.

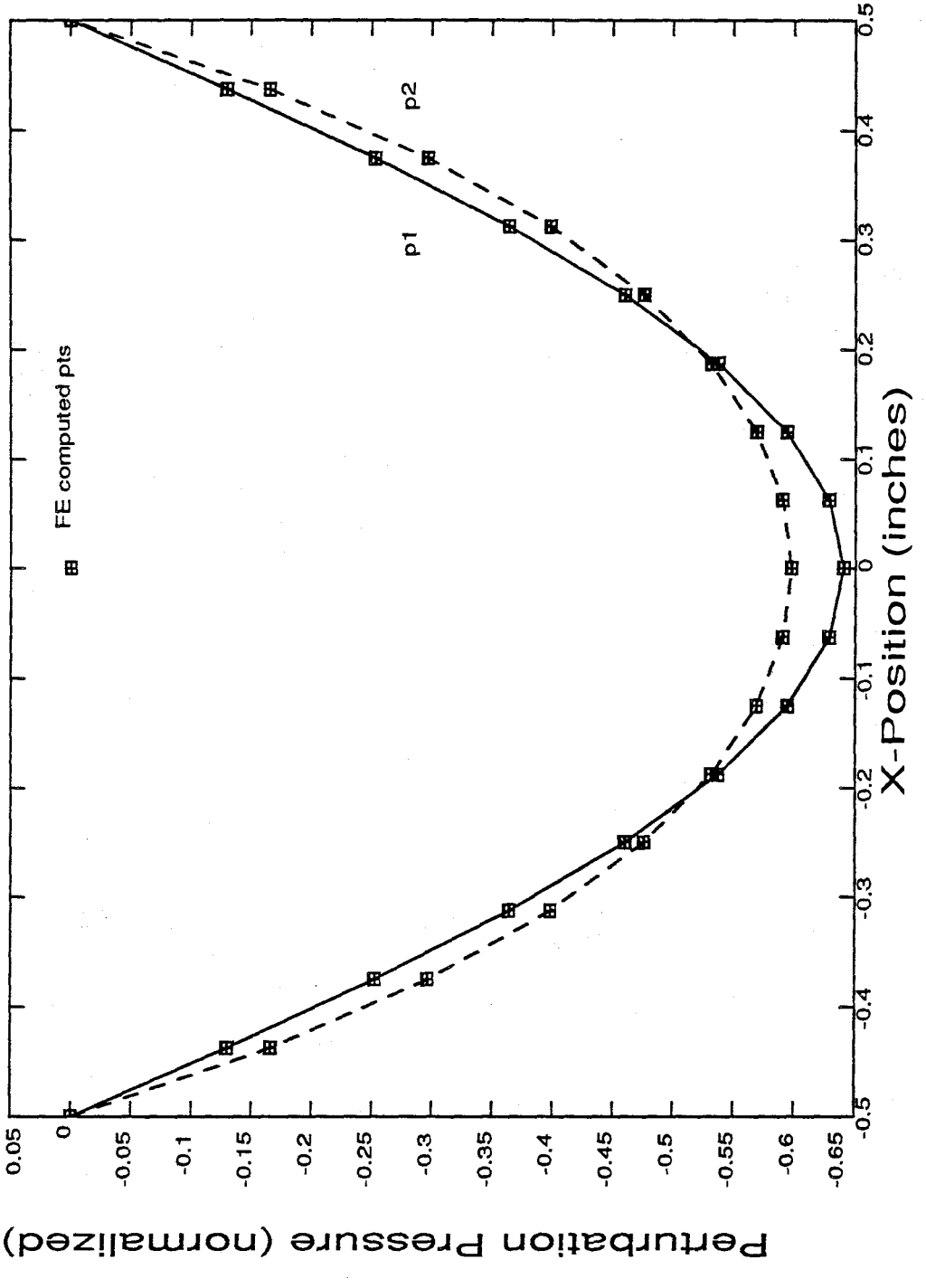
Figure 2.3: FE vs. Analytical, 1-D Squeeze Film, Bearing No. = 0
Perturbation Pressure (normalized)
X-Position (inches)
FE computed pts
p1
p2
0.05
0
-0.05
-0.1
-0.15
-0.2
-0.25
-0.3
-0.35
-0.4
-0.45
-0.5
-0.55
-0.6
-0.65
0.5
0.4
0.3
0.2
0.1
0
-0.1
-0.2
-0.3
-0.4
-0.5

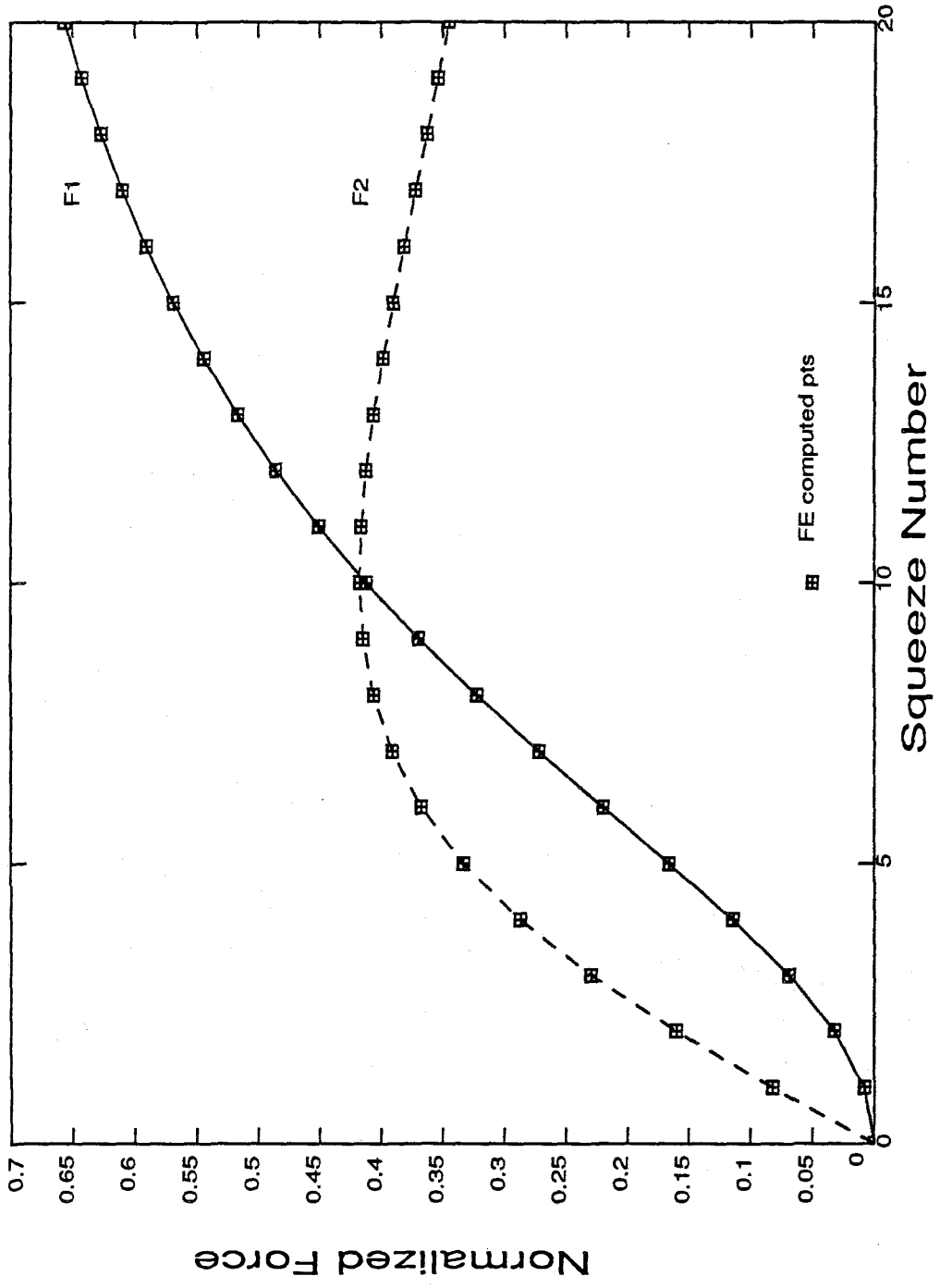

Figure 2.4: FE vs. Analytical, 1-D Squeeze Film, Bearing No. = 0

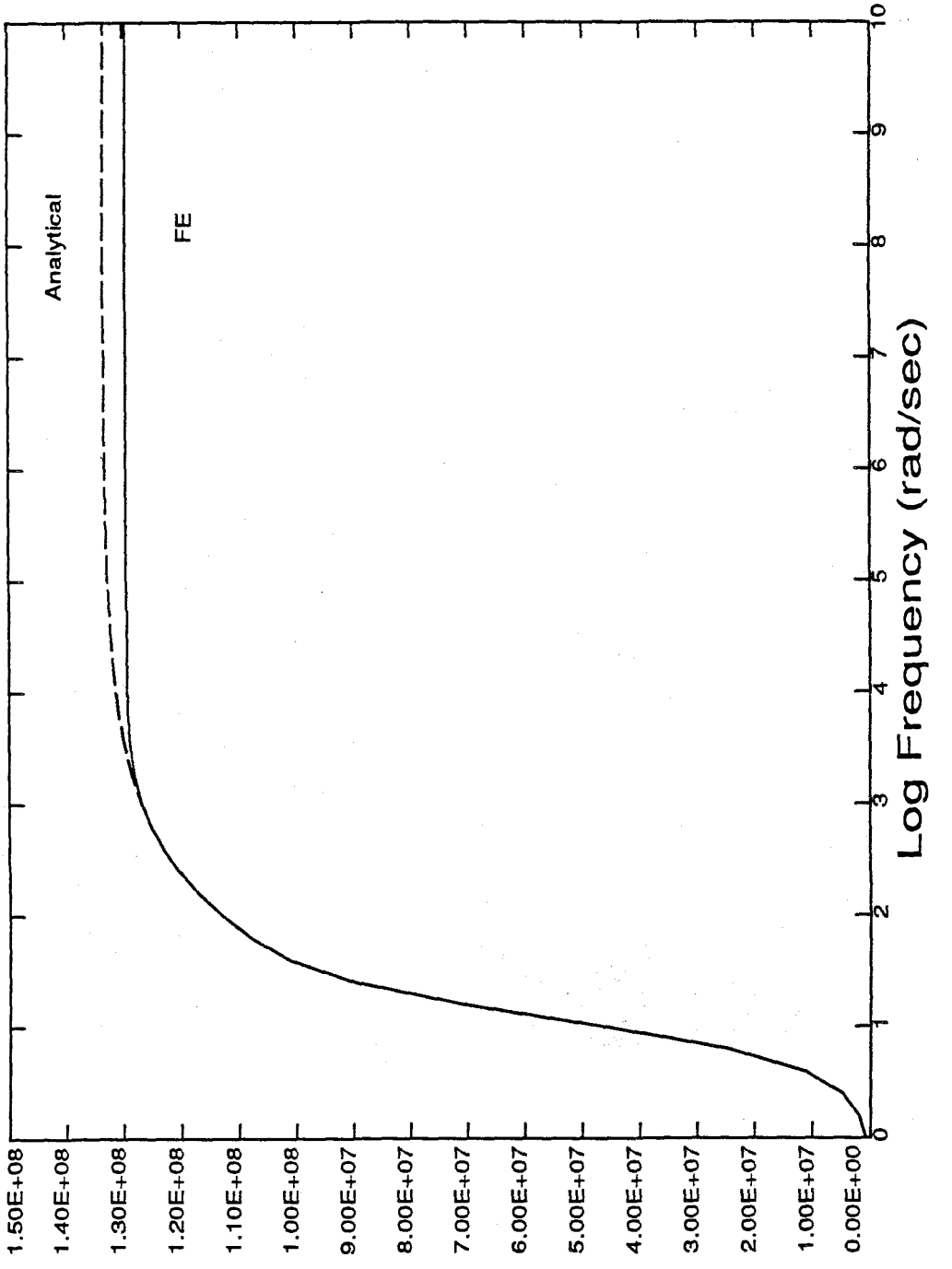

Figure 2.5: FE vs. Analytical, 1-D Squeeze Film, Bearing No. = 0

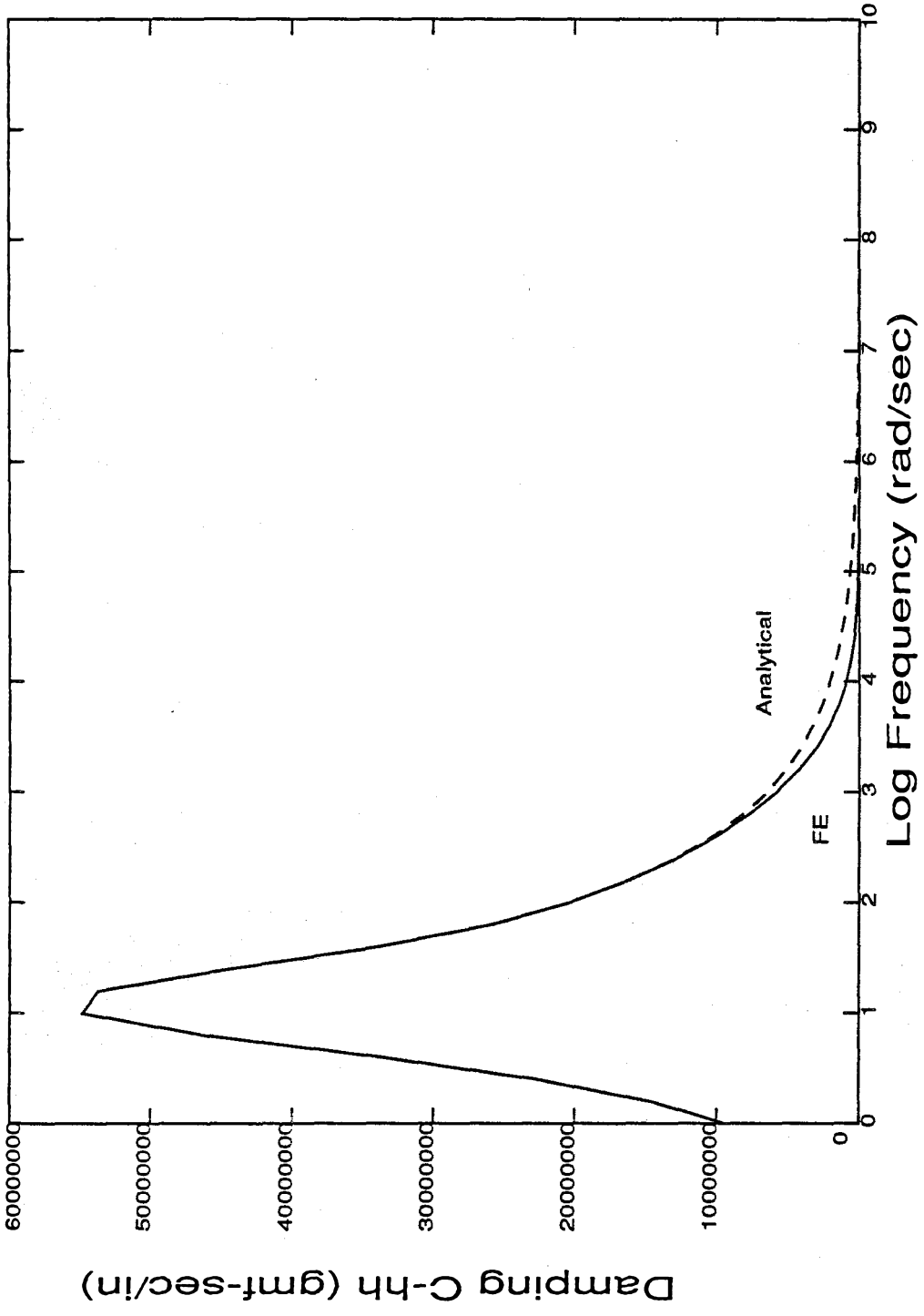

Figure 2.6: FE vs. Analytical, 1-D Squeeze Film, Bearing No. = 0

For the limiting case of a zero bearing number, the equations for the 1-D plane wedge reduce to the following:

$$\frac{d^2p_1}{dY^2} + \frac{3}{H_o}\frac{dH_o}{dY}\frac{dp_1}{dY} = \frac{-\sigma}{H_o^2}p_2 \tag{2.64}$$

$$\frac{d^2p_2}{dY^2} + \frac{3}{H_o}\frac{dH_o}{dY}\frac{dp_2}{dY} = \frac{\sigma}{H_o^2}\left(p_1 + \frac{\bar{h}}{H_o}\right) . \tag{2.65}$$

$H_o(Y)$ for the plane wedge geometry is given by

$$H_o(Y) = (1 - H_i)Y + H_i . \tag{2.66}$$

For a very large squeeze number, σ, the perturbation pressures are

$$p_1(Y) = \frac{-\{\alpha + \gamma(Y_o - Y)\}}{(1 - H_i)Y + H_i} \tag{2.67}$$

$$p_2(Y) = 0 .$$

This corresponds, for example, to the case of high-frequency perturbation of the gas film.

Equation 2.67 can be integrated to give the force and moment from the in-phase pressure component, resulting in,

$$f_1 = \frac{1}{(1 - H_i)}\left[(\alpha + \gamma Y_o)\ln H_i + \gamma\left\{1 + \frac{H_i \ln H_i}{(1 - H_i)}\right\}\right] \tag{2.69}$$

$$\begin{aligned} m_1 =& \frac{(\alpha + \gamma Y_o)}{(1 - H_i)}\left[1 + \frac{H_i \ln H_i}{(1 - H_i)}\right] \\ & - \frac{\gamma}{(1 - H_i)^3}\left[\frac{1}{2} - 2H_i + \frac{3H_i^2}{2} - H_i^2 \ln H_i\right] + f_1 Y_o . \end{aligned} \tag{2.70}$$

The 1-D plane wedge differs primarily from the 1-D parallel plate in that it has an additional degree of freedom in pitch, i.e., in rotation about an axis transverse to the lubricant flow direction. The numerically computed values for the four stiffness and four damping coefficients, for a wide range of frequencies, are given in Figures 2.7 through 2.14. Equations 2.69 and 2.70, with the appropriate choices of α and γ, can be used to predict

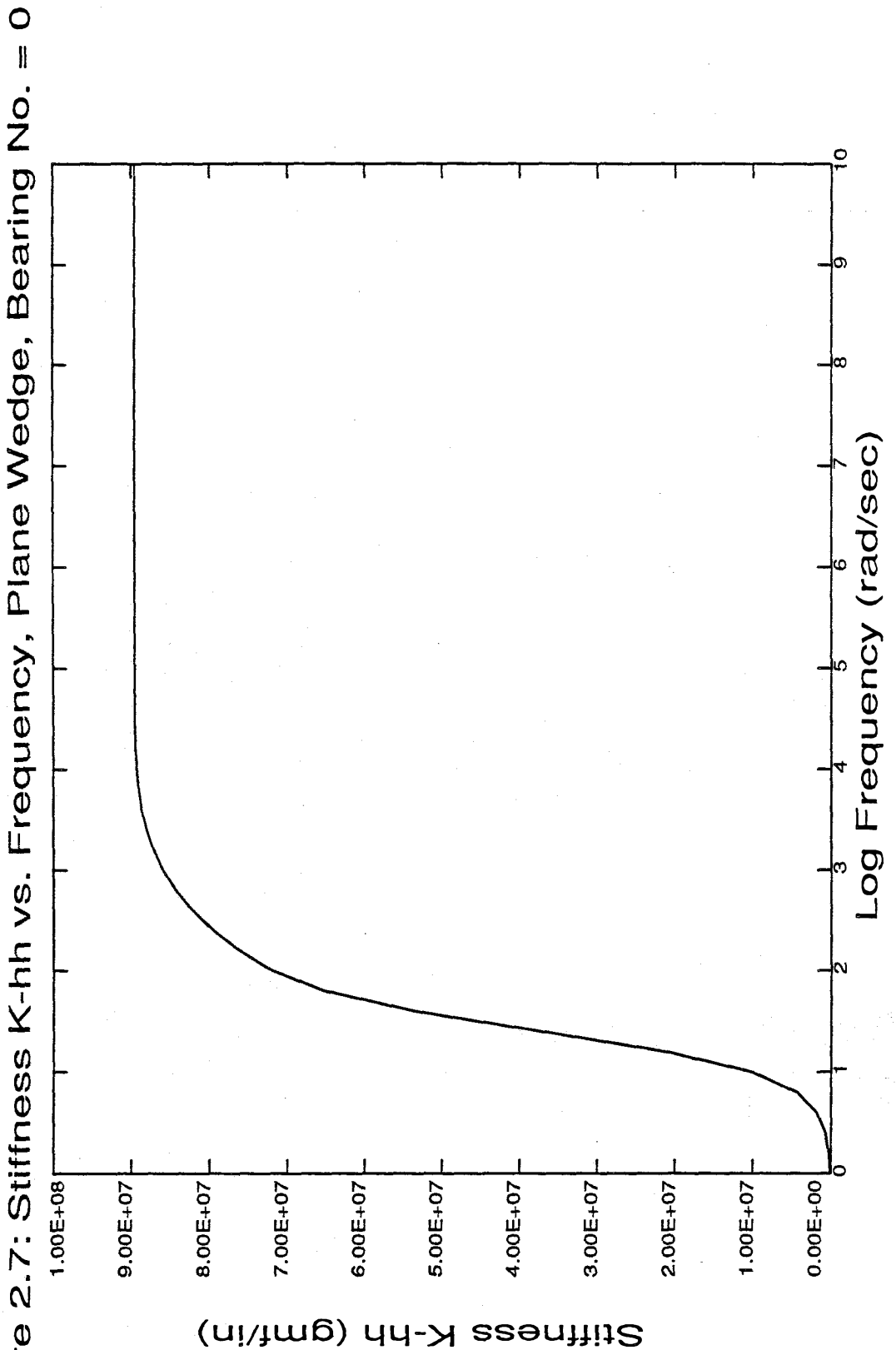

Figure 2.7: Stiffness K-hh vs. Frequency, Plane Wedge, Bearing No. = 0

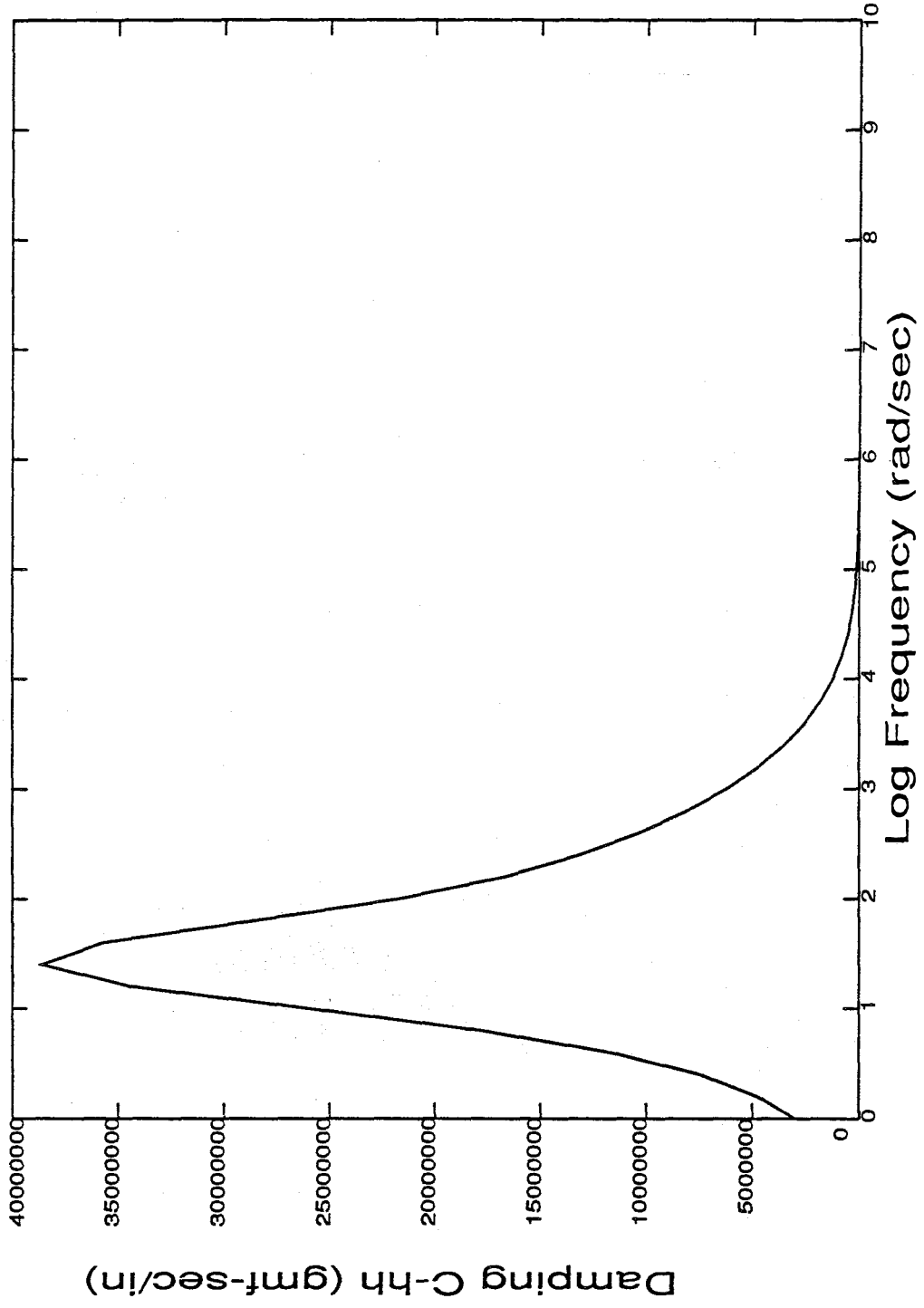

Figure 2.8: Damping C-hh vs. Frequency, Plane Wedge, Bearing No. = 0

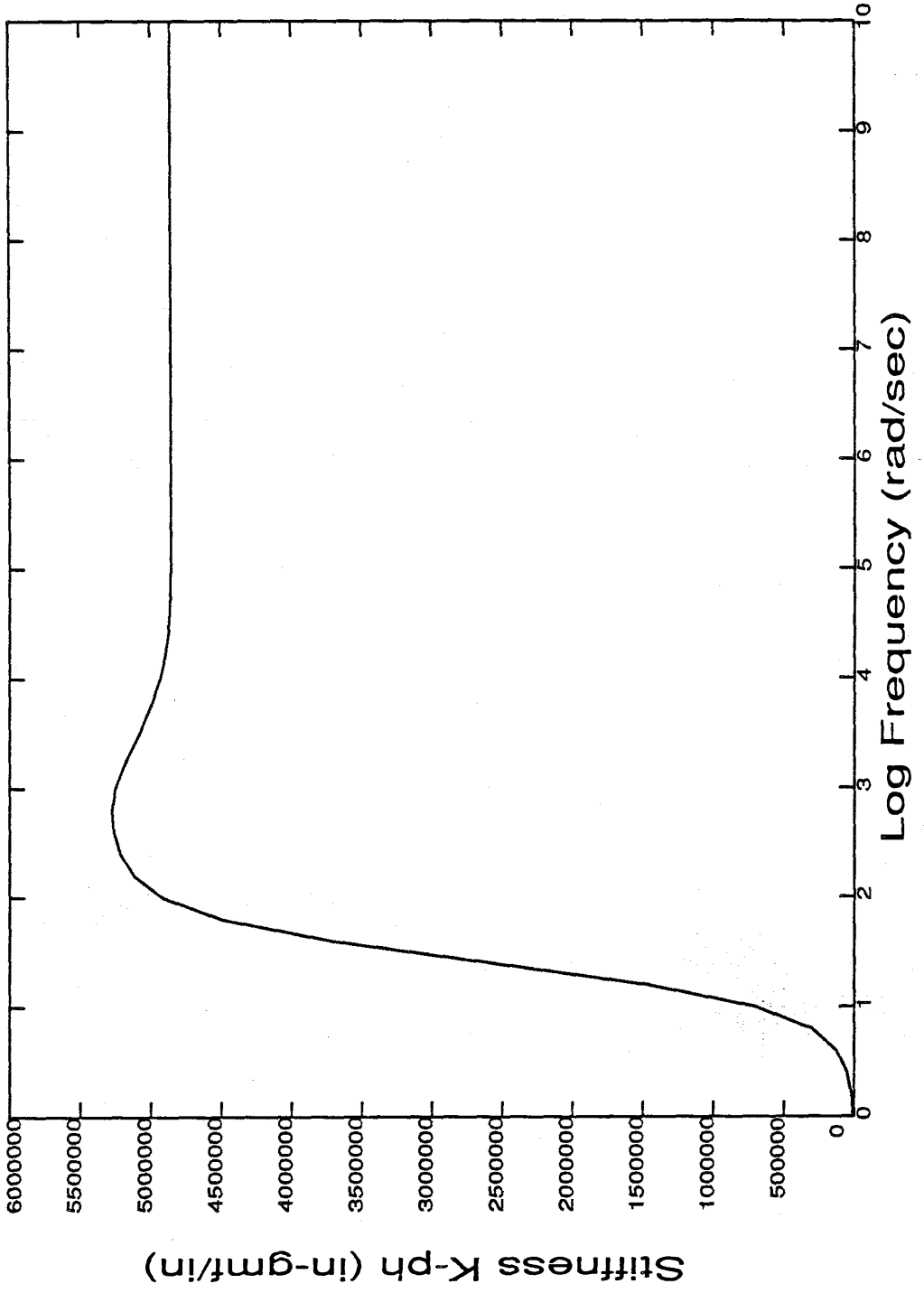

Figure 2.9: Stiffness K-ph vs. Frequency, Plane Wedge, Bearing No. = 0

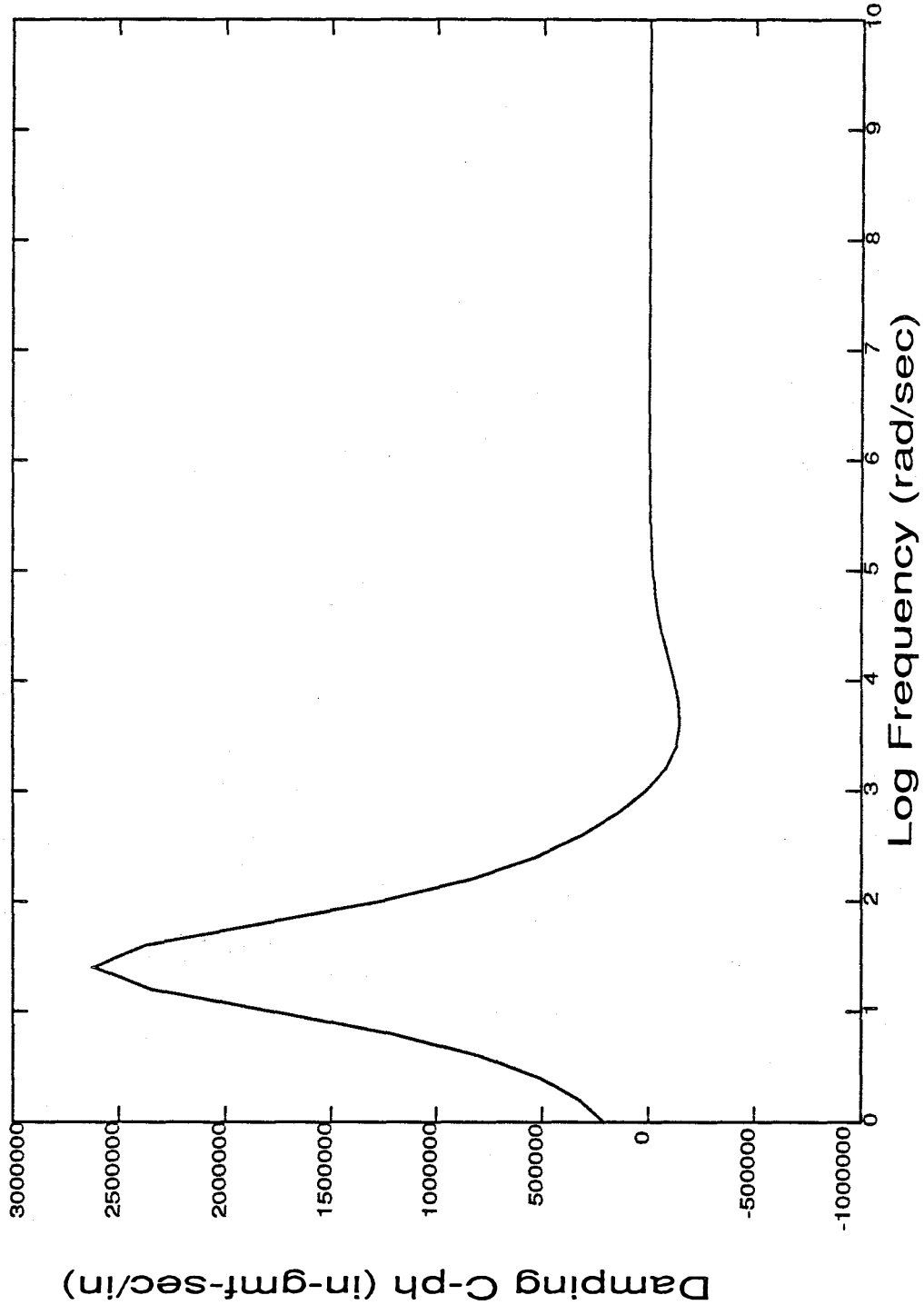

Figure 2.10: Damping C-ph vs. Frequency, Plane Wedge, Bearing No. = 0

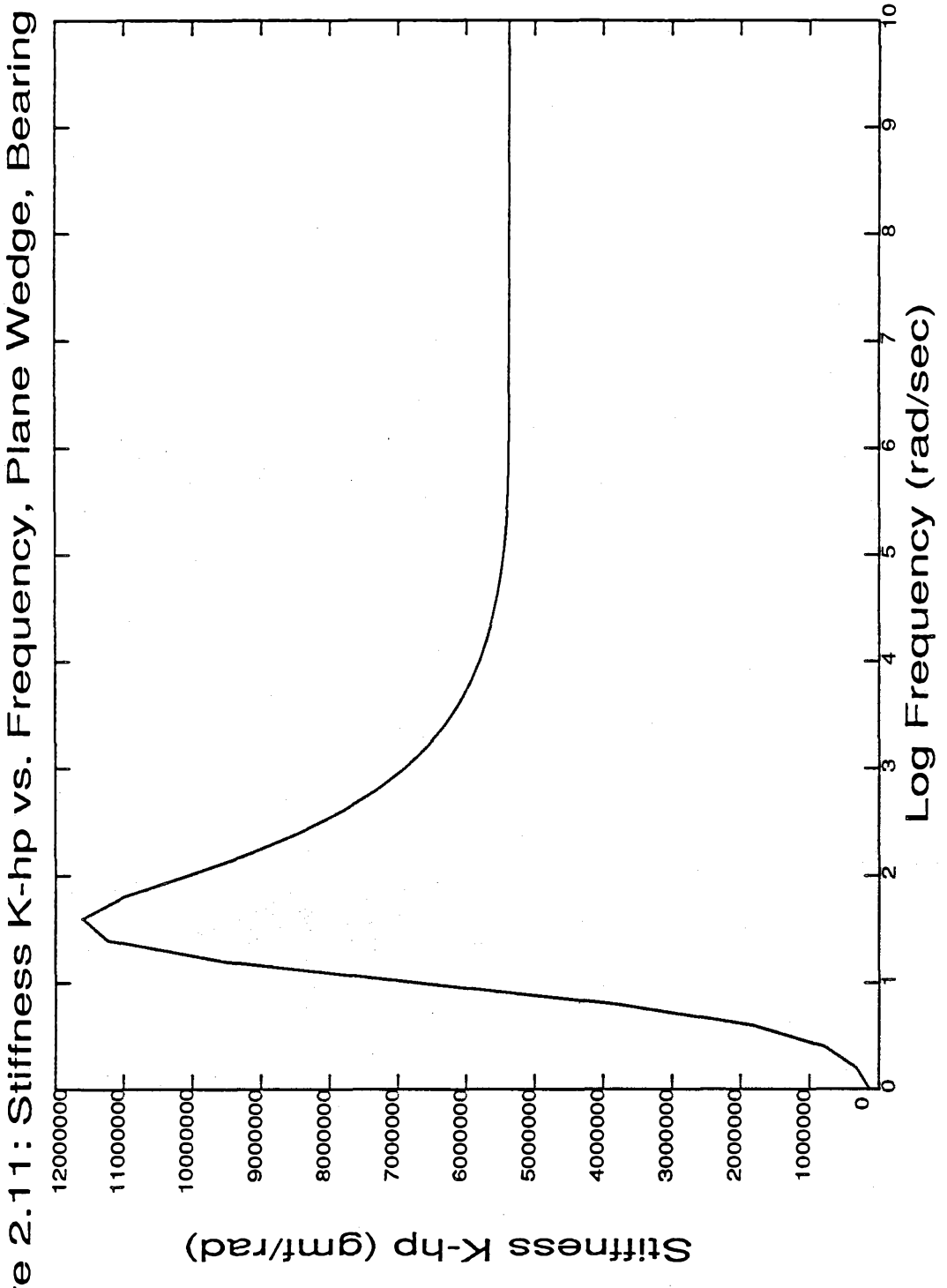

Figure 2.11: Stiffness K-hp vs. Frequency, Plane Wedge, Bearing No. = 0

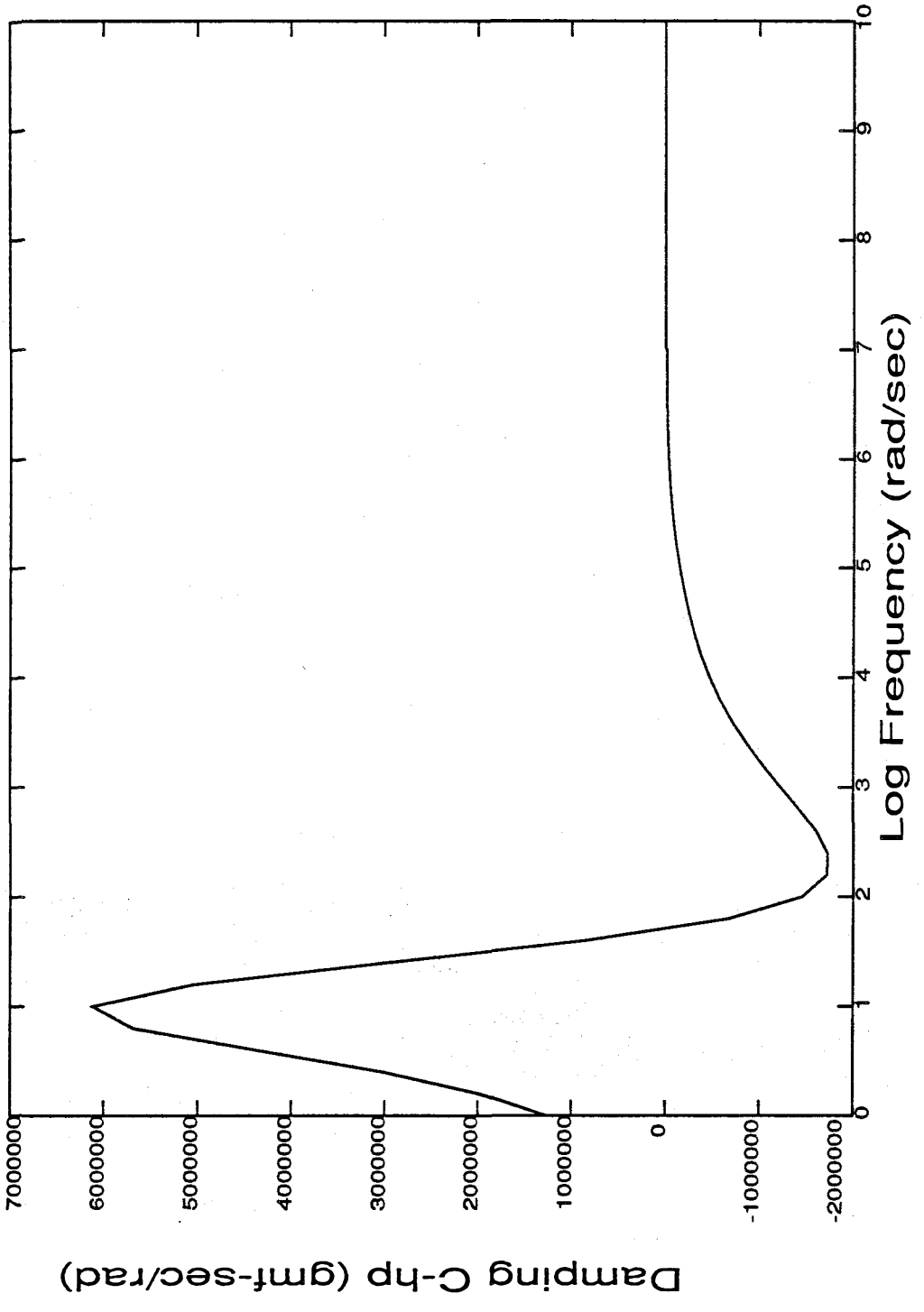

Figure 2.12: Damping C-hp vs. Frequency, Plane Wedge, Bearing No. = 0

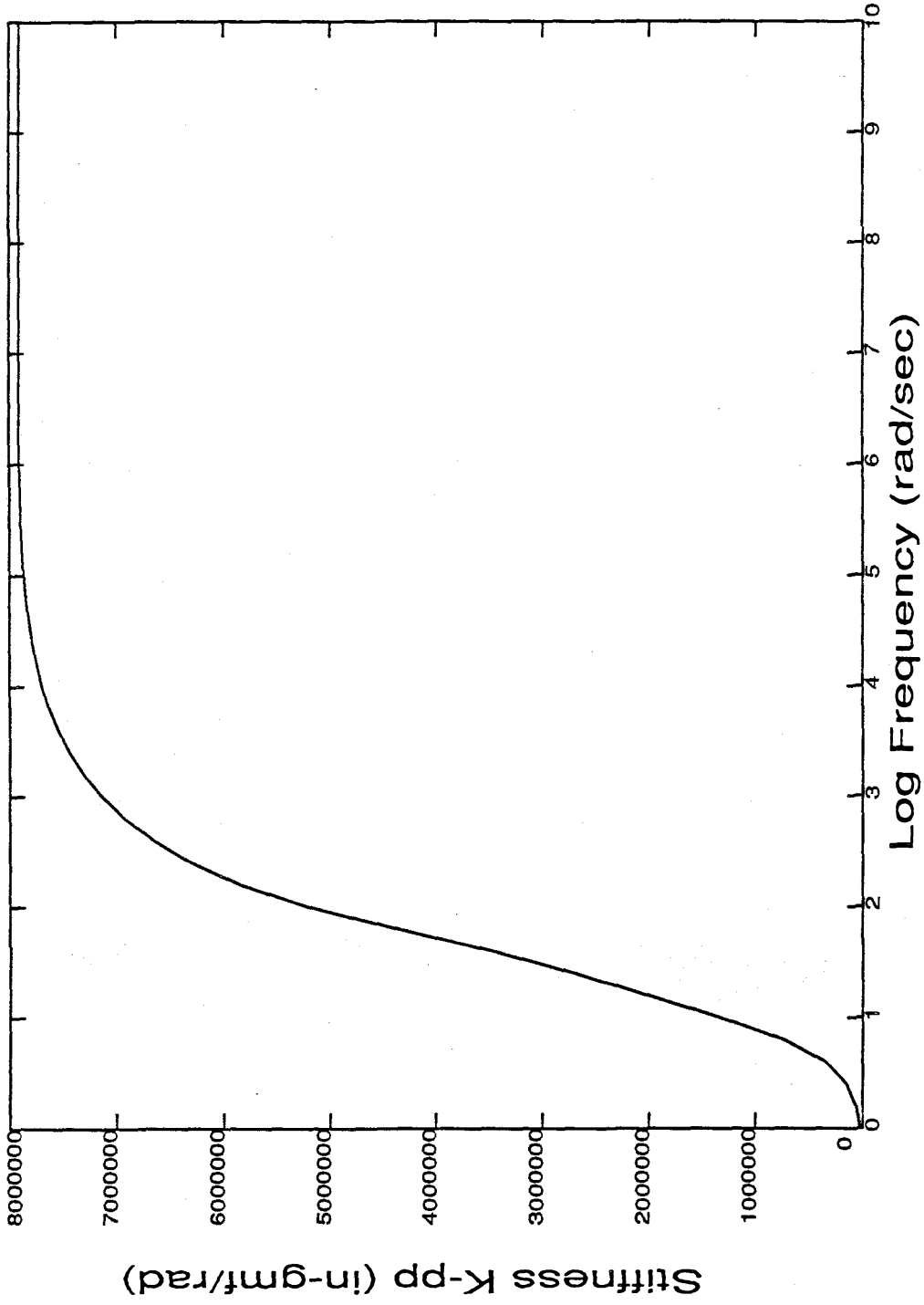

Figure 2.13: Stiffness K-pp vs. Frequency, Plane Wedge, Bearing No. = 0

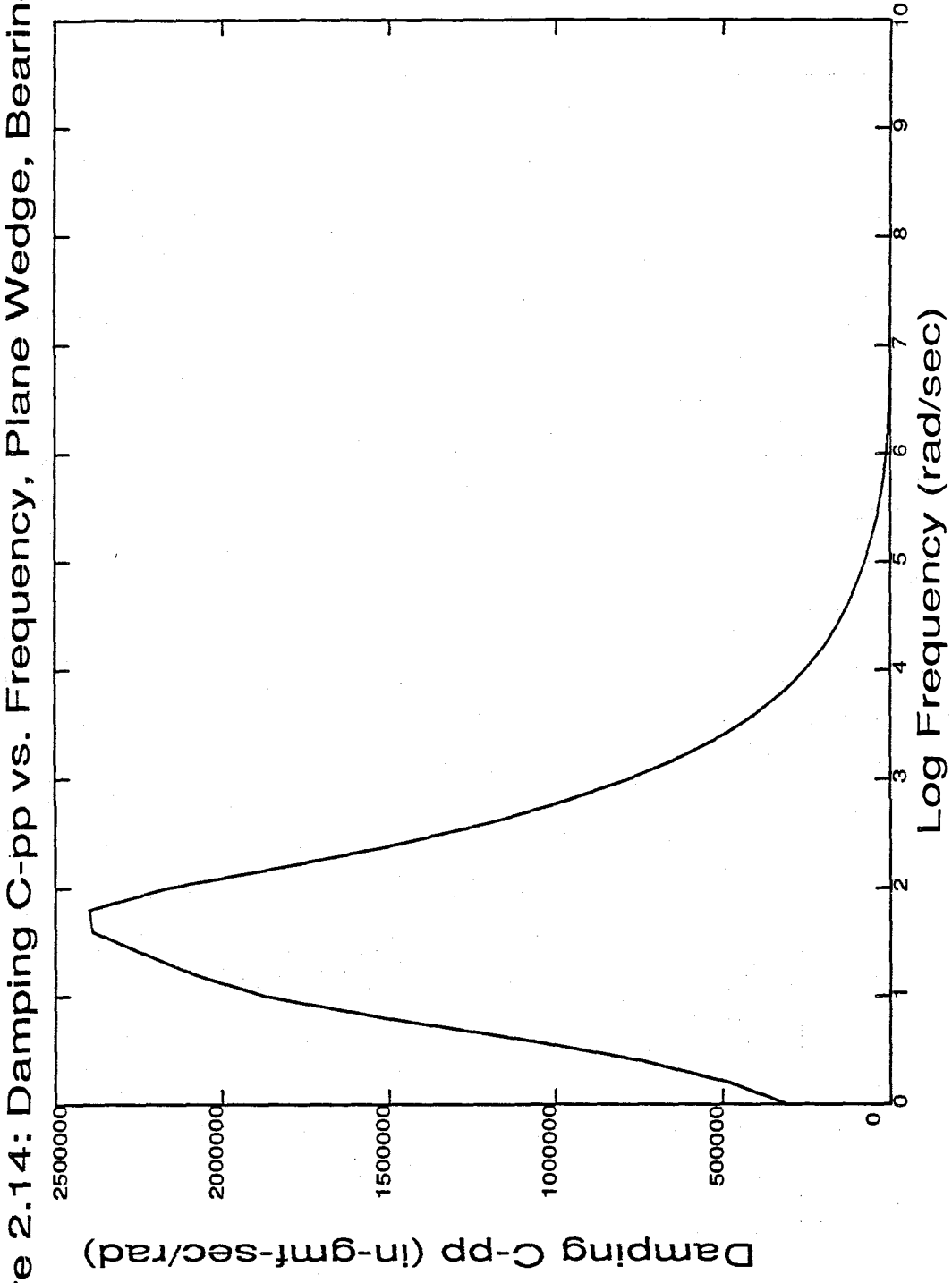

Figure 2.14: Damping C-pp vs. Frequency, Plane Wedge, Bearing No. = 0

the high-frequency, limiting values of the curves. At this limit, the damping is zero, and the stiffness components are as given by the following equations:

$$K_{hh} = \frac{\ln H_i}{1 - H_i} \tag{2.71}$$

$$K_{hp} = \frac{1}{1 - H_i} \left[\ln H_i \left\{ Y_o + \frac{H_i}{1 - H_i} \right\} + 1 \right] \tag{2.72}$$

$$K_{pp} = \frac{2Y_o}{1 - H_i} \left[1 + \ln H_i \left\{ \frac{H_i}{1 - H_i} + \frac{Y_o}{2} \right\} \right] - \frac{1}{(1 - H_i)^3} \left[\frac{1}{2} - 2H_i + \frac{3H_i^2}{2} - H_i^2 \ln H_i \right] \tag{2.73}$$

$$K_{ph} = K_{hp} \, , \tag{2.74}$$

where

K_{hh} = vertical force-per-unit heave displacement

K_{pp} = pitch moment-per-unit pitch rotation

K_{ph} = pitch moment-per-unit heave displacement

K_{hp} = vertical force-per-unit pitch rotation

It is interesting to note that, for the simple 1-D plane wedge at low speed and high frequency, the stiffness is a function only of pivot placement, Y_o, and inlet spacing, H_i.

For the limiting case of a zero bearing number and a zero squeeze number, both p_1 and p_2 vanish. As the bearing number becomes infinitely large while the squeeze number remains finite, a situation that most closely approximates current slider trends, the following equations for perturbation pressures are found:

$$\frac{dp_1}{dY} + \frac{1}{H_o} \frac{dH_o}{dY} p_1 = \frac{H_i}{H_o^2} \left\{ \gamma + \frac{\hbar}{H_o} \frac{dH_o}{dY} \right\} \tag{2.75}$$

$$\frac{dp_2}{dY} + \frac{1}{H_o} \frac{dH_o}{dY} p_2 = 0 \, . \tag{2.76}$$

Equations 2.75 and 2.76 are solved, subject to the boundary conditions of $p_1(0) = p_2(0) = p_1(1) = p_2(1) = 0$ to yield,

$$p_1(Y) = \frac{H_i}{H_o} \left[\frac{\gamma \{ H_i - Y_o(H_i - 1) - H_o \}}{H_o(H_i - 1)} + \frac{\gamma Y_o}{H_i} + \alpha \left\{ \frac{1}{H_i} - \frac{1}{H_o} \right\} \right] \tag{2.77}$$

$$p_2(Y) = 0 \, . \tag{2.78}$$

The in-phase force and moment are computed as before.

$$f_1 = \left\{ \frac{\gamma H_i}{(H_i - 1)} - \gamma Y_o - \alpha \right\} \left\{ 1 - \frac{\ln H_i}{(H_i - 1)} \right\} \tag{2.79}$$

$$\begin{aligned} m_1 = f_1 Y_o + \frac{2\gamma H_i^2 \ln H_i}{(H_i - 1)^3} - \frac{\gamma H_i}{(H_i - 1)^2} \{ (H_i + 1) + 2Y_o \ln H_i \} \\ + \frac{\gamma Y_o (H_i + 1)}{(H_i - 1)} - \frac{\alpha}{(H_i - 1)} \left\{ \frac{2H_i \ln H_i}{(H_i - 1)} - H_i - 1 \right\} \end{aligned} \tag{2.80}$$

The stiffness and damping coefficients computed for a high bearing number are constant with frequency for $\omega/V < .001$. There is no damping in this limit, except where the squeeze number becomes significant compared to the bearing number. As with the low bearing number limit, stiffnesses depend only on the pivot location and inlet spacing. Following the same procedure as before, the stiffnesses are computed from Equations 2.79 and 2.80 to be

$$K_{hh} = \frac{\ln H_i}{H_i - 1} - 1 \tag{2.81}$$

$$K_{hp} = \left(\frac{H_i}{H_i - 1} - Y_o \right) \left(1 - \frac{\ln H_i}{H_i - 1} \right) \tag{2.82}$$

$$K_{ph} = Y_o \left(\frac{\ln H_i}{H_i - 1} - 1 \right) - \frac{2H_i \ln H_i}{(H_i - 1)^2} + \frac{H_i + 1}{H_i - 1} \tag{2.83}$$

$$\begin{aligned} K_{pp} = Y_o \left(\frac{H_i}{H_i - 1} - Y_o \right) \left(1 - \frac{\ln H_i}{H_i - 1} \right) + \frac{2H_i^2 \ln H_i}{(H_i - 1)^3} \\ - \frac{H_i}{(H_i - 1)^2} (1 + H_i + 2Y_o \ln H_i) + Y_o \left(\frac{H_i + 1}{H_i - 1} \right) . \end{aligned} \tag{2.84}$$

A final analytical relationship of interest is obtained when both the bearing number and the squeeze number are large enough to dominate the other terms in Equations 2.29 and 2.30. For this case, the following ordinary differential equations for p_1 and p_2 are obtained.

$$\frac{d(p_2 H_o)}{dY} = -\frac{2\omega l}{V} (p_1 H_o + \hbar P_o) \tag{2.85}$$

$$\frac{d(p_1 H_o)}{dY} + \frac{d(\hbar P_o)}{dY} = \frac{2\omega l}{V} p_2 H_o \tag{2.86}$$

The solutions are as follows:

$$p_1(Y) = \frac{\hbar}{H_o}\left\{\cos\left(\frac{2\omega l Y}{V}\right) - \frac{H_i}{H_o}\right\} \tag{2.87}$$

$$p_2(Y) = -\frac{\hbar}{H_o}\sin\left(\frac{2\omega l Y}{V}\right) . \tag{2.88}$$

Integration of these pressures to obtain loading on the slider bearing results in sine and cosine integrals, which must be evaluated numerically.

2.5 Summary

Solutions for the equilibrium pressure distribution, and the corresponding forces and moments, have been obtained using the finite element method. The in-phase and out-of-phase perturbation pressures were calculated using this pressure field. From these, frequency-dependent linearized dynamic stiffness and damping matrices for the slider bearing were developed. In the next chapter, these bearing properties will be used in formulating the equations of motion of the slider.

CHAPTER 3

SLIDER DYNAMICS

3.1 Slider Equations of Motion

The slider-bearing-support system is shown schematically in Figure 3.1. The support that holds the slider in place over the moving disk surface is modeled by a set of linear and rotational springs attached at the pivot point. The dynamical equations of motion are referenced to a coordinate system located at the mass center of the slider and aligned with the slider's principal axes. The positive Y-axis of this system is aligned with the direction of flow through the bearing, and the X-axis is perpendicular to the flow direction.

Motions of the slider in the x and y directions, i.e., in the plane of the disk surface, are undesirable because they disturb the alignment of the transducer with magnetically recorded information. The slider bearing, however, has very little influence on these motions, and virtually all slider support systems are designed to provide minimal compliance in the disk plane. For that reason, the current analysis is limited to three degrees of freedom; the slider is free to pitch about the x-axis, to roll about the y-axis, and to heave, or translate, in the z-direction.

Based on the spring-mass-damper system defined by Figure 3.1, the equations of motion for the slider are

$$\begin{aligned} m\ddot{z} + k_z(z + \alpha y' + \beta x') - \frac{\partial F}{\partial z}z - \frac{\partial F}{\partial \alpha}\alpha - \frac{\partial F}{\partial \beta}\beta \\ - \frac{\partial F}{\partial \dot{z}}\dot{z} - \frac{\partial F}{\partial \dot{\alpha}}\dot{\alpha} - \frac{\partial F}{\partial \dot{\beta}}\dot{\beta} = F_z(t) \end{aligned} \tag{3.1}$$

$$\begin{aligned} I_p\ddot{\alpha} + k_\alpha\alpha + k_z(y'z + \alpha y'^2 + \beta x'y' + \alpha z'^2) \\ - \frac{\partial M_p}{\partial z}z - \frac{\partial M_p}{\partial \beta}\beta - \frac{\partial M_p}{\partial \alpha}\alpha - \frac{\partial M_p}{\partial \dot{z}}\dot{z} + \frac{\partial M_p}{\partial \dot{\alpha}}\dot{\alpha} - \frac{\partial M_p}{\partial \dot{\beta}}\dot{\beta} \\ - y'\left(\frac{\partial F}{\partial z}z + \frac{\partial F}{\partial \alpha}\alpha + \frac{\partial F}{\partial \beta}\beta + \frac{\partial F}{\partial \dot{z}}\dot{z} + \frac{\partial F}{\partial \dot{\alpha}}\dot{\alpha} + \frac{\partial F}{\partial \dot{\beta}}\dot{\beta}\right) = F_\alpha(t) \end{aligned} \tag{3.2}$$

$$\begin{aligned} I_r\ddot{\beta} + k_\beta\beta + k_z(x'z + \alpha x'y' + \beta x'^2 + \beta z'^2) \\ - \frac{\partial M_r}{\partial z}z - \frac{\partial M_r}{\partial \beta}\beta - \frac{\partial M_r}{\partial \alpha}\alpha - \frac{\partial M_r}{\partial \dot{z}}\dot{z} + \frac{\partial M_r}{\partial \dot{\beta}}\dot{\beta} - \frac{\partial M_r}{\partial \dot{\alpha}}\dot{\alpha} \\ + x'\left(\frac{\partial F}{\partial z}z + \frac{\partial F}{\partial \beta}\beta + \frac{\partial F}{\partial \alpha}\alpha + \frac{\partial F}{\partial \dot{z}}\dot{z} + \frac{\partial F}{\partial \dot{\beta}}\dot{\beta} + \frac{\partial F}{\partial \dot{\alpha}}\dot{\alpha}\right) = F_\beta(t)\,. \end{aligned} \tag{3.3}$$

FIGURE 3.1: THE SLIDER-BEARING-SUPPORT MODEL

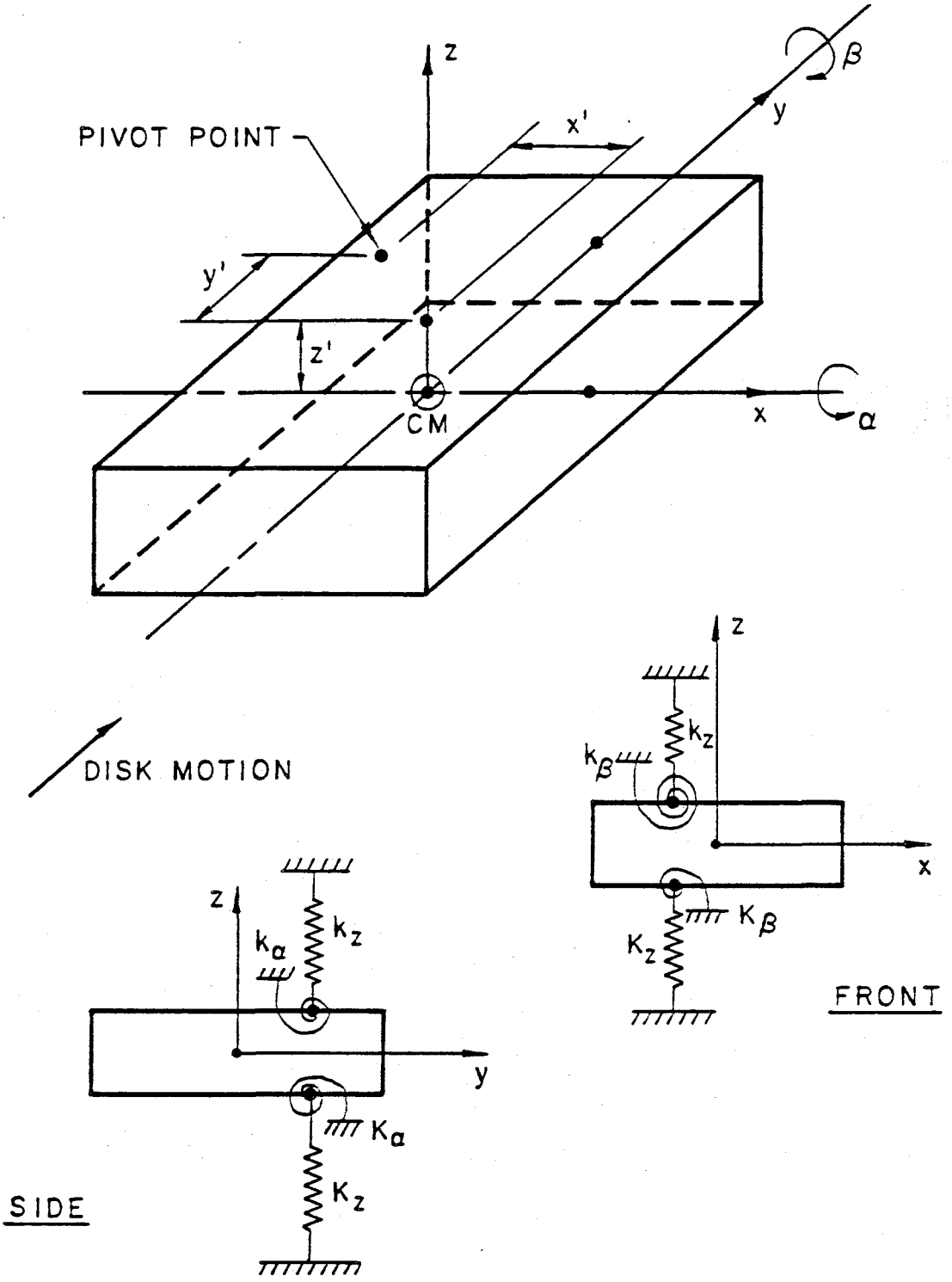

These equations are conveniently written in matrix form as follows:

$$[M]\{\ddot{\xi}\} + [C]\{\dot{\xi}\} + [K]\{\xi\} = \{F\} \tag{3.4}$$

where

$$[M] = \begin{bmatrix} m & 0 & 0 \\ 0 & I_p & 0 \\ 0 & 0 & I_r \end{bmatrix}$$

$$\{\xi\} = \begin{Bmatrix} z \\ \alpha \\ \beta \end{Bmatrix}$$

$$[C] = \begin{bmatrix} \left(-\frac{\partial F}{\partial \dot{z}}\right) & \left(-\frac{\partial F}{\partial \dot{\alpha}}\right) & \left(-\frac{\partial F}{\partial \dot{\beta}}\right) \\ \left(-\frac{\partial M_p}{\partial \dot{z}} - y'\frac{\partial F}{\partial \dot{z}}\right) & \left(-\frac{\partial M_p}{\partial \dot{\alpha}} - y'\frac{\partial F}{\partial \dot{\alpha}}\right) & \left(-\frac{\partial M_p}{\partial \dot{\beta}} - y'\frac{\partial F}{\partial \dot{\beta}}\right) \\ \left(-\frac{\partial M_r}{\partial \dot{z}} + x'\frac{\partial F}{\partial \dot{z}}\right) & \left(-\frac{\partial M_r}{\partial \dot{\alpha}} + x'\frac{\partial F}{\partial \dot{\alpha}}\right) & \left(-\frac{\partial M_r}{\partial \dot{\beta}} + x'\frac{\partial F}{\partial \dot{\beta}}\right) \end{bmatrix} \tag{3.5}$$

$$[K] = \begin{bmatrix} \left(k_z - \frac{\partial F}{\partial z}\right) & \left(k_z y' - \frac{\partial F}{\partial \alpha}\right) & \left(k_z x' - \frac{\partial F}{\partial \beta}\right) \\ \left(k_z y' - \frac{\partial M_p}{\partial z} - y'\frac{\partial F}{\partial z}\right) & \left(k_\alpha + k_z y'^2 + k_z z'^2 - \frac{\partial M_p}{\partial \alpha} - y'\frac{\partial F}{\partial \alpha}\right) & \left(k_z x'y' - \frac{\partial M_p}{\partial \beta} - y'\frac{\partial F}{\partial \beta}\right) \\ \left(k_z x' - \frac{\partial M_r}{\partial z} - x'\frac{\partial F}{\partial z}\right) & \left(k_z x'y' - \frac{\partial M_r}{\partial \alpha} - x'\frac{\partial F}{\partial \alpha}\right) & \left(k_\beta + k_z z'^2 + k_z x'^2 - \frac{\partial M_r}{\partial \beta} - x'\frac{\partial F}{\partial \beta}\right) \end{bmatrix}.$$

Solving these equations presents several difficulties. First, the presence of damping makes traditional methods of uncoupling the equations of motion ineffective, except for very special forms of damping, which are not expected to exist in the general slider bearing case (89). Secondly, the stiffness and damping matrices are, in general, non-symmetric because of the non-symmetric contributions of the slider bearing. Finally, both the stiffness and damping matrices depend on the frequency of slider motion, thus rendering the eigenvalue problem associated with Equation 3.4 non-linear.

3.2 Formulation of the Eigenvalue Problem in 2-N Space

In order to facilitate the computation of modal damping, and to provide a means for attempting to uncouple the equations of motion, the eigenvalue problem associated with equation 3.4 is first reformulated as a 2-N space problem, using generalized velocities as auxiliary variables, as shown in Equations 3.6 and 3.7. The 2-N first order ordinary differential equations resulting from the transformation of Equation (3.4) are expressed in matrix form as follows: (Frequency-dependence of $[K]$ and $[C]$ is temporarily neglected.)

$$[R]\{\dot{y}(t)\} + [S]\{y(t)\} = \{0\} \tag{3.6}$$

where

$$\{y(t)\} = \begin{Bmatrix} \{\dot{\xi}(t)\} \\ \{\xi(t)\} \end{Bmatrix}$$

$$[R] = \begin{bmatrix} [0] & [M] \\ [M] & [C] \end{bmatrix} \tag{3.7}$$

$$[S] = \begin{bmatrix} -[M] & [0] \\ [0] & [K] \end{bmatrix} .$$

From Equation 3.5, $[K]$ and $[C]$ can be seen to be non-symmetric, thus rendering $[R]$ and $[S]$, Equation 3.7, non-symmetric as well. Conventional orthogonality relations, such as those presented by Meirovitch (90) depend on symmetry of $[R]$ and $[S]$, and thus do not apply in this case. For this non-symmetric case, the appropriate similarity transformation for de-coupling the equations of motion is developed in terms of the left and right eigenvalue problems. Let the response vector $\{y(t)\}$ take the following form,

$$\{y(t)\} = \{\gamma\}e^{\alpha t} . \tag{3.8}$$

Combining 3.6 and 3.8 yields the following:

$$\alpha[R]\{\gamma\} + [S]\{\gamma\} = \{0\} , \tag{3.9}$$

which can be written in the form

$$[D]\{\gamma\} = -\alpha\{\gamma\} , \tag{3.10}$$

where

$$[D] = [R]^{-1}[S] \,. \tag{3.11}$$

Equation 3.11 represents the conventional or "right" eigenvalue problem.

The transpose of the dynamical matrix, $[D]^T$, has the same eigenvalues as $[D]$, but different eigenvectors. Thus, the following "left" eigenvalue problem can also be written.

$$[D]^T\{\hat{\gamma}\} = -\alpha\{\hat{\gamma}\} \tag{3.12}$$

or

$$\{\hat{\gamma}\}^T[D] = -\alpha\{\hat{\gamma}\}^T \,, \tag{3.13}$$

where

$$\{\hat{\gamma}\} = \text{left eigenvector} \,. \tag{3.14}$$

The eigensolutions to equations 3.10 and 3.13 have, respectively, the following forms,

$$[D]\{\gamma_i\} = -\alpha_i\{\gamma_i\} \tag{3.15}$$

$$\{\hat{\gamma}_j\}^T[D] = -\alpha_j\{\hat{\gamma}_j\}^T \,. \tag{3.16}$$

Pre-multiplying Equation 3.15 by $\{\hat{\gamma}_j\}^T$ and post-multiplying Equation 3.16 by $\{\gamma_i\}$ yields the following pair of equations.

$$\{\hat{\gamma}_j\}^T[D]\{\gamma_i\} = -\alpha_i\{\hat{\gamma}_j\}^T\{\gamma_i\} \tag{3.17}$$

$$\{\hat{\gamma}_j\}^T[D]\{\gamma_i\} = -\alpha_j\{\hat{\gamma}_j\}^T\{\gamma_i\} \tag{3.18}$$

Subtracting Equation 3.17 from Equation 3.18 yields the bi-orthogonality relation for the left and right eigenvectors.

$$\{\hat{\gamma}_j\}^T\{\gamma_i\} = 0 \,; \qquad i \neq j \tag{3.19}$$

In addition, Equations 3.18 and 3.19 imply that

$$\{\hat{\gamma}_j\}^T[D]\{\gamma_i\} = 0 \,; \qquad i \neq j \,. \tag{3.20}$$

The relationships in Equations 3.19 and 3.20 will be used to decouple the equations of motion for the slider-bearing system.

3.3 Solution of the Frequency Dependent Eigenvalue Problem

Of the solution difficulties discussed in section 3.1, the third and most challenging is the frequency dependence of the eigenvalue problem. Because the damping ς_i, Equation 3.22, is generally quite small, especially for the unstable modes, the analysis is greatly simplified by using only the imaginary portion of the complex eigenvalue α_i in evaluating $[D]$.

The complete form of the eigenvalue problems of Equations 3.15 and 3.16 are written

$$\begin{aligned} \left[D\left(I_m(\alpha_i)\right)\right]\{\gamma_i\} &= -\alpha_i\{\gamma_i\} \\ \{\hat{\gamma}_j\}^T\left[D\left(I_m(\alpha_i)\right)\right] &= -\alpha_j\{\hat{\gamma}_j\}^T \ , \end{aligned} \tag{3.21}$$

where

$$\begin{aligned} \alpha_i &= \varsigma_i\omega_i + i\omega_i\sqrt{1-\varsigma_i^2} \\ \omega_{d_i} &= \omega_i\sqrt{1-\varsigma_i^2} \end{aligned} \tag{3.22}$$

are the complex eigenvalues. Thus, both the left and right eigenproblems are non-linear, and require an iterative solution technique.

The technique chosen for the non-linear eigenproblem involves a combination of root bracketing, and Brent's method. First, the finite element perturbation technique is used to generate tables of stiffness and damping values for a range of frequencies. Cubic spline interpolation then provides the eigensolution algorithm with a continuous range of values for these quantities. Once the stiffness and damping matrices have been computed at a given frequency, the 2-N matrices $[R]$ and $[S]$ can be assembled. These are then used to compute the dynamical matrix, $[D]$, in Equation 3.11. The complex eigenvalues of $[D]$, at a prescribed frequency, are computed by first converting the matrix to upper Hessenberg form, and then using the QR algorithm. Repeating the above procedure for a range of frequencies allows the roots to be bracketed.

Once the roots have been located in this manner, Brent's method is used to converge to the precise value of damped natural frequency in each bracket. Brent's method uses a combination of bisection and quadratic interpolation to achieve accelerated convergence, while checking periodically to insure that the search remains within the previously computed bracket for the root.

Following computation of the complex eigenvalues, which occur as N complex conjugate pairs, the associated eigenvectors are calculated using inverse iteration. Given an

eigenvalue and a random normalized initial guess for the eigenvector, a new eigenvector is computed and the change from the previous vector is compared with the convergence criteria. This scheme exhibits approximately linear convergence, with a computational load of $O(N^2)$. Because the eigenvalue does not change, it is only necessary to perform an L-U decomposition on the dynamical matrix once; subsequent updates of the eigenvector require only back- substitution. One possible problem with this scheme, peculiar to non-symmetric matrices, is the "defective" case, which may result from an unfortunate initial guess for the eigenvector. This is avoided by computing a growth factor equal to the magnitude of the difference between the initial guess and the first computed eigenvector. When the growth factor is small, the initial guess is altered; only a large growth factor will lead to good convergence.

3.4 Forced Response

By applying a similarity transformation based on the bi-orthogonality relation developed in Section 3.2 to the forced problem arising from Equation 3.4, the equations of motion can be decoupled for a generalized input, and expressed in terms of a sequence of 2-N first-order ordinary differential equations that can be easily solved. Subsequent examination of these equations for specific inputs can be used to identify critical design parameters for the slider bearing system.

Figure 3.2 shows a schematic representation of the mechanical slider-bearing-support system, and the various types of inputs to which it may be subjected. Equation 3.4 for this system may be rewritten as follows:

$$[M]\{\ddot{\xi}(t)\} + [C]\{\dot{\xi}(t)\} + [K]\{\xi(t)\} = \{\mathcal{F}(t)\} , \tag{3.23}$$

where

$$\{\mathcal{F}(t)\} = \{f(t)\} + [k_p]\{\xi_p(t)\} + [C_S]\{\dot{\xi}_d(t)\} + [K_S]\{\xi_d(t)\} . \tag{3.24}$$

Equation 3.6 now becomes

$$[R]\{\dot{y}(t)\} + [S]\{y(t)\} = \{F(t)\} , \tag{3.25}$$

where

$$\{F(t)\} = \left\{ \begin{array}{c} \{0\} \\ \{\mathcal{F}(t)\} \end{array} \right\} . \tag{3.26}$$

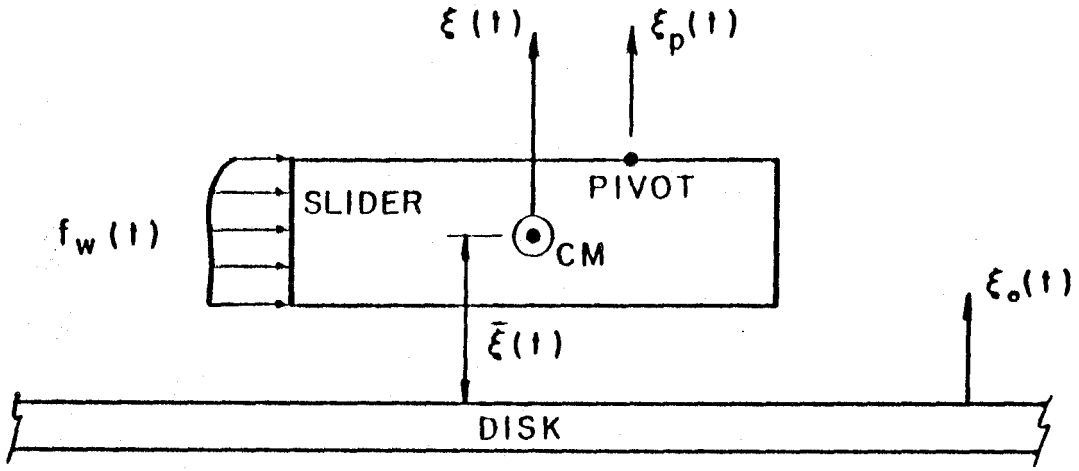

$$\xi(t) \Leftrightarrow \begin{Bmatrix} z(t) \\ \alpha(t) \\ \beta(t) \end{Bmatrix}$$

FIGURE 3.2: FORCED RESPONSE; TYPICAL INPUTS

Premultiplying Equation 3.25 by $[R]^{-1}$ as before yields the following set of 2-N equations for the forced problem

$$\{\dot{y}(t)\} + [D]\{y(t)\} = [R]^{-1}\{F(t)\} \tag{3.27}$$

with $[D]$ defined by Equation 3.11 as before. Equation 3.27 is uncoupled by first assuming a solution of the form

$$\{y(t)\} = \sum_{r=1}^{2N} \{\gamma_r\} q_r(t) = [G]\{q(t)\} \; . \tag{3.28}$$

The columns of the modal matrix, $[G]$, are the right eigenvectors, $\{\gamma\}$, obtained from the homogeneous solution. The elements of the column vector, $\{q(t)\}$, consist of $2N$ generalized displacements, which are to be determined. Substituting Equation 3.28 into 3.27 and premultiplying the result by $[\hat{G}]^T$ yields the following:

$$[\hat{G}]^T[G]\{\dot{q}(t)\} + [\hat{G}]^T[D][G]\{q(t)\} = [\hat{G}]^T[R]^{-1}\{F(t)\} \; , \tag{3.29}$$

where $[\hat{G}]$ is the left-modal matrix, formulated from the solution eigenvectors of the left eigenproblem.

The bi-orthogonality relations in Equations 3.19 and 3.20 permit the following definitions to be made.

$$\begin{aligned} [g^*] &\equiv [\hat{G}]^T[G] = \text{diagonal matrix} \\ [d^*] &\equiv [\hat{G}]^T[D][G] = \text{diagonal matrix} \\ \{Q(t)\} &\equiv [\hat{G}]^T[R]^{-1}\{F(t)\} = [\hat{G}]^T \begin{Bmatrix} \{[M]^{-1}\mathcal{F}(t)\} \\ \{0\} \end{Bmatrix} \end{aligned} \tag{3.30}$$

Equations 3.30 and 3.17 imply that

$$d_r^* = -\alpha_r g_r^* \; . \tag{3.31}$$

Combining Equations 3.29, 3.30, and 3.31 results in the following for the r-th uncoupled, forced response equation.

$$\dot{q}_r(t) - \alpha_r q_r(t) = \frac{1}{g_r^*} Q_r(t) \; ; \qquad r = 1, 2, \ldots, 2N \tag{3.32}$$

Assuming the initial conditions to be zero, the solution to Equation 3.32 can be written in terms of the following convolution integral.

$$q_r(t) = \frac{1}{g_r^*} \int_0^t Q_r(\tau) e^{\alpha_r(t-\tau)} d\tau \tag{3.33}$$

In order to solve for the displacements, $\{\xi(t)\}$, consider the definition of $\{y(t)\}$ in Equation 3.28,

$$\{y(t)\} = \begin{Bmatrix} \{\dot{\xi}(t)\} \\ \{\xi(t)\} \end{Bmatrix} = [G]\{q(t)\} = \begin{bmatrix} [\alpha\eta] \\ [\eta] \end{bmatrix} \{q(t)\} , \tag{3.34}$$

where the $N \times 2N$ rectangular matrix $[\eta]$ represents the lower half of the modal matrix, $[G]$. The displacement vector can now be written as

$$\begin{aligned} \{\xi(t)\} &= [\eta]\{q(t)\} \\ &= \sum_{r=1}^{2N} \{\eta_r\} q_r(t) \\ &= \sum_{r=1}^{2N} \{\eta_r\} \frac{1}{g_r^*} \int_0^t Q_r(\tau) e^{\alpha_r(t-\tau)} d\tau . \end{aligned} \tag{3.35}$$

Assuming that the eigenvectors defining the modes of the system occur in pairs as complex conjugates, they can be ordered such that the $(r+1)$-th mode is the complex conjugate of the r-th mode. The final solution is simplified by the following complex vector notation.

$$g_r^* = |g_r^*| e^{i\theta_r^g} ; \qquad g_{r+1}^* = |g_r^*| e^{-i\theta_r^g} \tag{3.36}$$

$$\{\eta_r^j\} = \{|\eta_r^j| e^{i\theta_r^j}\} ; \qquad \{\eta_{r+1}^j\} = \{|\eta_r^j| e^{-i\theta_r^j}\} \tag{3.37}$$

$$Q_r(t) = |Q_r(t)| e^{i\theta_r^q} ; \qquad Q_{r+1}(t) = |Q_r(t)| e^{-i\theta_r^q} \tag{3.38}$$

$$\alpha_r = \varsigma_r\omega_r + i\omega_r\sqrt{1-\varsigma_r^2} ; \qquad \alpha_{r+1} = \varsigma_r\omega_r - i\omega_r\sqrt{1-\varsigma_r^2} \tag{3.39}$$

Combining Equations 3.35 through 3.39 yields the following solution for the displacement vector.

$$\begin{aligned} \{\xi_j(t)\} = \sum_{r=1,3,\ldots}^{2N-1} \frac{2}{|g_r^*|} \int_0^t |Q_r(\tau)| e^{-\varsigma_r\omega_r(t-\tau)} \\ \left\{ |\eta_r^j| \cos\left[\omega_r\sqrt{1-\varsigma_r^2}(t-\tau) + \theta_r^g - \theta_r^q - \theta_r^j\right] \right\} d\tau \end{aligned} \tag{3.40}$$

Equation 3.40 expresses the displacement vector for the slider-bearing-support system for any combination of pivot point displacement, disk surface displacement, and/or applied loading on the slider body. Once the loading function, $\{\mathcal{F}(t)\}$, has been evaluated from Equation 3.24, Equations 3.26 and 3.30 can be used to compute $\{Q(t)\}$. This is then used

in Equation 3.40, together with the eigenvalues, α_r, and the corresponding eigenvectors, $\{\eta_r\}$, to compute the displacements of the center of mass of the slider body.

3.5 Response to Periodic Disk Displacement

The motion of the disk surface is primarily periodic in nature. This motion is due to many factors, including the out-of-flatness of the disk, which produces displacement at the frequency of rotation, as well as the vibrations of the disk at its natural frequencies. One of the principal requirements for slider bearings is that they maintain an approximately constant spacing between the magnetic transducer and the disk in order to insure error-free transmission of data. It is thus worthwhile to examine the elements of slider-bearing design, which have the greatest influence on spacing.

Consider the case of sinusoidal disk motion, where the displacement vector is written as

$$\{\xi_d(t)\} = \{\bar{\xi}_d\} \sin \omega_o t \ . \tag{3.41}$$

Equation 3.24 for the total forcing function now becomes

$$\{\mathcal{F}(t)\} = \omega_o [C_S]\{\bar{\xi}_d\} \cos \omega_o t + [K_S]\{\bar{\xi}_d\} \sin \omega_o t \ , \tag{3.42}$$

and Equation 3.30 implies

$$\{Q(t)\} = [\hat{\eta}]^T \left\{ \{D_1\} \cos \omega_o t + \{D_2\} \sin \omega_o t \right\} \ , \tag{3.43}$$

where

$$\begin{aligned} \{D_1\} &= \omega_o [M]^{-1} [C_S]\{\bar{\xi}_d\} \\ \{D_2\} &= [M]^{-1} [K_S]\{\bar{\xi}_d\} \end{aligned} \tag{3.44}$$

and $[\hat{\eta}]$ is the upper portion of the left-modal matrix, $[\hat{G}]$.

3.6 Response to a Random Input

In its normal operating environment, the slider-bearing system may experience random inputs that are due to disk motion, support displacement and/or buffeting of the slider body by the air flow in the disk-drive enclosure. Consider a random excitation of the slider system such that the equations of motion can be written as follows:

$$[M]\{\ddot{\xi}(t)\} + [C]\{\dot{\xi}(t)\} + [K]\{\xi(t)\} = \{\mathcal{R}(t)\} \ , \tag{3.45}$$

where $\{\mathcal{R}(t)\}$ is an ergodic random forcing function, and $\{\xi(t)\}$ represents the random displacement response. Using the same $2N$ space modal analysis as before to uncouple the equations of motion, the following expression for $Q_r(t)$ is obtained.

$$Q_r(t) = \{\hat{\eta}_r\}^T [M]^{-1} \{\mathcal{R}(t)\} \tag{3.46}$$

The response mean-square value for this input is obtained as follows:

$$\overline{\xi_i^2(t)} = \frac{1}{2\pi} \sum_{r=1}^{2N} \sum_{s=1}^{2N} \eta_r^i \eta_s^i \int_{-\infty}^{\infty} \frac{\Psi_{rs}(\omega) d\omega}{[\varsigma_r \varsigma_s \omega_r \omega_s + (\omega - \omega_{d_r})(\omega - \omega_{d_s})]} , \tag{3.47}$$

where $\Psi_{rs}(\omega)$ is the Fourier transform of the cross-correlation function of the generalized excitation, $\psi_{rs}(\tau)$, given by

$$\psi_{rs}(\tau) = \lim_{T \to \infty} \frac{1}{T} \int_{-T/2}^{T/2} \{\hat{\eta}_r\}^T [M]^{-1} \{\mathcal{R}(t)\} \{\hat{\eta}_s\}^T [M]^{-1} \{\mathcal{R}(t-\tau)\} dt . \tag{3.48}$$

The quantities in the denominator of 3.48 are defined in terms of the complex eigenvalues as shown in Equation 3.22.

3.7 Summary

In this chapter, the stiffness and damping matrices of the slider gas bearing have been used, together with the dynamical properties of the slider body and support system, to develop the equations of motion of the slider for three degrees of freedom: vertical displacement perpendicular to the disk surface, angular displacement in pitch about the transverse axis, and angular displacement in roll about the longitudinal axis. The problem was transformed into a $2N$-space problem in order to compute modal damping, and the resulting nonlinear eigenproblem was solved using an iterative technique. An approximate similarity transformation based on the left and right modal matrices of the homogeneous problem was then used in uncoupling the equations of motion for forced response. Finally, the particular cases of periodic disk surface displacement and of generalized ergodic random input were examined.

CHAPTER 4

SOME APPLICATIONS OF THE THEORY

4.1 Introduction

The theory developed in this thesis permits calculation of the natural frequencies and mode shapes of a slider-bearing system about its equilibrium operating position. By examining a number of such positions, it is possible to ascertain numerically the effects of pitch angle, yaw angle, and minimum spacing. The stiffness and damping properties of the slider bearing are computed from the in-phase and out-of-phase components of perturbation pressure, and thus the perturbation pressure fields determine how the slider-bearing geometry contributes to these important dynamic properties.

This chapter begins by comparing the plane wedge and taper-flat slider pad geometries. Differences in static pressure and in perturbation pressures for a coupled, pitch-heave mode of oscillation are used to draw conclusions about the effect of bearing geometry on stiffness and damping properties. The dynamic response of these two slider-bearing pads, for various conditions of yaw angle, pitch angle, and minimum spacing, are also discussed. Comparison of these two designs serves to help establish the relationship between bearing-film geometry, the distribution of the static and perturbation pressures, and their ultimate effect on the dynamic properties of the lubricating film.

The remainder of Chapter 4 is devoted to the evaluation of the IBM Model 2314 slider, representing one of the earliest self-acting, bearing designs, and the IBM Model 3370, which is currently in wide use in the disk-drive industry. The dynamic behavior of each is computed for its typical operating conditions, and the characteristics of the two are compared. Additional response calculations for the IBM Model 3370 demonstrate the application of the forced-response model.

4.2 Effect of Bearing Geometry on Static Performance

The static performance of the slider bearing is characterized by the total pressure developed when the slider is at equilibrium. The integral of this pressure over the slider-bearing surface determines the bearing load, while the center of pressure represents the point about which this pressure distribution exerts no moment in pitch. The gas-film

geometries and disk velocity used in computing the static performance data are shown in Figures 4.1 and 4.2.

One of the simplest possible slider-bearing film geometries is the plane wedge, shown in Figure 4.1. The flat bearing, at an angle relative to the disk surface, forms a converging channel for the oncoming flow. This simple geometry is one of the easiest to manufacture, and the linear height profile $H(X, Y)$ makes analysis straightforward. A major disadvantage of the plane wedge is the complete loss of hydrodynamic pressure at zero pitch angle, when the slider surface is parallel to the disk.

A modified version of the plane-wedge slider pad is used in the majority of disk drives manufactured today. This pad geometry is shown in Figure 4.2. It differs from the plane wedge in that an additional angle is provided at the nose. This inlet taper produces an initial positive pitch moment for slider-bearing systems, which are designed to rest in contact with a stationary disk surface and then "take off" unassisted as the disk begins to rotate. This positive pitch moment can counteract the negative moment that is due to friction with the disk surface and can form a stable, nose-up flying attitude. The inlet taper also prevents loss of the hydrodynamic bearing load at zero pitch angle.

4.2.1 Static Pressure Distribution

The effect of the inlet taper on static pressure distribution in the slider bearing can be seen by comparing Figures 4.3 and 4.4. The colors in these plots indicate the pressure under the slider-bearing pad in atmospheres, according to the scale at the right of each figure. For the same operating conditions, the taper-flat pad develops a slightly higher peak pressure at the tail than the plane-wedge pad does. The taper-flat pad, unlike the plane wedge, also forms a relatively high pressure at the front of the bearing behind the inlet taper. This additional pressure peak not only increases the total bearing load, but also shifts the center of pressure towards the nose of the slider pad.

4.2.2 Bearing Load

The effects of roll-angle change on a single pad are relatively small. Roll angle affects the pressure distributions in the two-pad slider mainly through the resulting vertical displacement of the individual pads. The motions of the slider pad in pitch, and in vertical displacement, are thus of primary interest in relating slider-bearing geometry to static and

FIGURE 4.1: PLANE-WEDGE SLIDER PAD

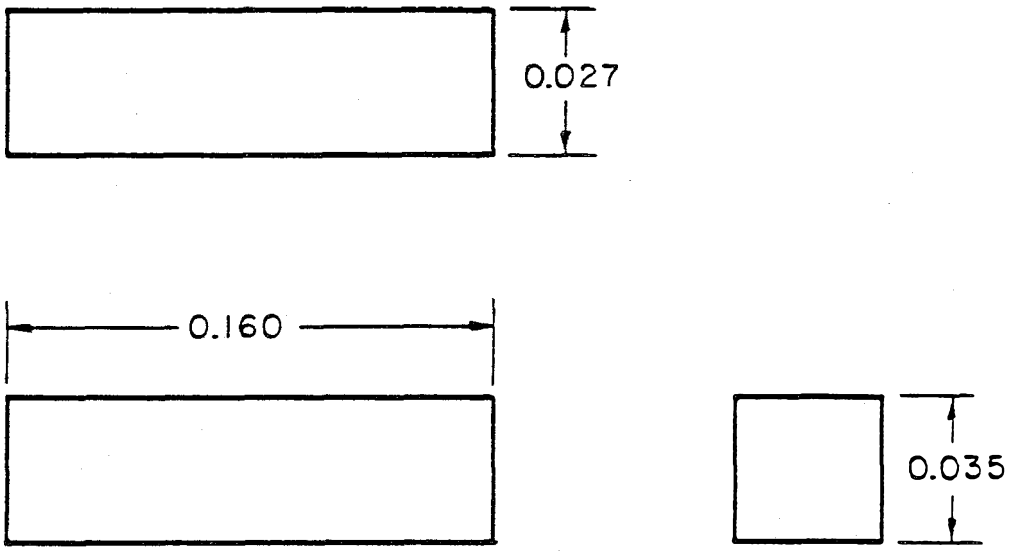

Nominal Operating Parameters:

Surface Speed:	1000 inches/sec
Min. Spacing:	20 μ inches
Pitch Angle:	100 μ radians

FIGURE 4.2: TAPER-FLAT SLIDER PAD

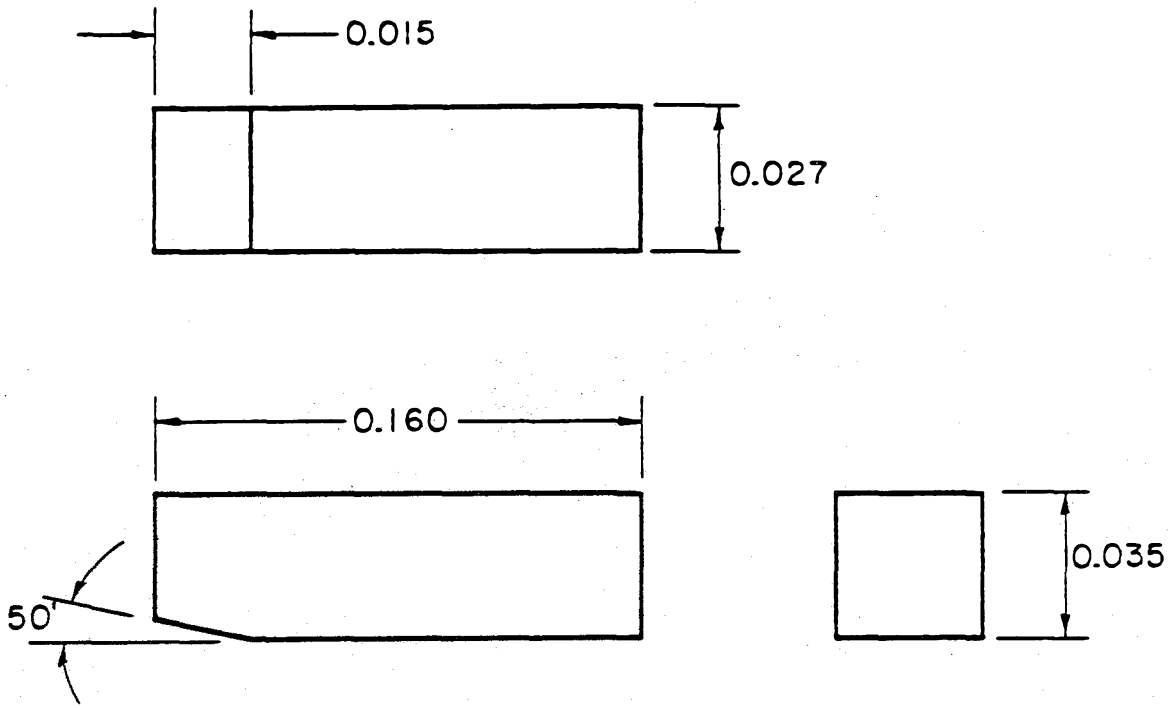

Nominal Operating Parameters:

Surface Speed:	1000 inches/sec
Min. Spacing:	20 μ inches
Pitch Angle:	100 μ radians

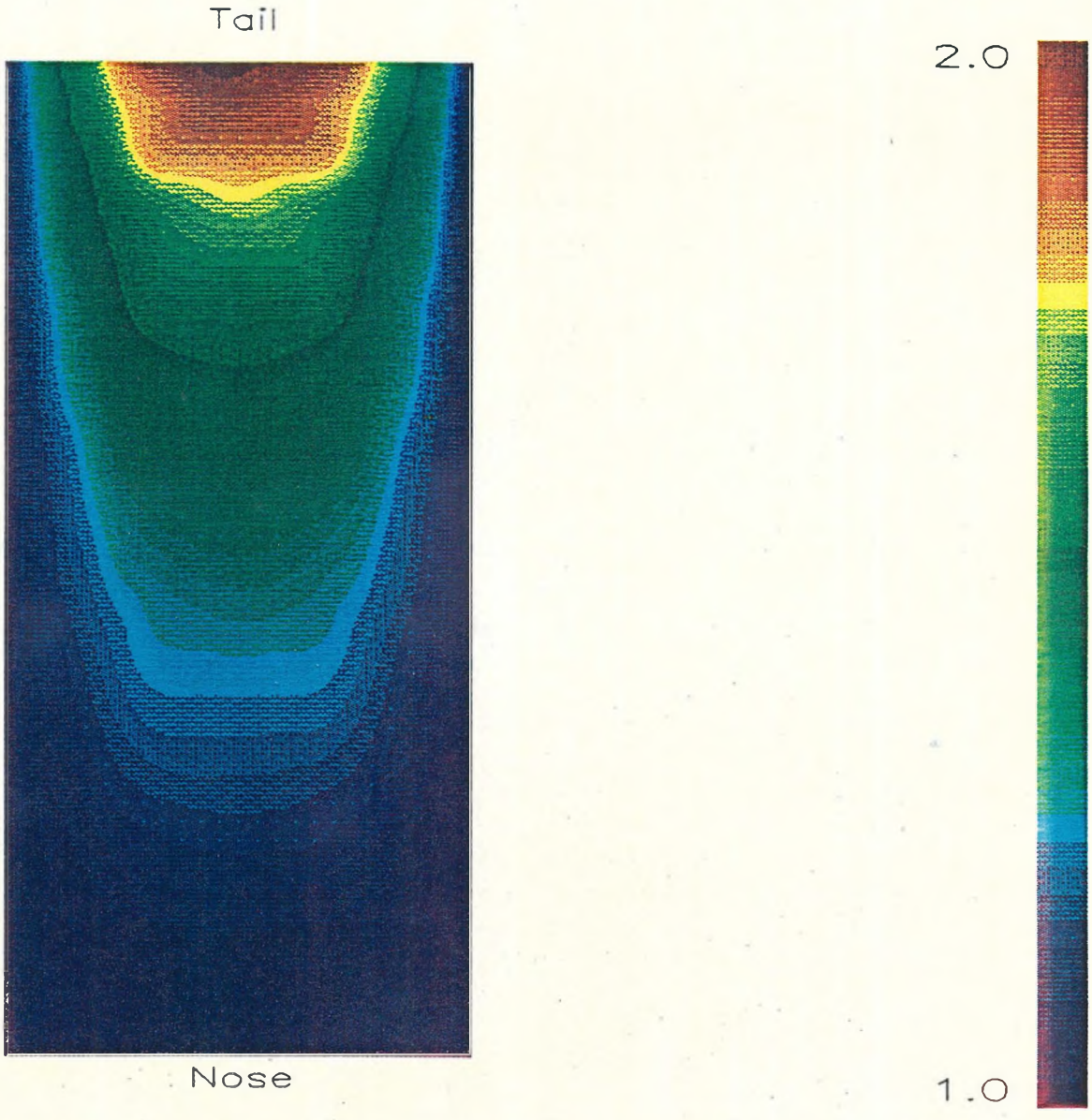

Figure 4.3: Plane Wedge, Static Pressure (atm)

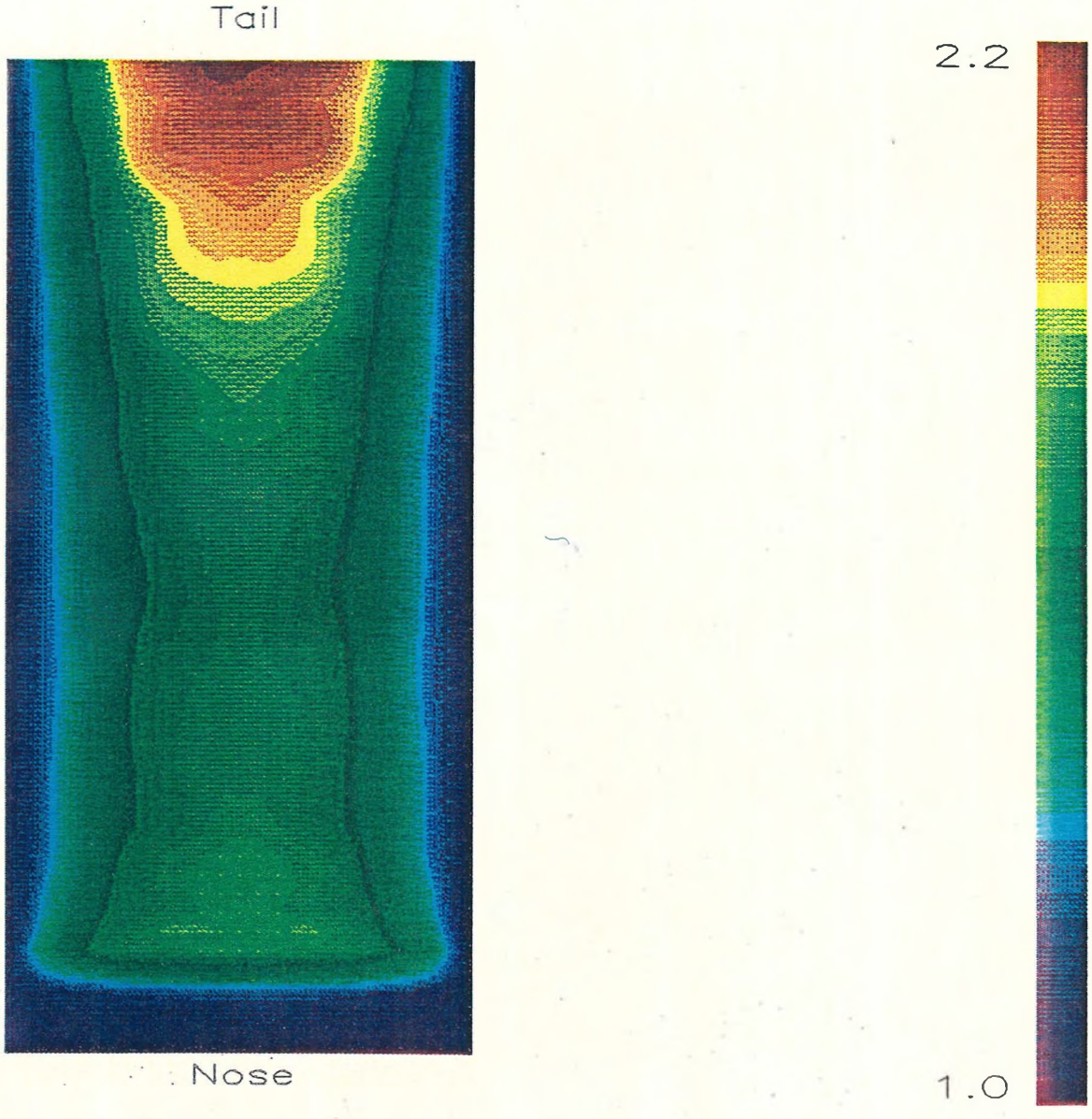

Figure 4.4: Taper Flat, Static Pressure (atm)

dynamic performance. The effects of minimum bearing clearance, pitch angle, and yaw angle on static bearing load are shown in Figures 4.5 through 4.10.

Over the range of tail spacings shown in Figures 4.5 and 4.6, the load curves for the plane-wedge and taper-flat slider-bearing geometries show a similar trend, except that the total load developed by the taper-flat pad is approximately double that of the plane wedge.

The effect of pitch angle on the bearing load for the plane wedge and taper-flat pads is shown in Figures 4.7 and 4.8, respectively. The general trend is opposite for the two different sliders. As the pitch angle of the taper-flat slider is increased, the inlet taper is raised farther from the disk surface, thus losing its load-producing capability. At a pitch angle of 300 microradians, both the taper-flat and plane-wedge pads have similar pressure distributions and nearly the same total bearing load.

Yaw angle effects are particularly important in disk drives that are designed for use in microcomputers. The smaller size of these drives often dictates the use of a swinging-arm device for positioning the slider bearing radially on the disk surface. Such a positioner cannot maintain alignment of the slider bearing with the tangent direction of disk rotation, and the resulting yaw angle influences slider-bearing performance. Increasing the yaw angle reduces the load for both the plane-wedge and the taper-flat geometries, as shown in Figures 4.9 and 4.10. Yawing the slider pad relative to the flow direction causes some of the incoming flow to be directed out the side of the bearing, resulting in a loss of pressure at the tail.

4.2.3 Center of Pressure

The point about which the pitch moment of the pressure distribution is zero, referred to as the center of pressure, is also affected by minimum bearing clearance, pitch angle, and yaw angle, as shown in Figures 4.11 through 4.16. Center of pressure is measured from the tail of the slider-bearing pad, and has units of inches.

Increasing the tail spacing shifts the center of pressure toward the nose of both the plane-wedge and the taper-flat slider bearings, as shown in Figures 4.11 and 4.12. As the spacing becomes larger, the peak pressure at the tail is reduced to a greater degree than the pressure at the nose, and this shifts the center of pressure toward the front. The center of both slider bearing pads is located .080″ from the tail; the center of pressure for the

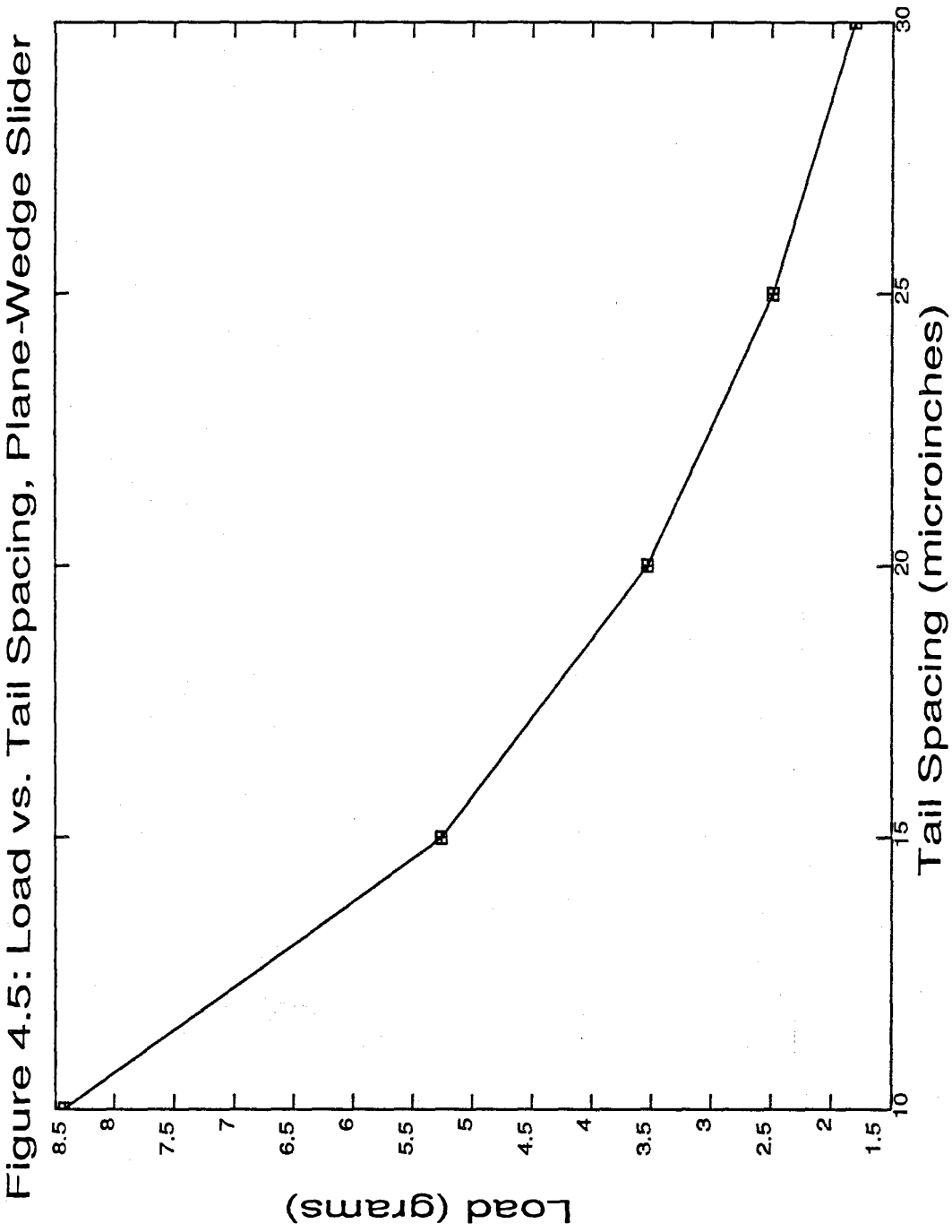

Figure 4.5: Load vs. Tail Spacing, Plane-Wedge Slider

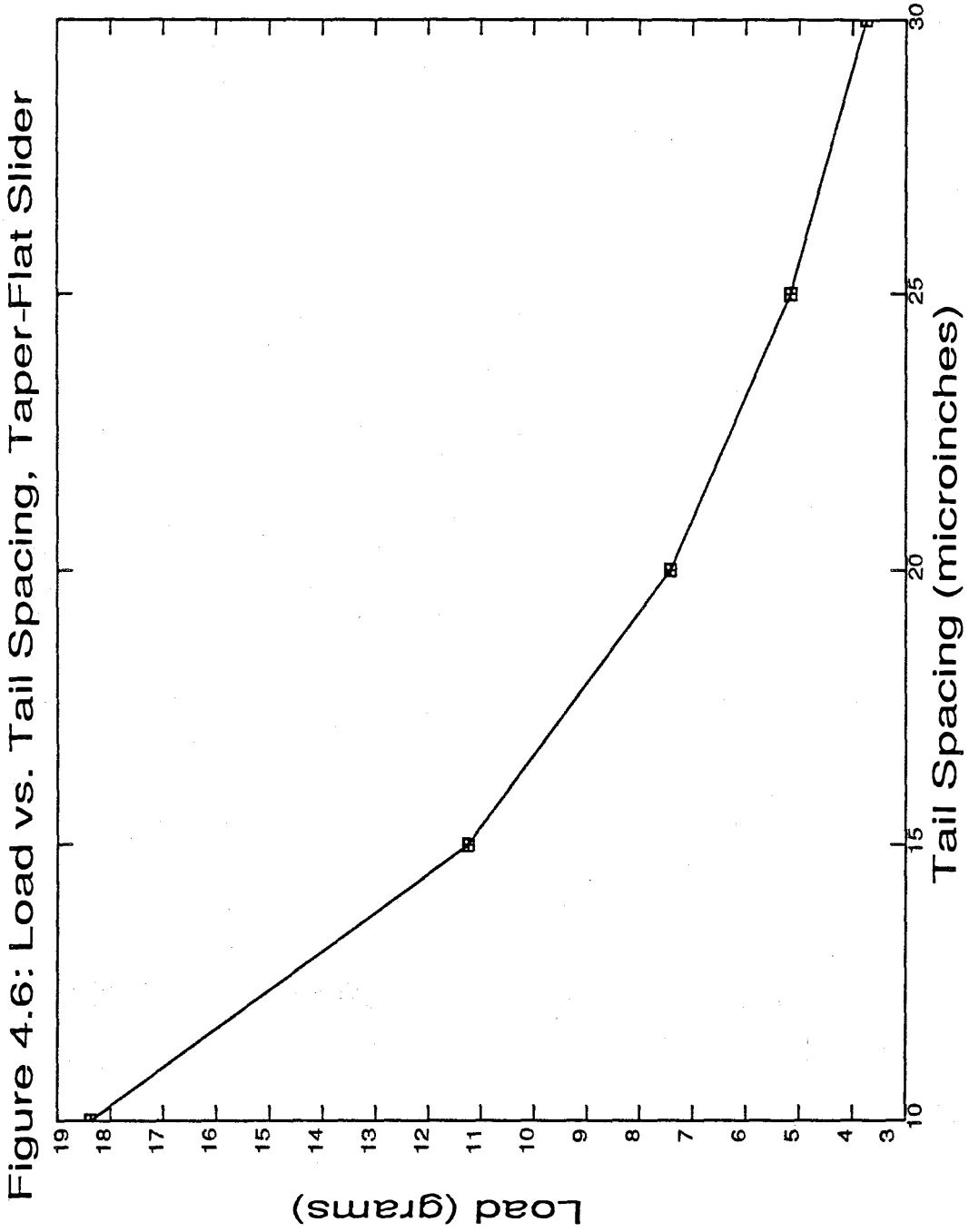

Figure 4.6: Load vs. Tail Spacing, Taper-Flat Slider

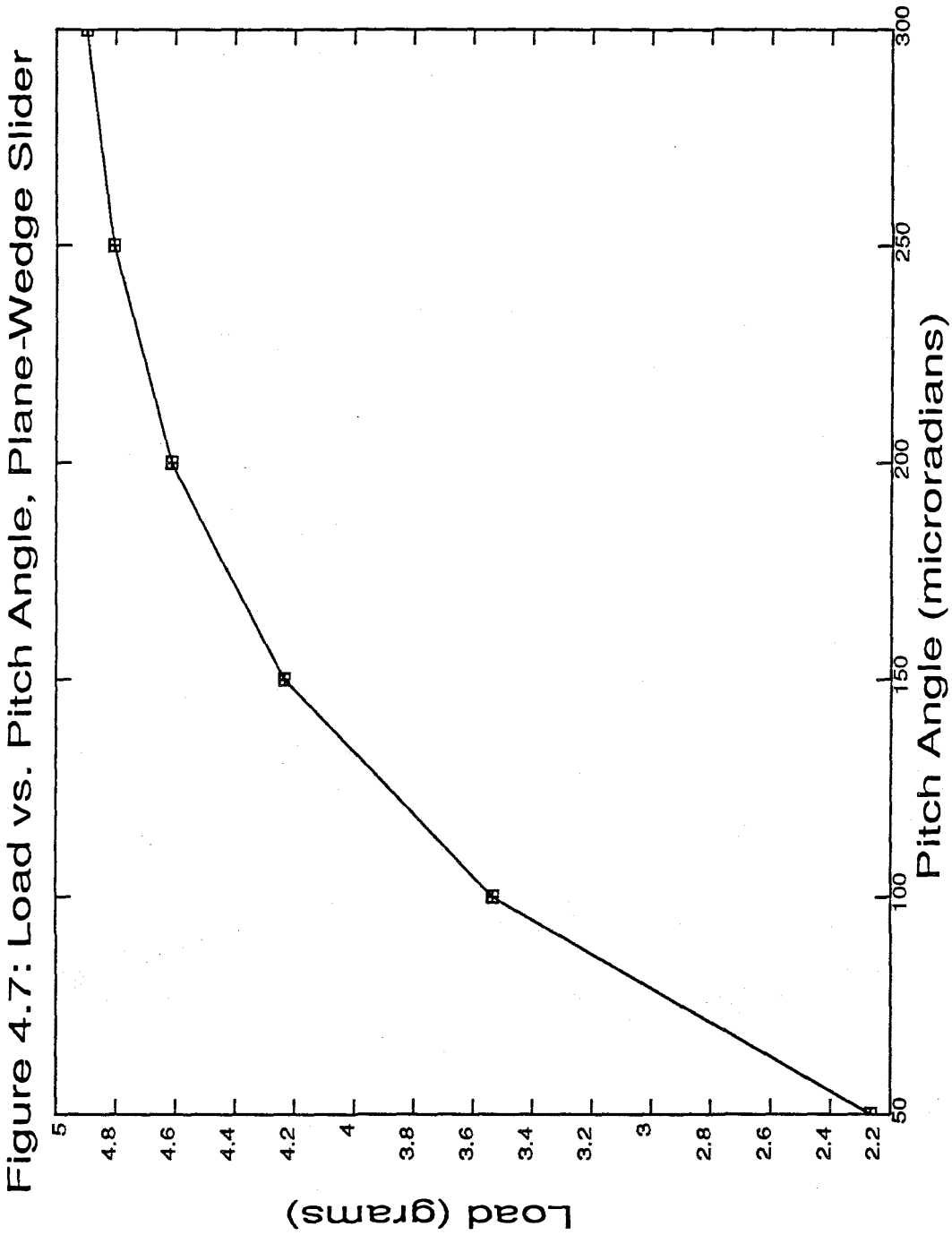

Figure 4.7: Load vs. Pitch Angle, Plane-Wedge Slider

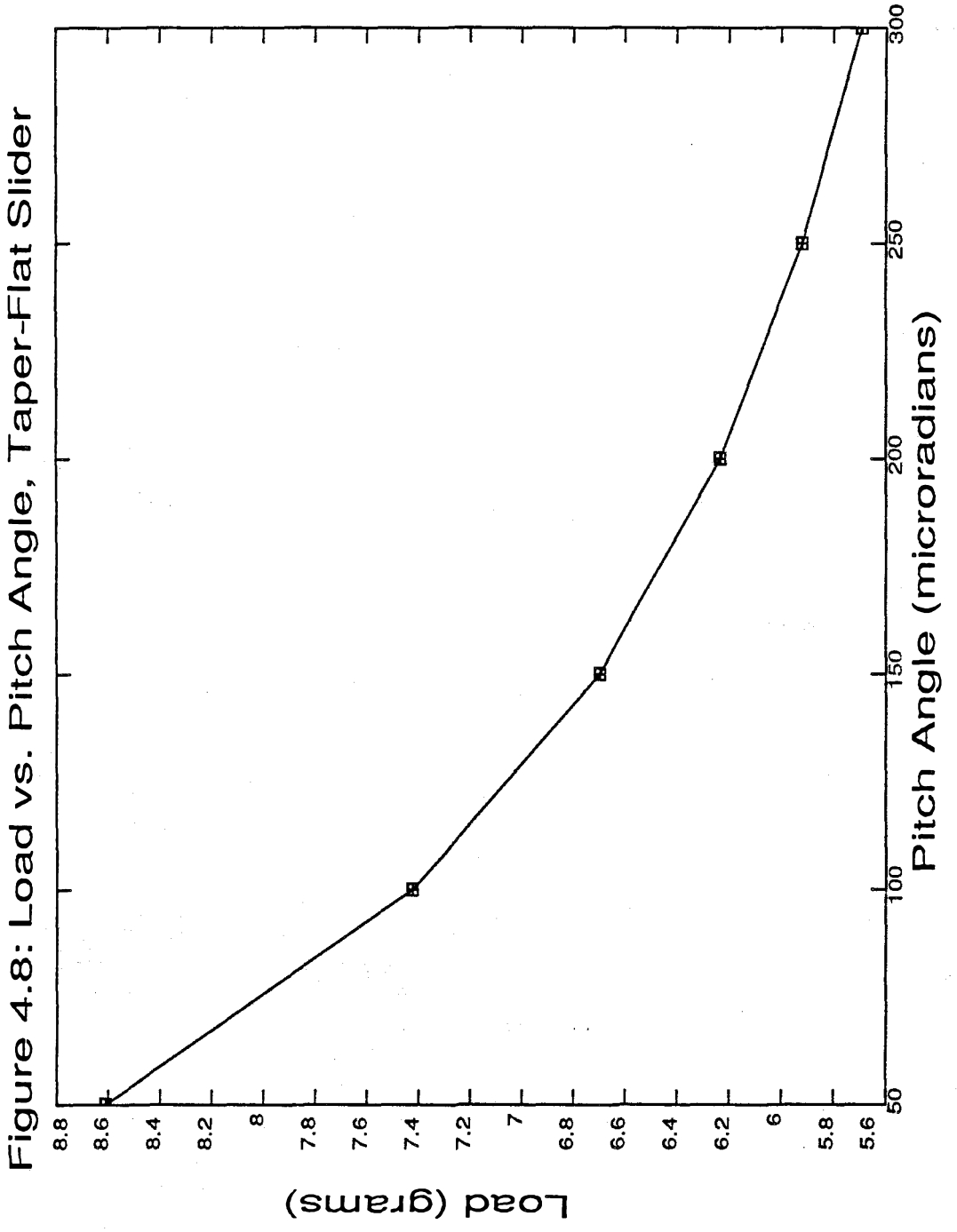

Figure 4.8: Load vs. Pitch Angle, Taper-Flat Slider

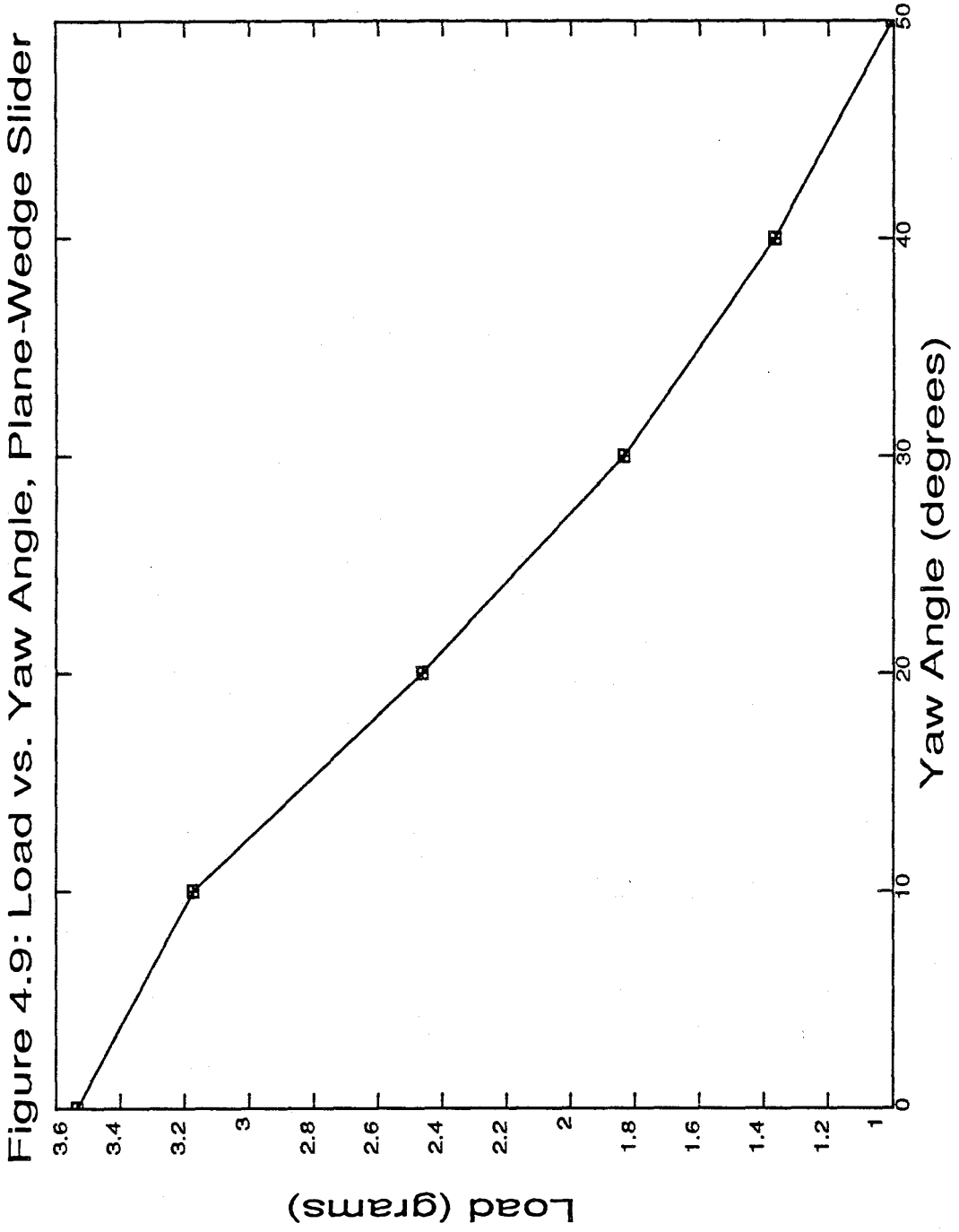

Figure 4.9: Load vs. Yaw Angle, Plane-Wedge Slider

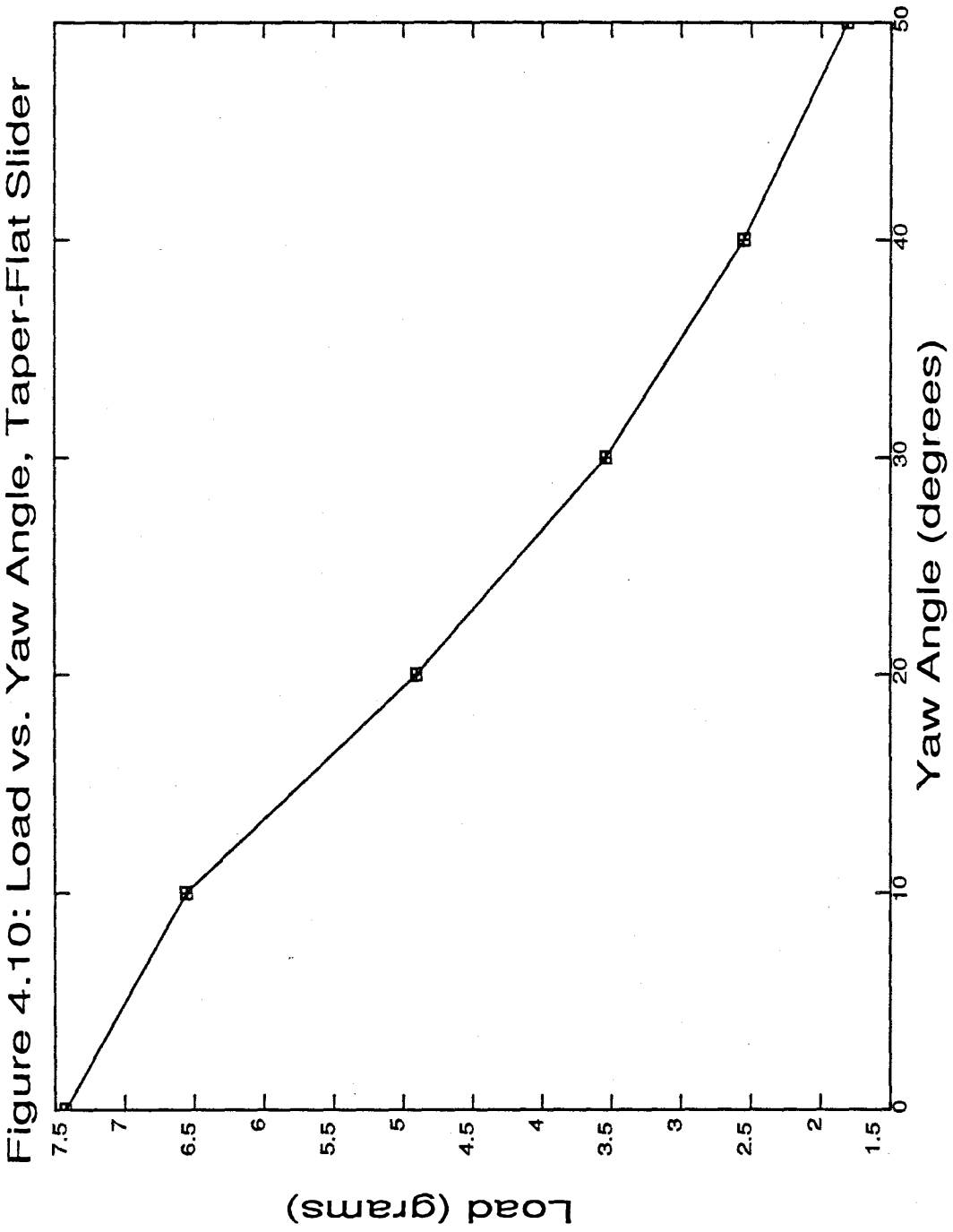

Figure 4.10: Load vs. Yaw Angle, Taper-Flat Slider

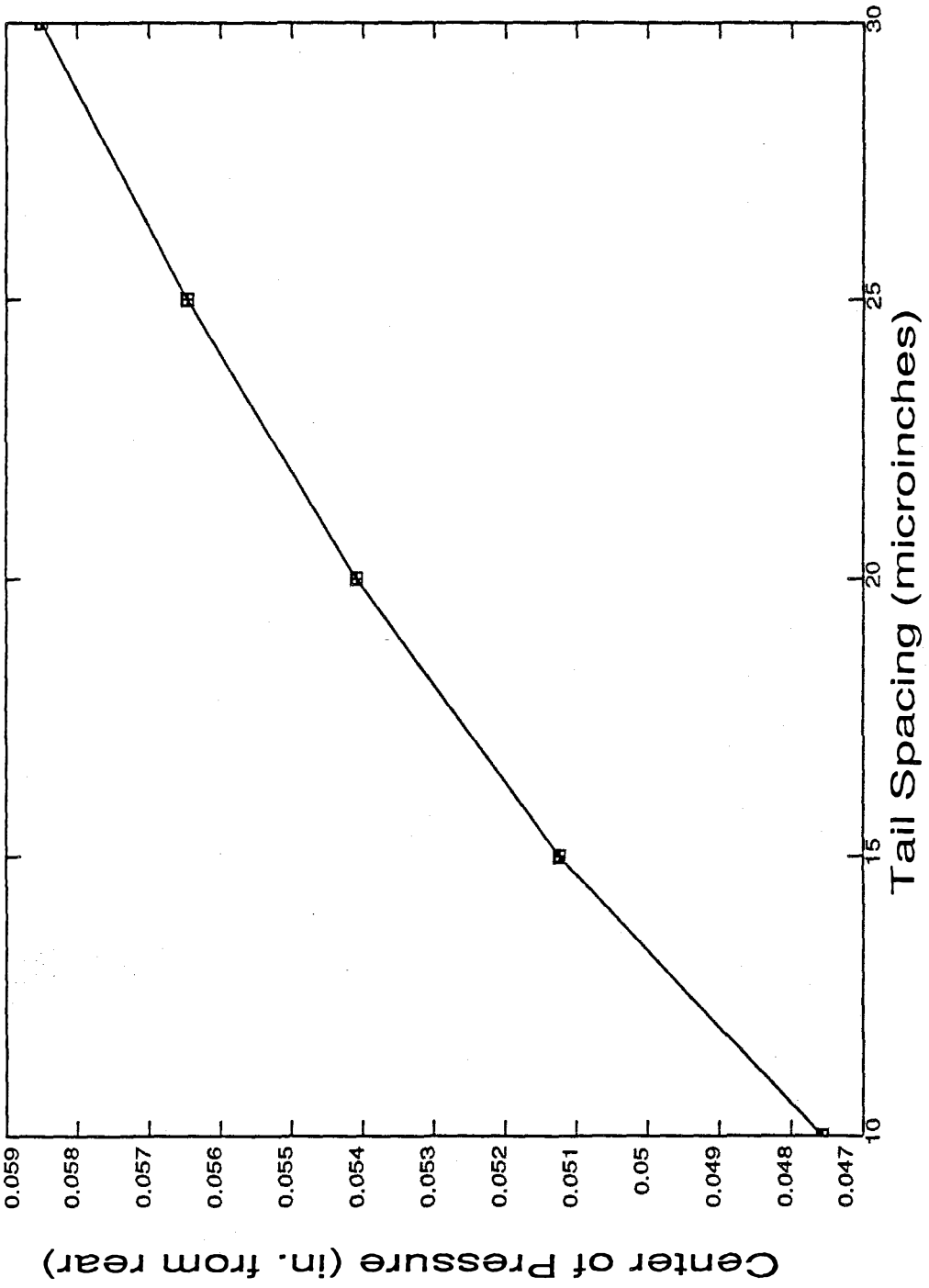

Figure 4.11: Ctr. of Pressure vs. Tail Spacing, Plane-Wedge Slider

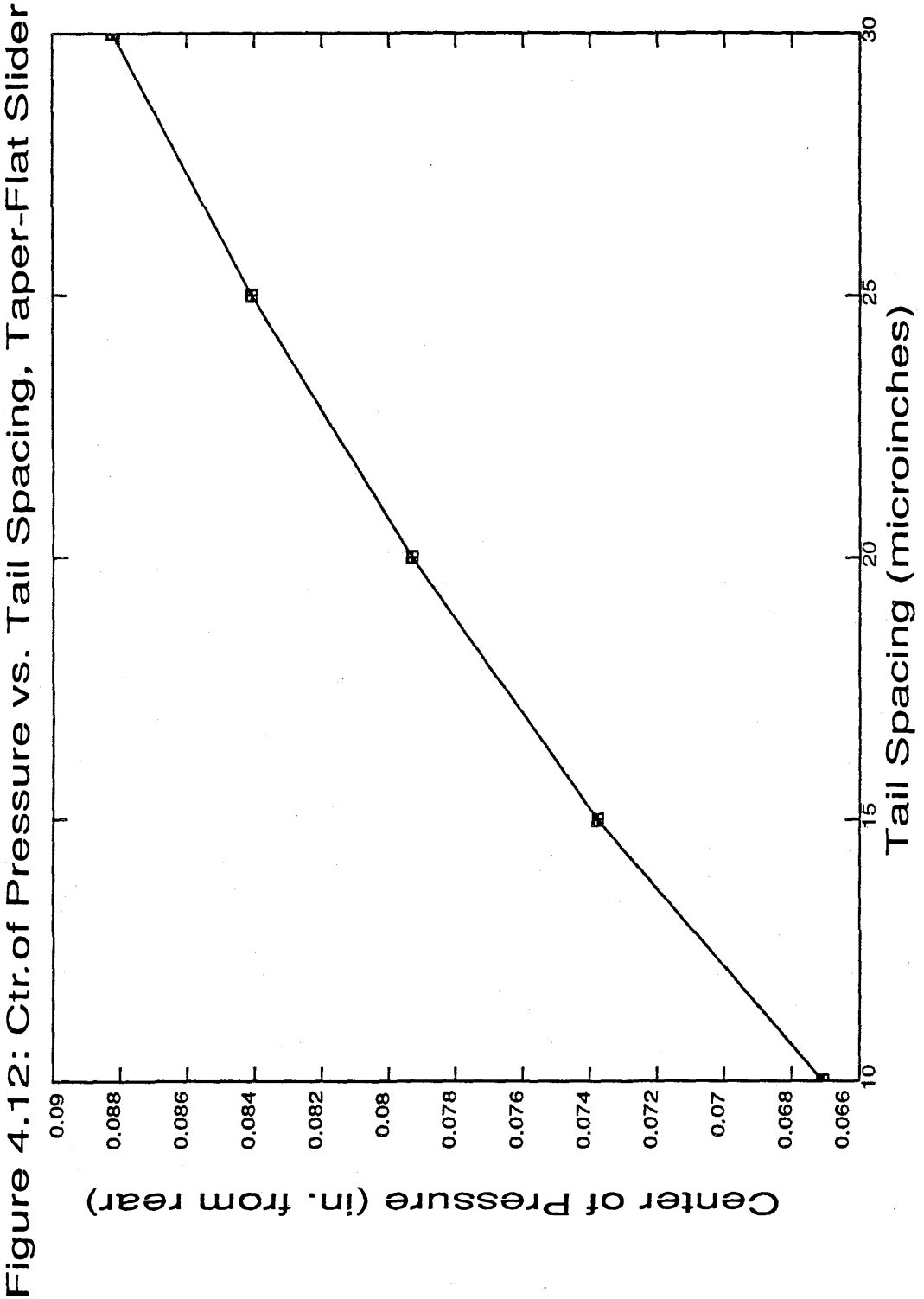

Figure 4.12: Ctr.of Pressure vs. Tail Spacing, Taper-Flat Slider

plane-wedge pad remains behind this point over the range of 10 microinch to 30 microinch tail spacing, while at a tail spacing of 21 microinches, the center of pressure of the taper-flat slider coincides with the geometric center of the pad.

Center of pressure is also affected by pitch angle, as illustrated by Figures 4.13 and 4.14. As the pitch angle is increased, both the plane-wedge and taper-flat slider-bearing pads exhibit a shift of the center of pressure toward the tail, implying a positive pitch stiffness. The center of pressure for the plane-wedge pad remains behind its geometric center for the range of 50 microradians to 300 microradians of pitch. The center of pressure for the taper-flat slider-bearing pad coincides with its geometric center at a pitch angle of 100 microradians.

Figures 4.15 and 4.16 show the effect of yaw angle on the location of the center of pressure for plane-wedge and taper-flat slider-pad geometries. In both cases, the increase in yaw angle decreases the peak pressure at the tail of the slider pad, thus moving the center of pressure toward the nose.

The many factors affecting bearing load and center of pressure, which include minimum spacing, pitch angle, and yaw angle, determine the static, equilibrium operating condition for the slider-bearing system. By performing a perturbation analysis about this equilibrium position, the dynamic performance of the slider-bearing system can be evaluated.

4.3 Effect of Bearing Geometry on Dynamic Performance

The contribution of bearing geometry to slider dynamics is determined by the perturbation pressure fields. The distribution of the in-phase and out-of-phase pressures within the gas film depends on the perturbation of $H(X,Y)$. For evaluation of the stiffness and damping matrices, the gas film is perturbed separately in heave, pitch, and roll for a range of frequencies. These matrices are used in formulating the equations of motion of the entire slider-bearing system.

The eigensolutions of the slider-bearing system define the damped natural frequencies and the corresponding normalized displacement vectors for the slider body. If displaced from equilibrium, the slider body will always oscillate at one or more of these frequencies. When the slider body is in motion at one of its natural frequencies, and in the corresponding mode shape, the gas film is perturbed with the same frequency and shape.

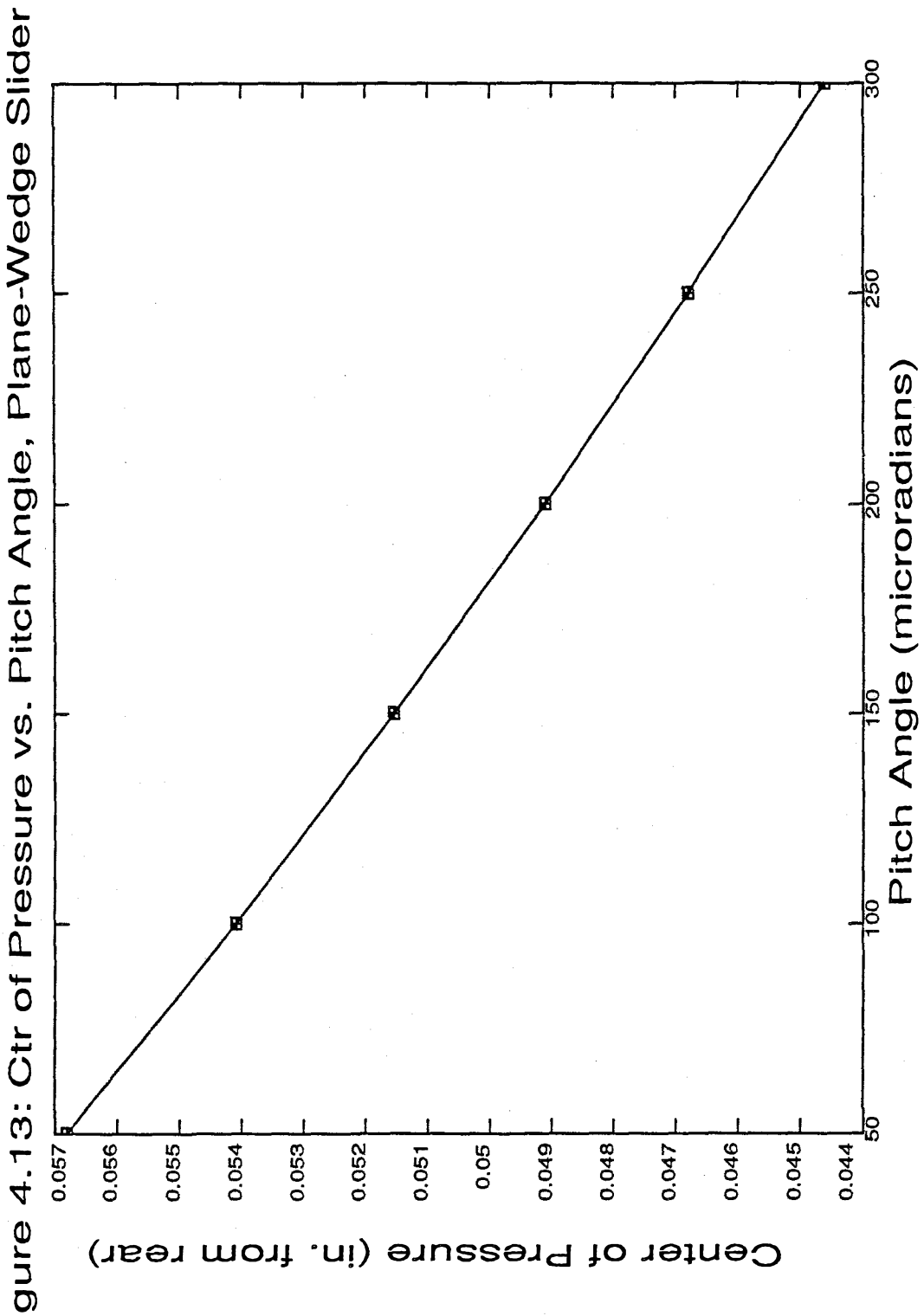

Figure 4.13: Ctr of Pressure vs. Pitch Angle, Plane-Wedge Slider

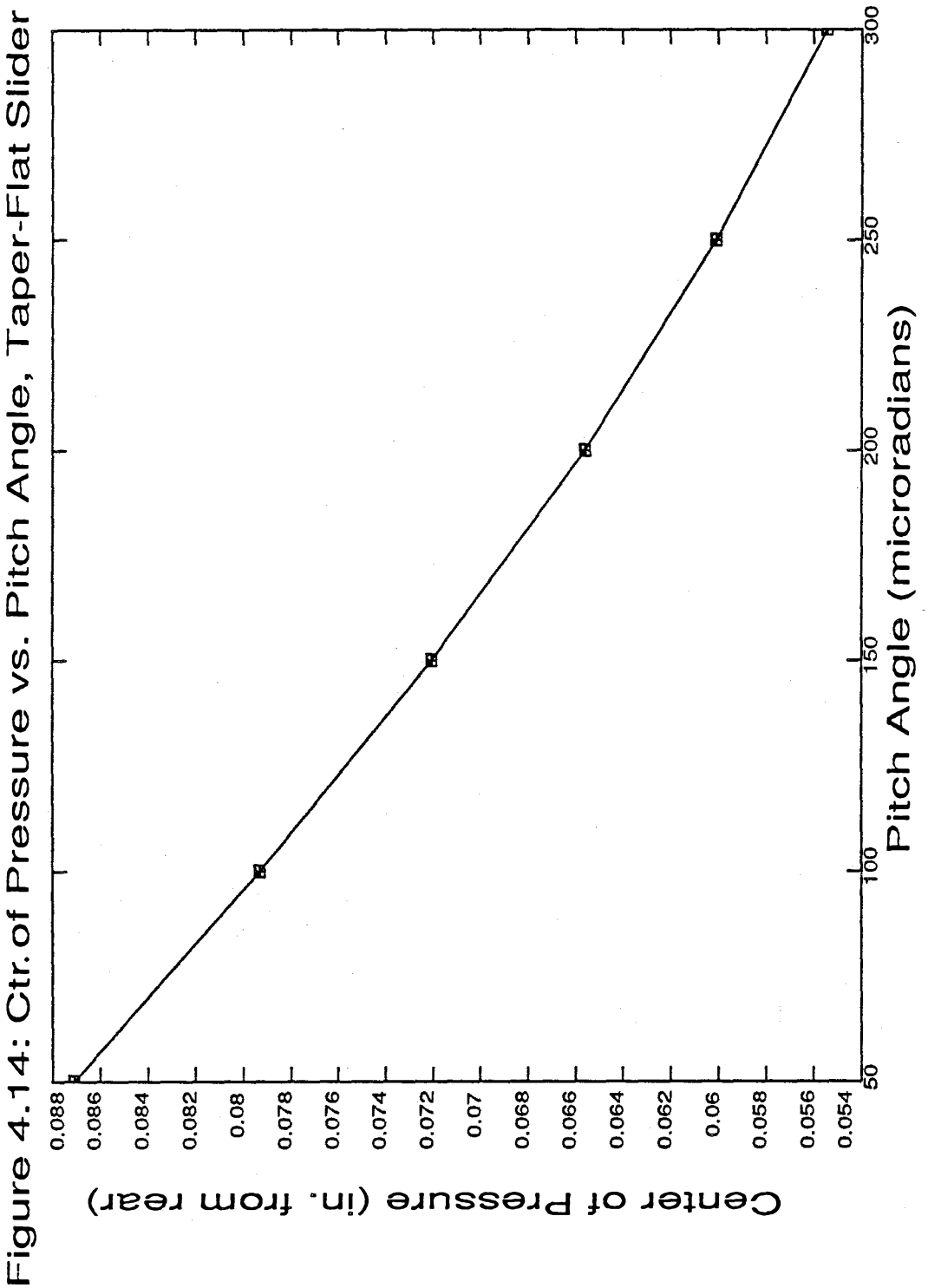

Figure 4.14: Ctr. of Pressure vs. Pitch Angle, Taper-Flat Slider

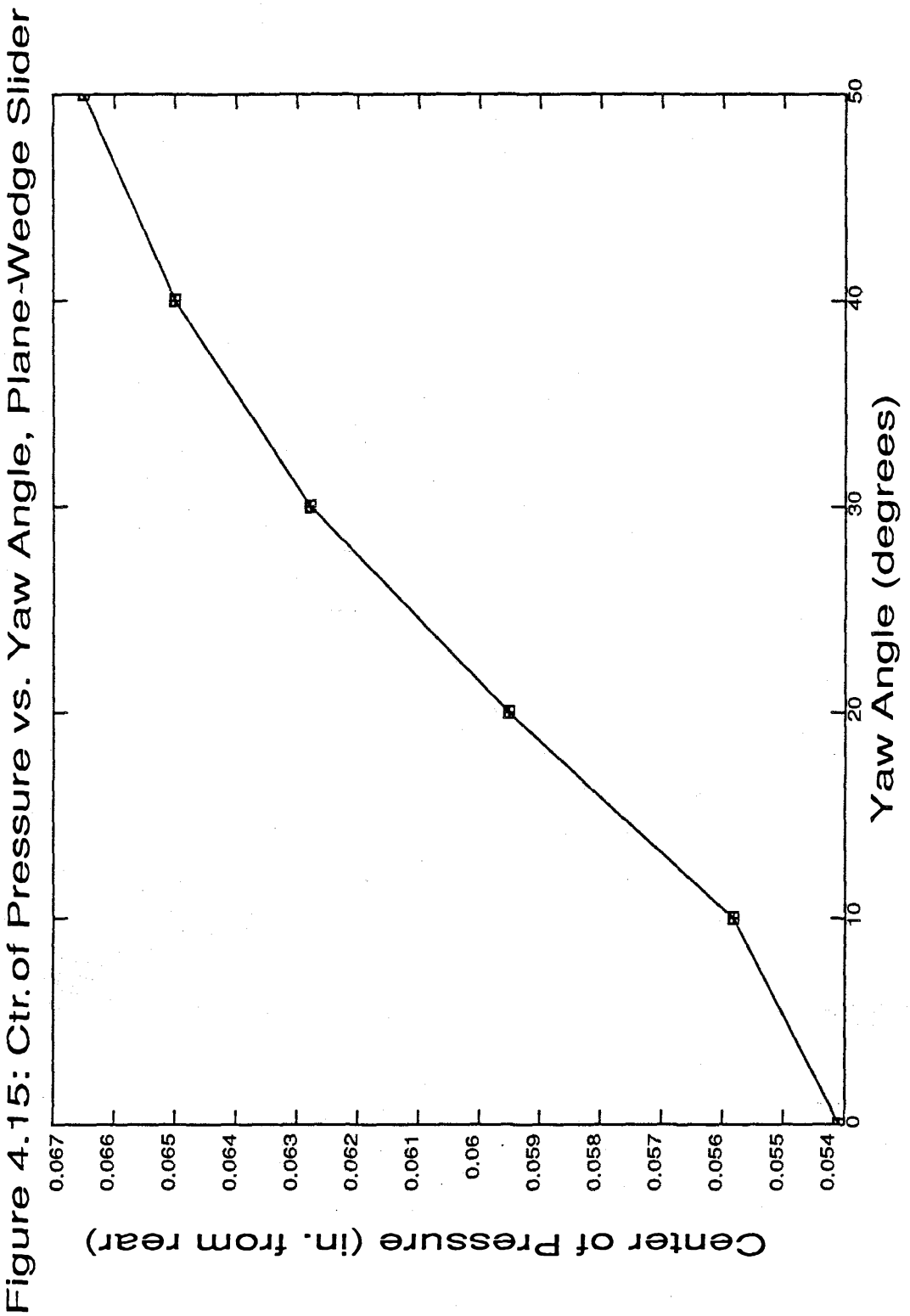

Figure 4.15: Ctr. of Pressure vs. Yaw Angle, Plane-Wedge Slider

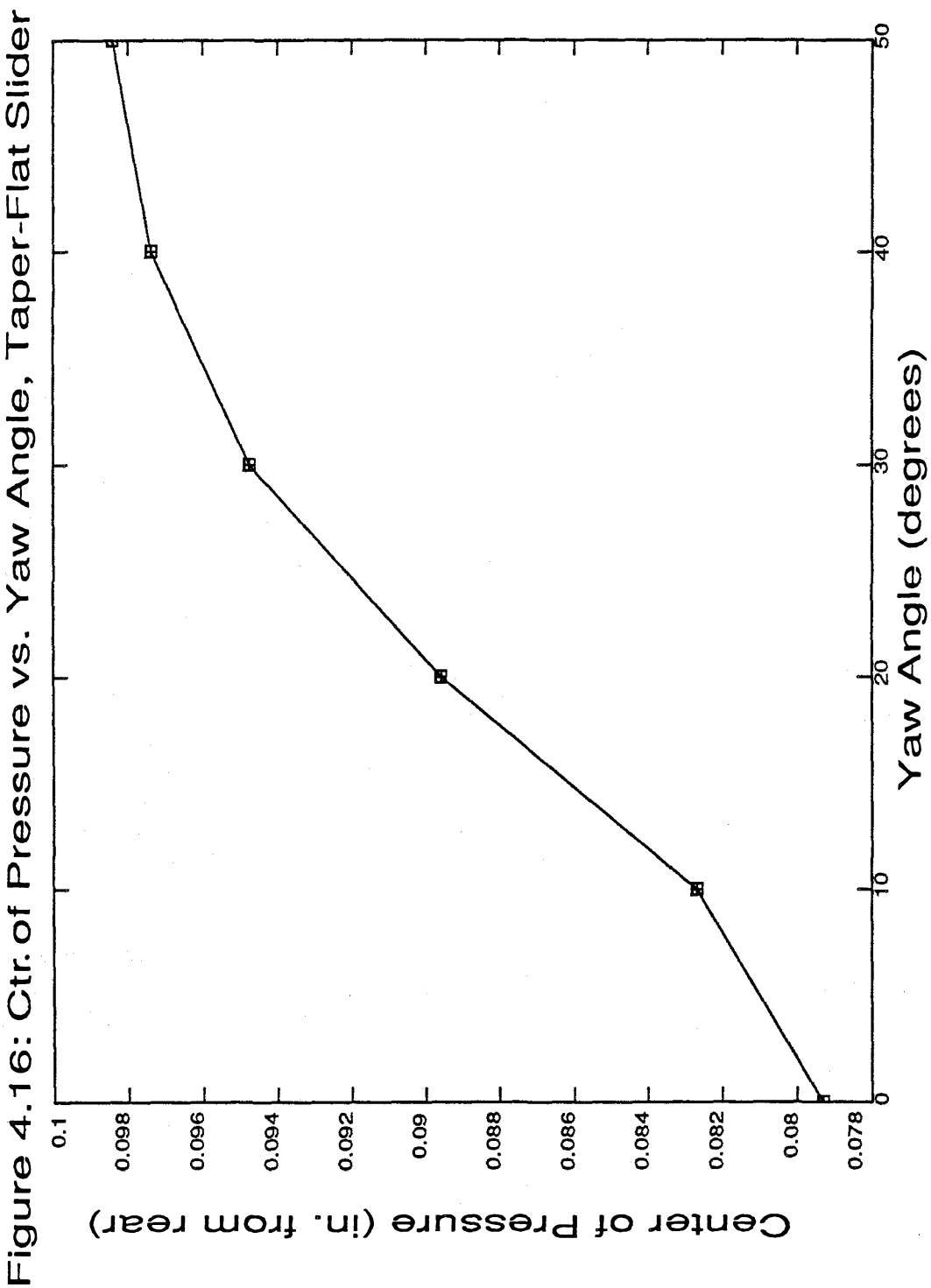

Figure 4.16: Ctr. of Pressure vs. Yaw Angle, Taper-Flat Slider

The distribution of in-phase perturbation pressure for a modal displacement of the slider body thus represents the contribution of the gas film to the stiffness matrix of the slider-bearing system, while the distribution of out-of-phase pressure indicates the contribution of the gas film to the damping matrix. The connection between slider-bearing geometry and the contribution of the gas film to stiffness and damping can be visualized by perturbing the slider body according to the eigensolutions of the slider-bearing system, and examining the resulting in-phase and out-of-phase perturbation pressure fields.

This section begins by comparing the perturbation pressure fields for the plane-wedge and taper-flat pads while oscillating in the first coupled, pitch/heave mode. The effects of pitch angle, yaw angle, and vertical spacing from the disk surface on dynamic response of plane wedge and taper-flat pads are then examined.

4.3.1 Perturbation Pressure Distribution

The perturbation pressure fields for the plane-wedge and taper-flat slider pads are shown in Figures 4.17 through 4.20. The dimensions of the slider pads in the color plots are not shown to scale. The colors in the plots correspond to the magnitude of the perturbation pressure according to the scale at the right of each figure. The numerical values of perturbation pressure are non-dimensionalized by the ambient pressure outside the bearing (see Equation 2.13). The shape of the perturbation, $\hat{h}(X,Y)$, is determined from the normalized eigenvector.

In the coupled pitch/heave mode of oscillation, there is no height perturbation along the axis of pitch rotation, and the perturbation pressure is zero. The location of the axis about which the slider body rotates in the coupled pitch/heave mode, relative to the tail of the slider body, is referred to as the center of rotation.

The in-phase pressure fields for the first coupled, pitch-heave mode of the plane-wedge and taper-flat slider-bearing pads are shown in Figures 4.17 and 4.18, respectively. The natural frequencies corresponding to Figures 4.17 and 4.18 are 21.5 KHz for the plane wedge, and 24.4 KHz for the taper-flat pad.

From a comparison of Figures 4.17 and 4.18, the effect of the inlet-taper on the center of rotation in the first coupled, pitch-heave mode is evident. For the plane wedge, Figure 4.17, the center of rotation is in the rear half of the slider pad, while for the taper-flat shown

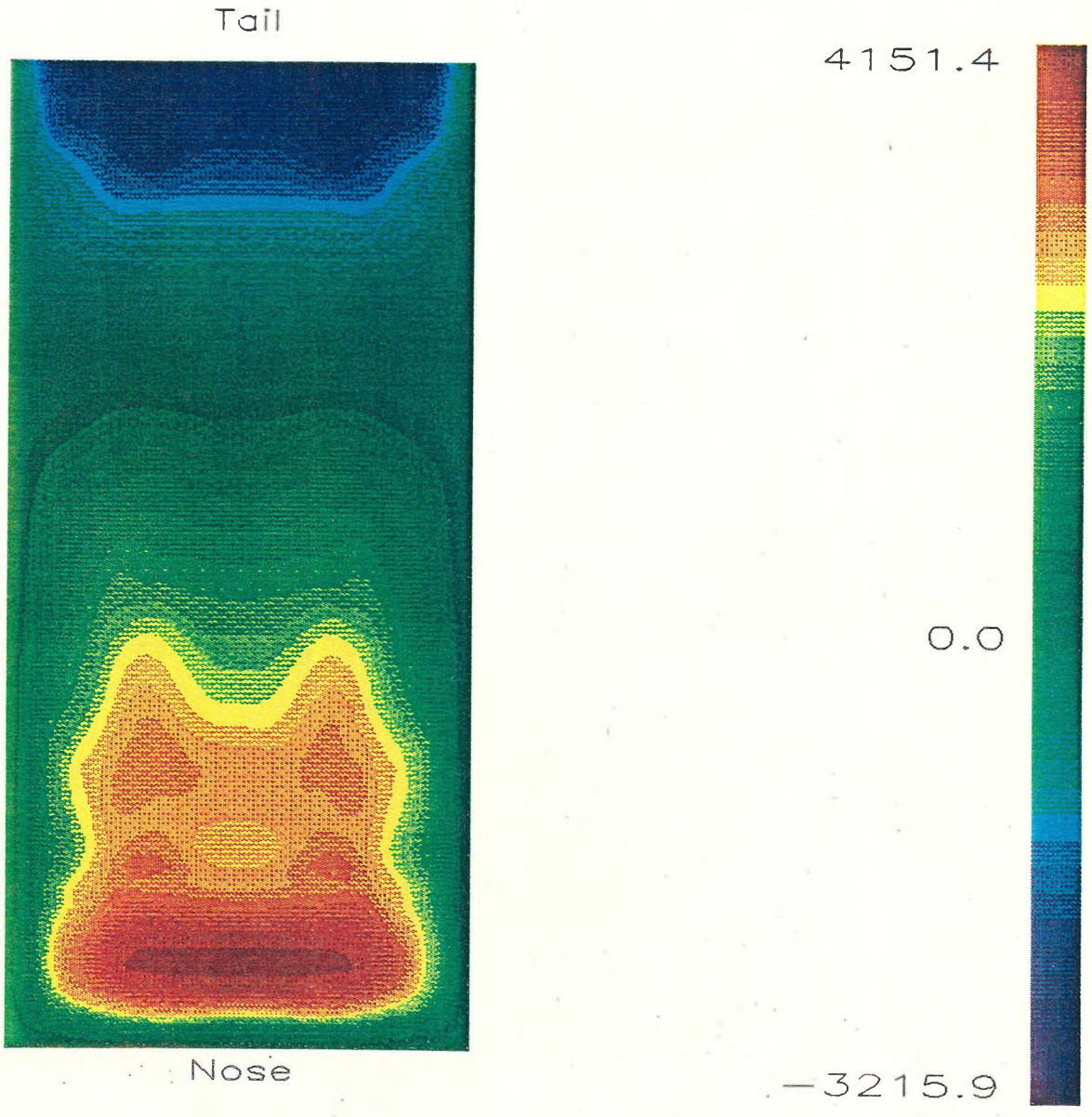

Figure 4.17: Plane Wedge, P−H Mode 1, P1

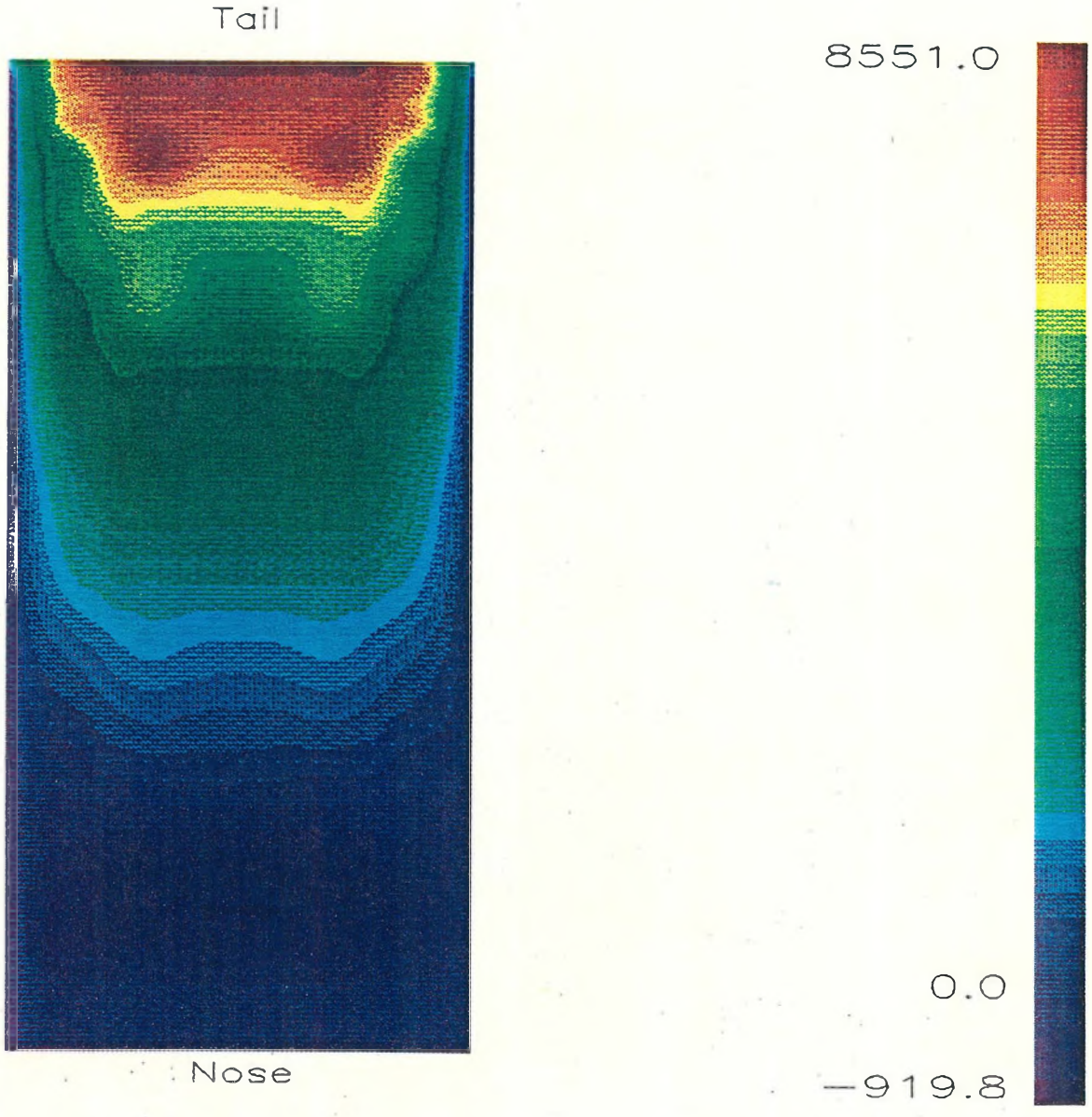

Figure 4.18: Taper Flat, P−H Mode 1, P1

in Figure 4.18, it is in the front half of the pad. For this mode, the additional pressure peak near the nose of the taper-flat pad shifts the center of rotation away from the tail of the slider body.

The in-phase pressure in the taper-flat pad is greatest near the tail, where the spacing between the disk and slider pad is the smallest. This area is also farthest from the center of rotation, and thus experiences a larger vertical perturbation. For the plane-wedge pad, the center of rotation is near the tail, and the percentage change in vertical spacing is nearly the same at either end of the slider pad. The plane-wedge pad thus exhibits peaks in in-phase perturbation pressure at both the nose and the tail.

Figures 4.19 and 4.20 show the out-of-phase perturbation pressure fields for the same coupled, pitch-heave mode as in Figures 4.17 and 4.18. The fraction of critical damping for the plane-wedge pad in this mode (Figure 4.19) is .018, while for the taper-flat it is .06. The taper-flat slider profile shows very little out-of-phase perturbation pressure around the inlet taper but has its peak value near the tail, where the transverse gradient of static pressure is high, and the vertical motion is greatest. For the plane-wedge slider pad, Figure 4.19, the maximum out-of-phase perturbation pressure is near the nose, where the longitudinal gradient of static pressure is the smallest, and the vertical motion is greatest. The plane wedge also exhibits peak values of perturbation pressure near the region of large transverse gradient in static pressure at the tail. This peak is of lower magnitude than that of the taper- flat because of the reduced vertical displacement of the plane wedge at the tail.

For the pitch-heave mode discussed above, the plane-wedge slider pad exhibits lower damping and natural frequency than the taper-flat pad. The center of rotation of the plane-wedge pad is nearer the tail, where the magnetic transducer is most easily placed. While the addition of the inlet taper improves damping and natural frequency, it also shifts the center of rotation farther from the transducer location, resulting in greater variation in spacing between the transducer and the disk surface.

The responses of the plane wedge and the taper-flat slider pad geometries to variations in pitch angle, yaw angle, and tail spacing are compared in the following section. The slider-bearing system was in equilibrium at each operating condition for the dynamic perturbation calculations. The solution of the eigenproblem defined by Equation 3.10 provides the natural frequency, fraction of critical damping, and mode shape that characterize the

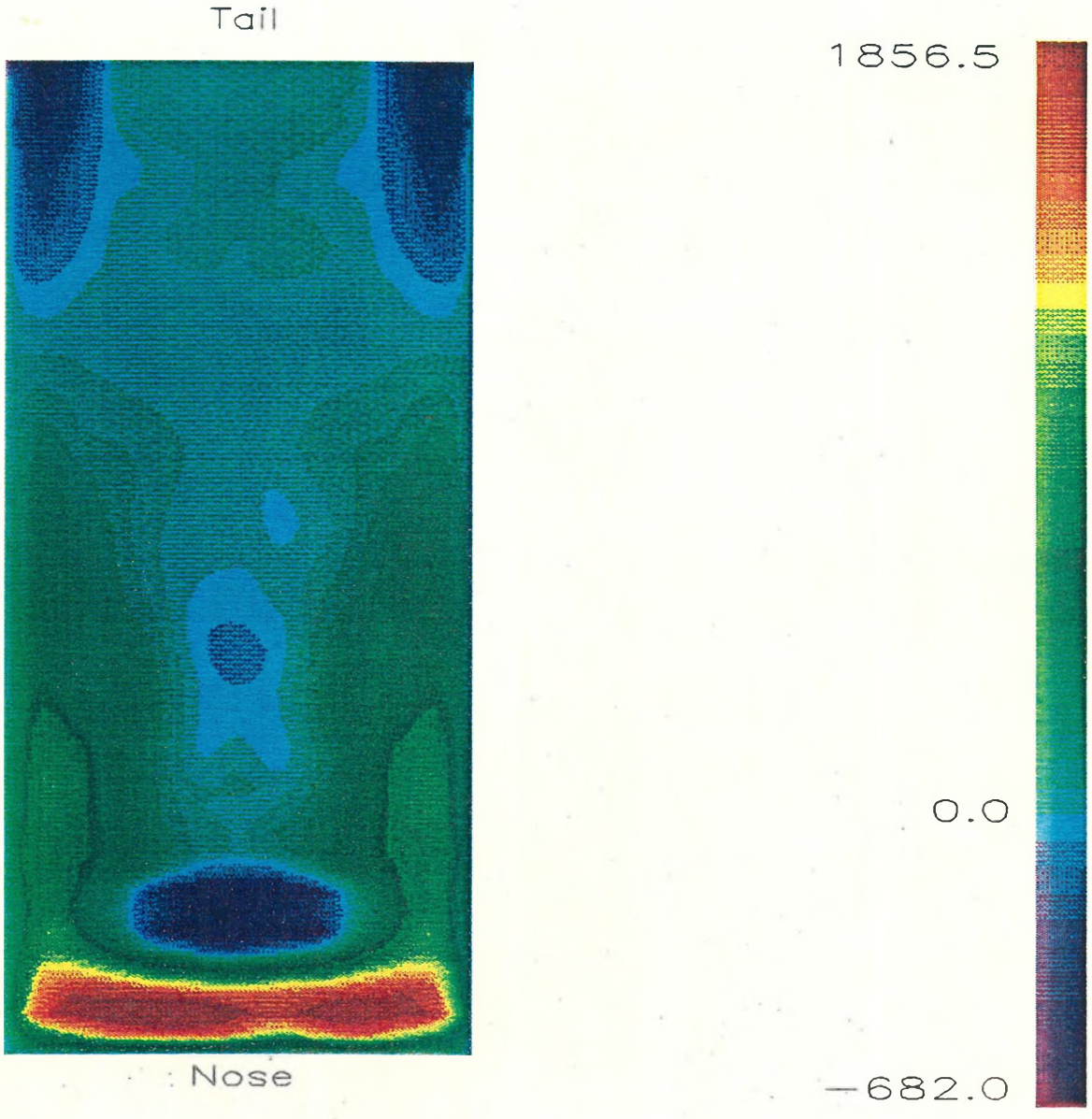

Figure 4.19: Plane Wedge, P−H Mode 1, P2

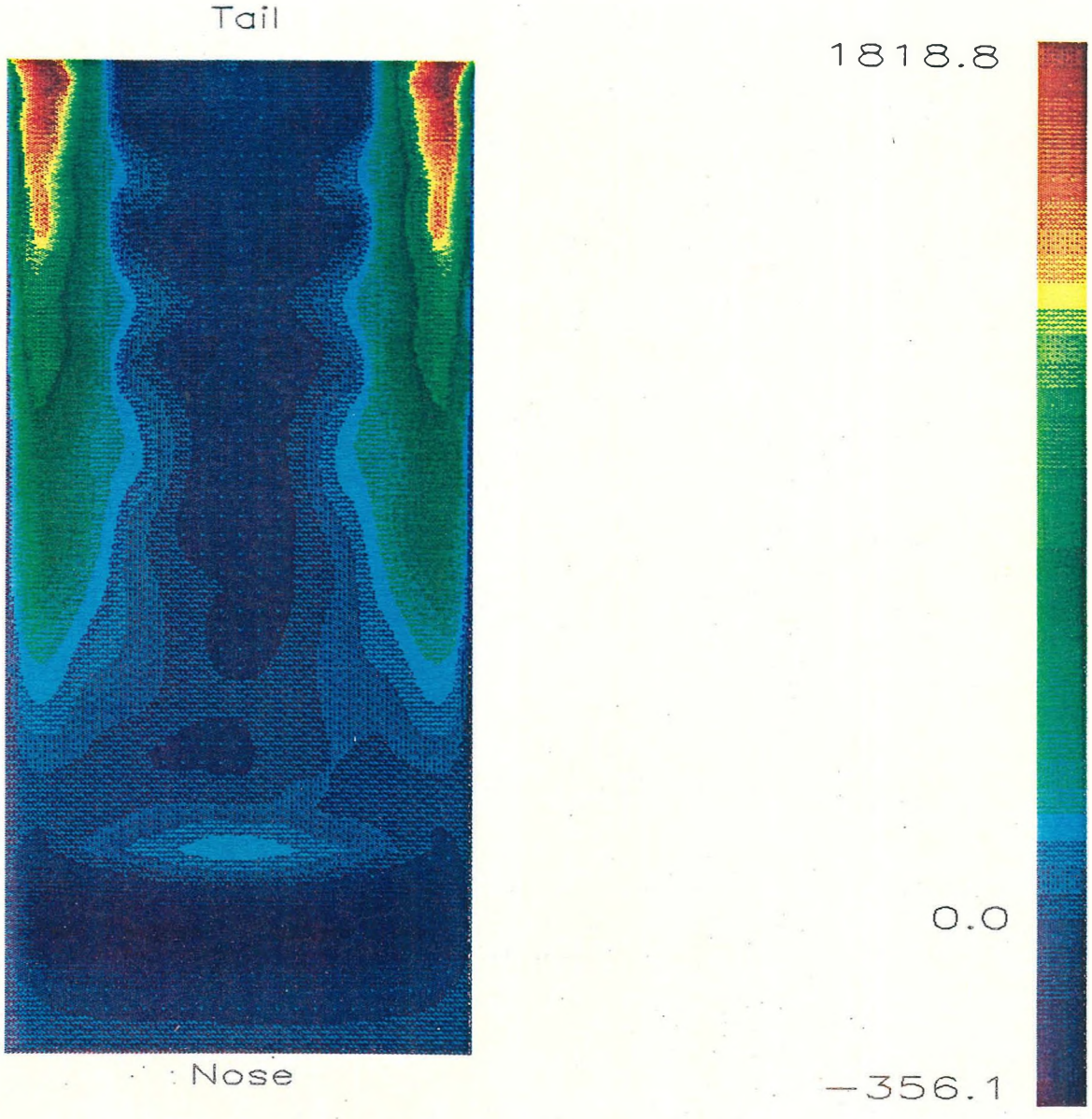

Figure 4.20: Taper Flat, P−H Mode 1, P2

dynamic performance of the slider bearing for each equilibrium condition.

4.3.2 Natural Frequency

According to a modal analysis of the slider-bearing system, there are two coupled pitch-heave modes, and an uncoupled roll mode of slider oscillation for each pad geometry. The natural frequencies of these three modes, as a function of tail spacing, are compared for the plane-wedge and taper-flat slider pads in Figures 4.21. and 4.22. For the range of 10 microinch to 30 microinch tail spacing, the uncoupled roll mode and the second coupled, pitch-heave mode are very similar for the plane-wedge and taper-flat pads. In the first coupled, pitch-heave mode, the taper-flat slider pad exhibits consistently higher frequency over the range of tail spacings studied.

Pitch angle also has a significant effect on natural frequency, as illustrated by Figures 4.23 and 4.24. The sensitivity to pitch angle is similar for the plane-wedge and taper-flat slider bearing pads in the uncoupled roll mode, but the second coupled, pitch-heave mode shows a much greater reduction in frequency with higher pitch in the taper-flat pad geometry.

Natural frequency is also affected by the yaw angle, as shown in Figures 4.25 and 4.26. The uncoupled roll modes of each of the two slider-bearing geometries show very similar behavior over the yaw-angle range of 0 to 50 degrees. For the plane-wedge slider pad, Figure 4.25, the coupled, pitch-heave modes become closer in natural frequency with increasing yaw. Figure 4.26, for the taper-flat pad, shows the two coupled, pitch-heave modes to grow farther apart in natural frequency as the yaw angle becomes greater.

4.3.3 Fraction of Critical Damping

The modal analysis methods described in Chapter 3 provide a value for the fraction of critical damping of each of the natural modes. This damping fraction is an important measure of the slider-bearing system's stability.

The effect of tail spacing on the fraction of critical damping is illustrated by Figures 4.27 and 4.28 for the plane wedge and taper-flat, slider-bearing geometries, respectively. The uncoupled roll mode shows an increase in the fraction of critical damping with increasing tail spacing for both pad geometries, with the taper-flat pad having a slightly lower value over the entire range. The first coupled, pitch-heave mode of the plane-wedge

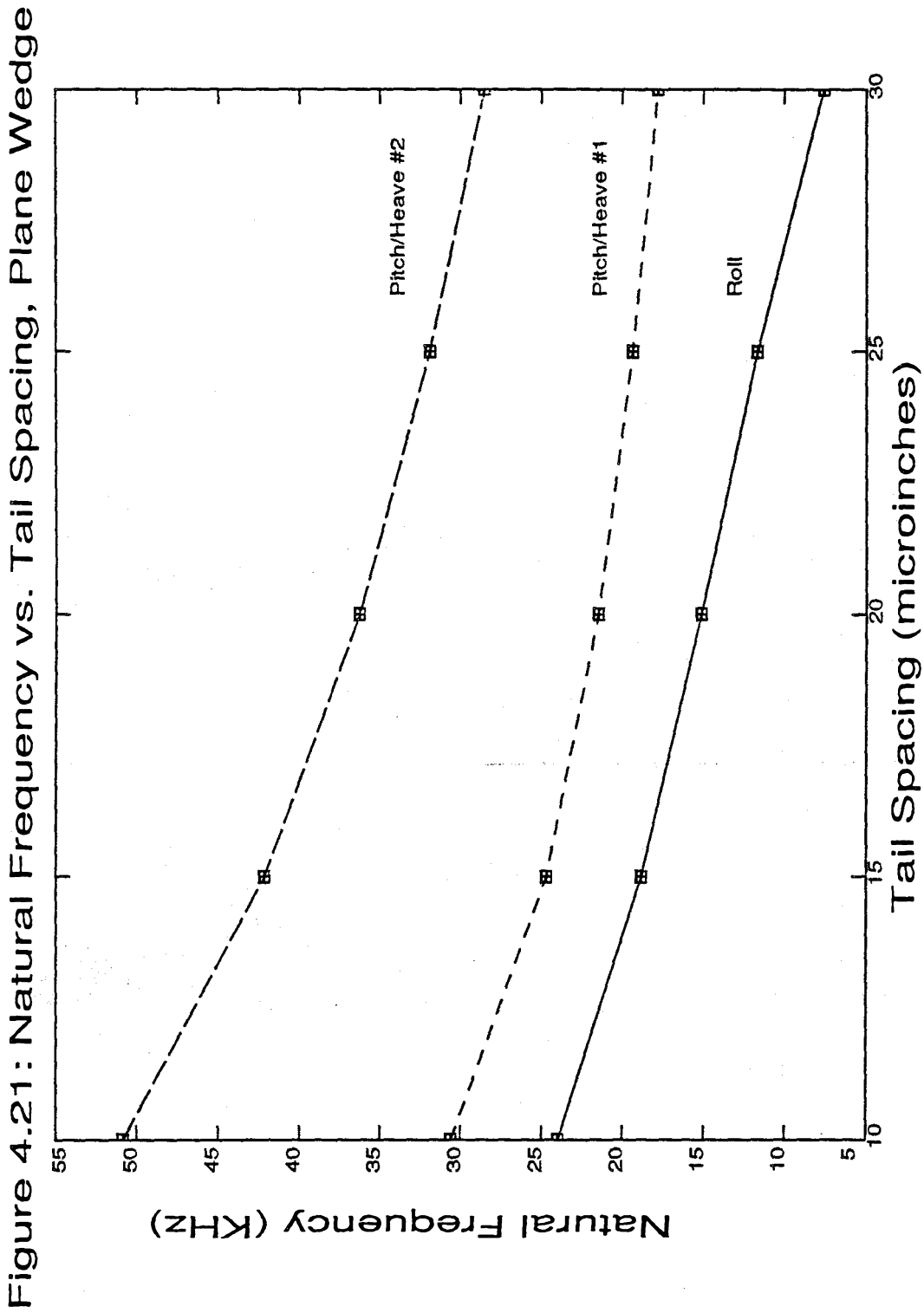

Figure 4.21: Natural Frequency vs. Tail Spacing, Plane Wedge

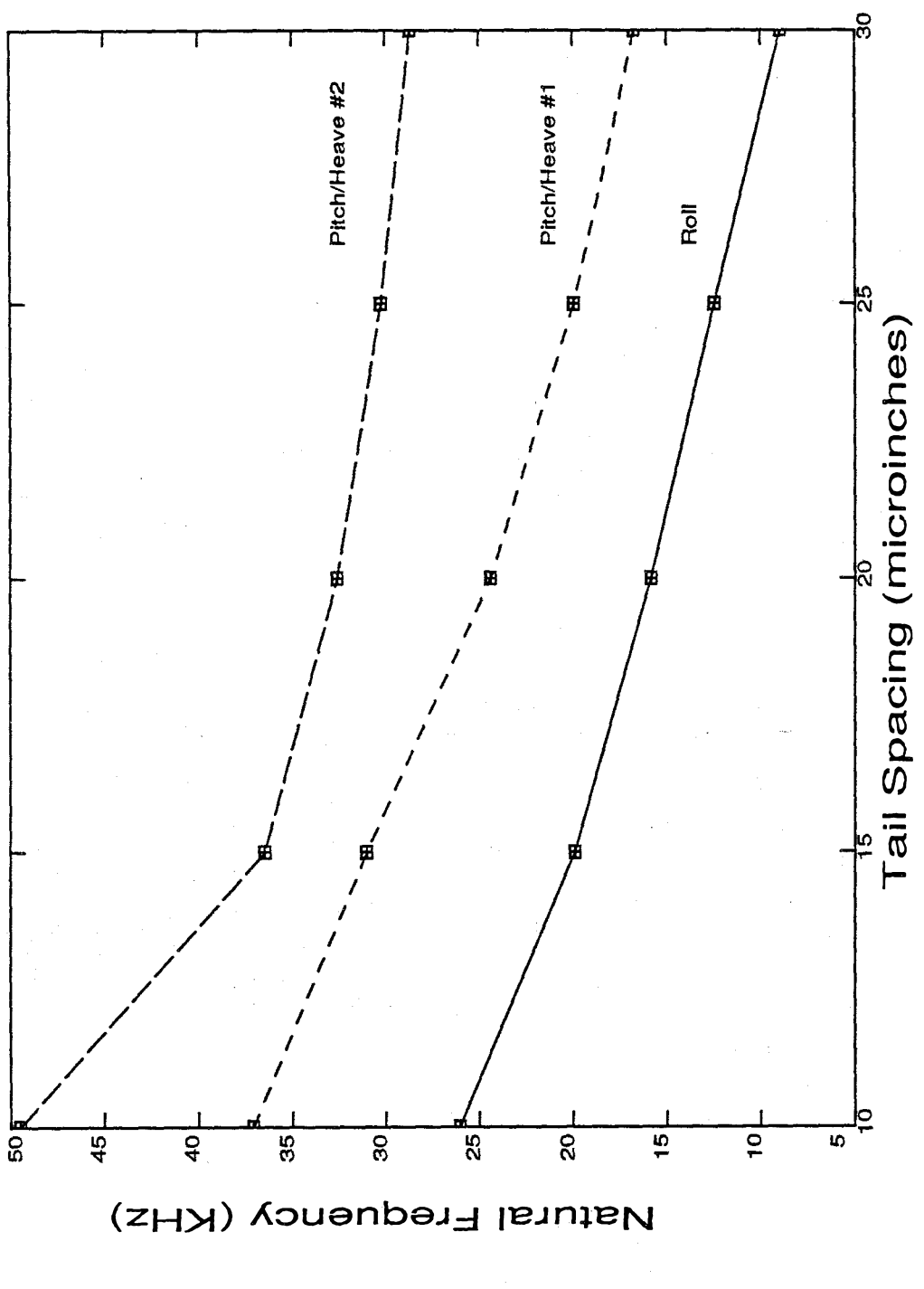

Figure 4.22: Natural Frequency vs. Tail Spacing, Taper-Flat

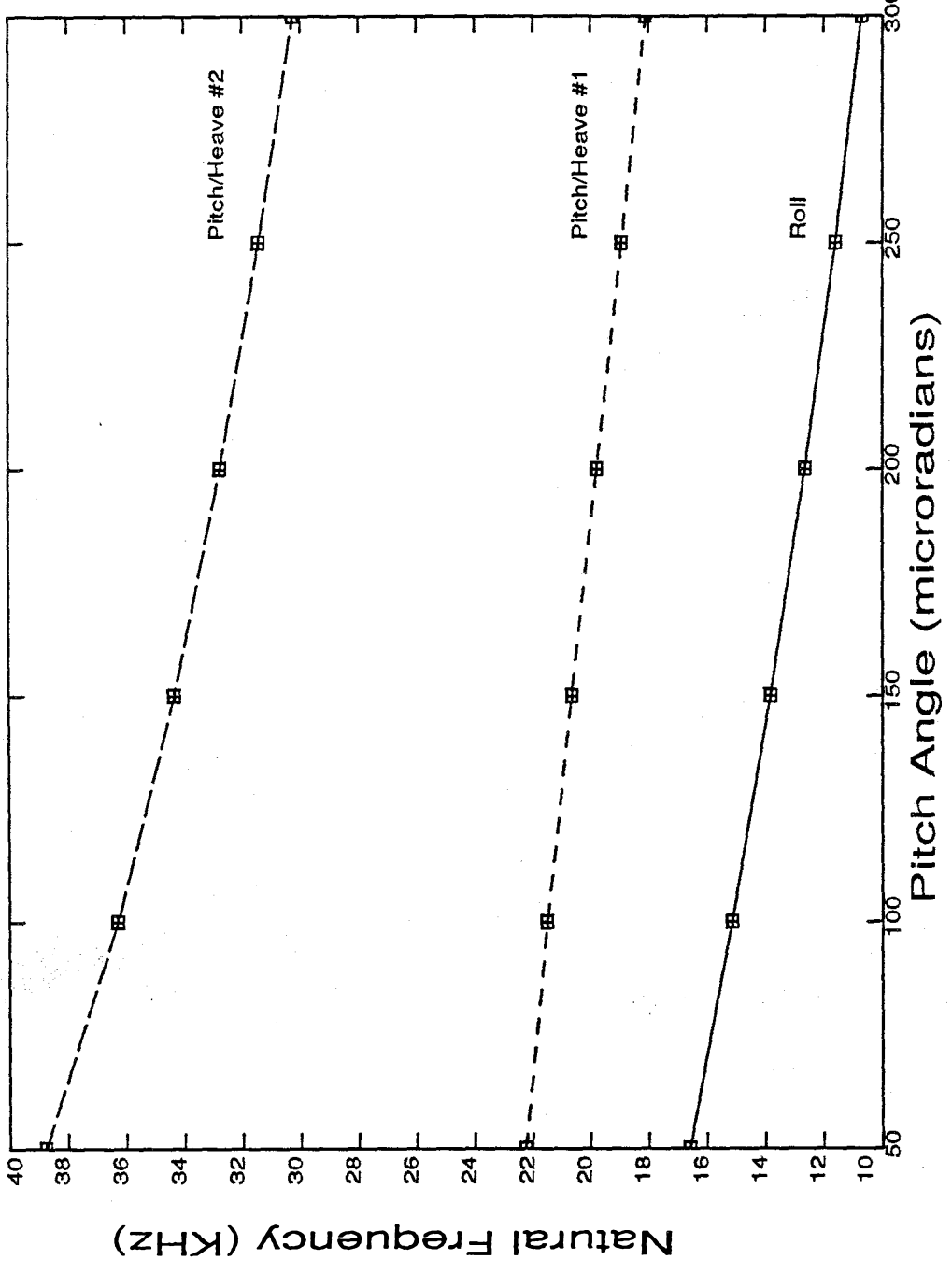

Figure 4.23: Natural Frequency vs. Pitch Angle, Plane Wedge

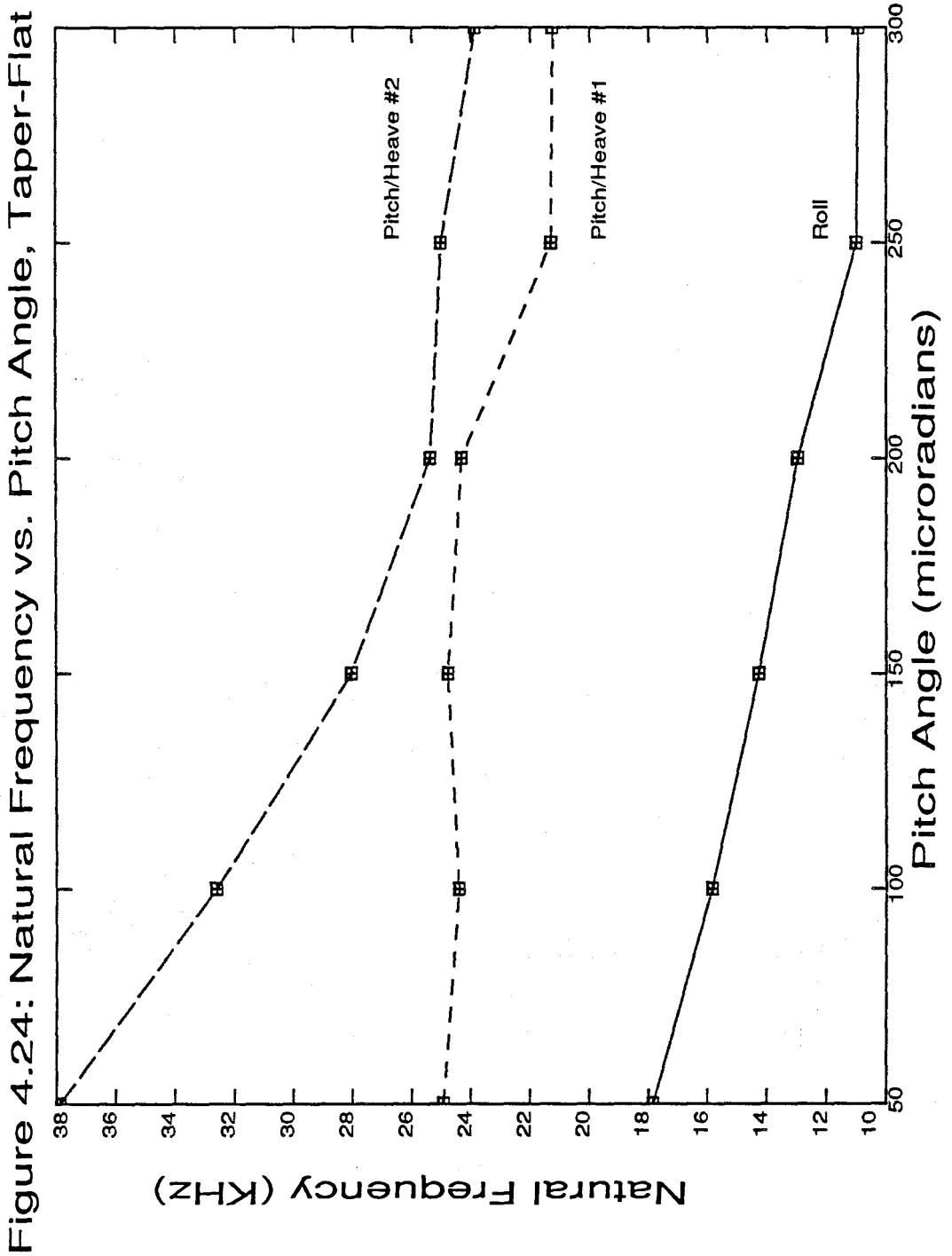

Figure 4.24: Natural Frequency vs. Pitch Angle, Taper-Flat

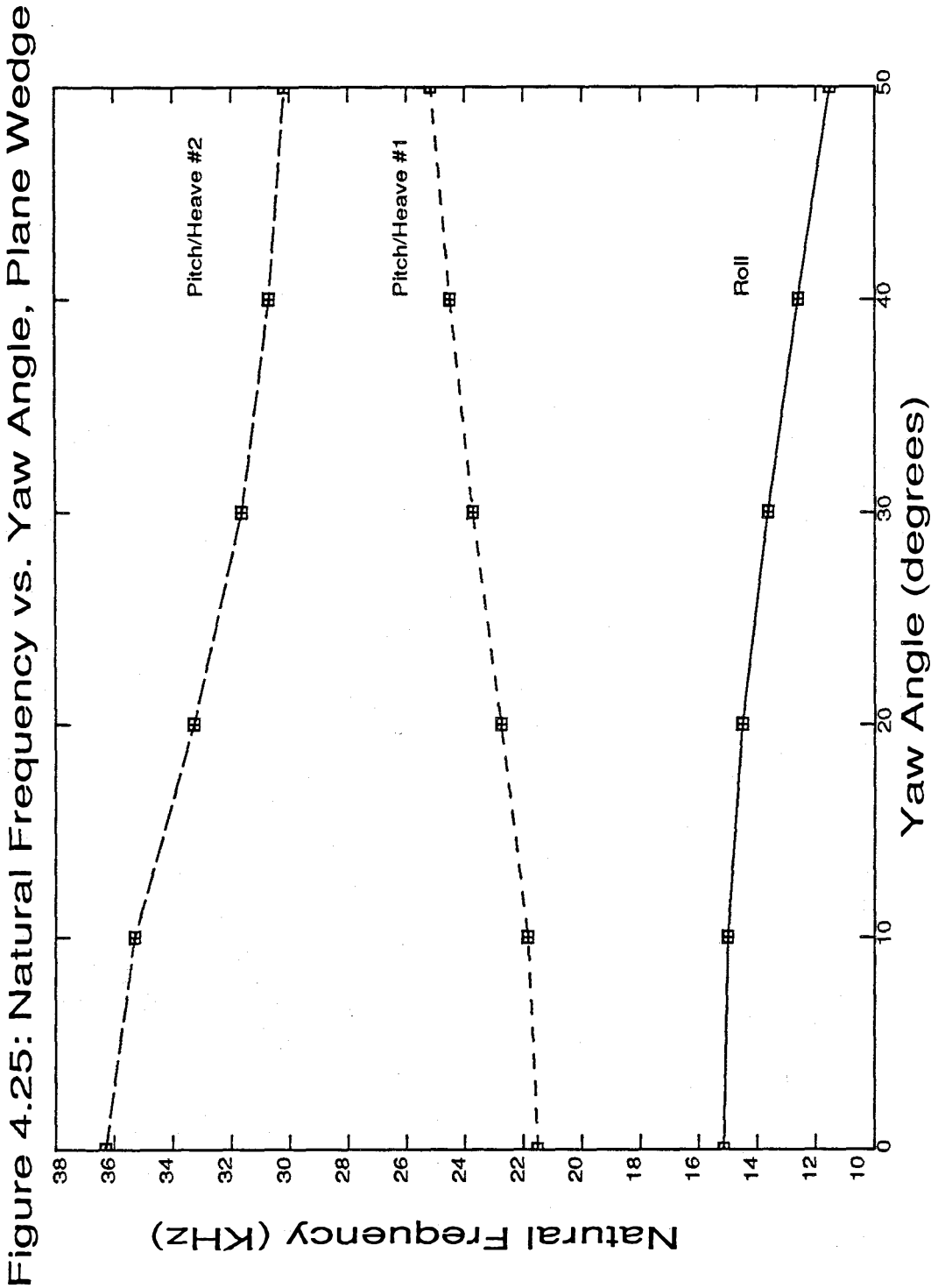

Figure 4.25: Natural Frequency vs. Yaw Angle, Plane Wedge

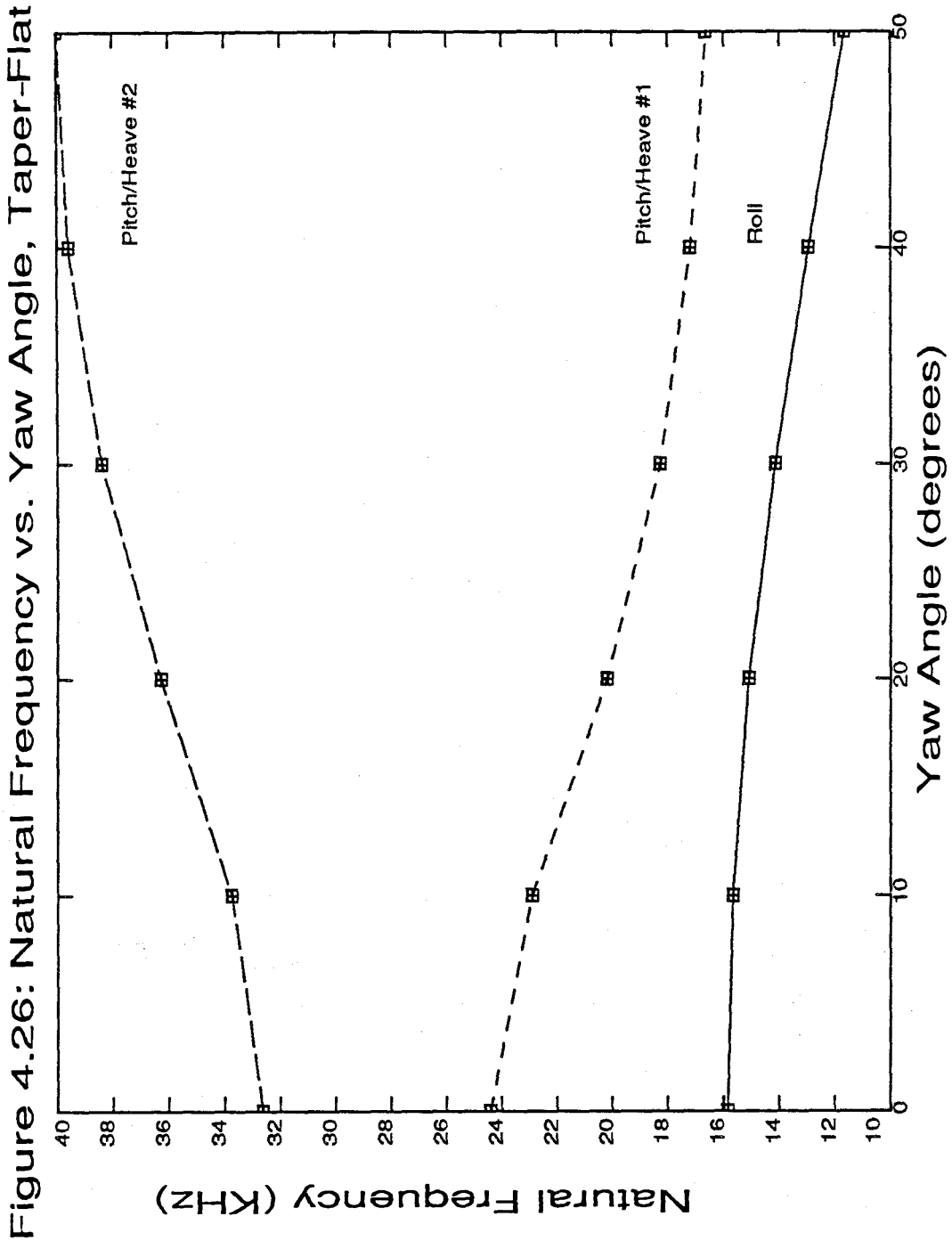

Figure 4.26: Natural Frequency vs. Yaw Angle, Taper-Flat

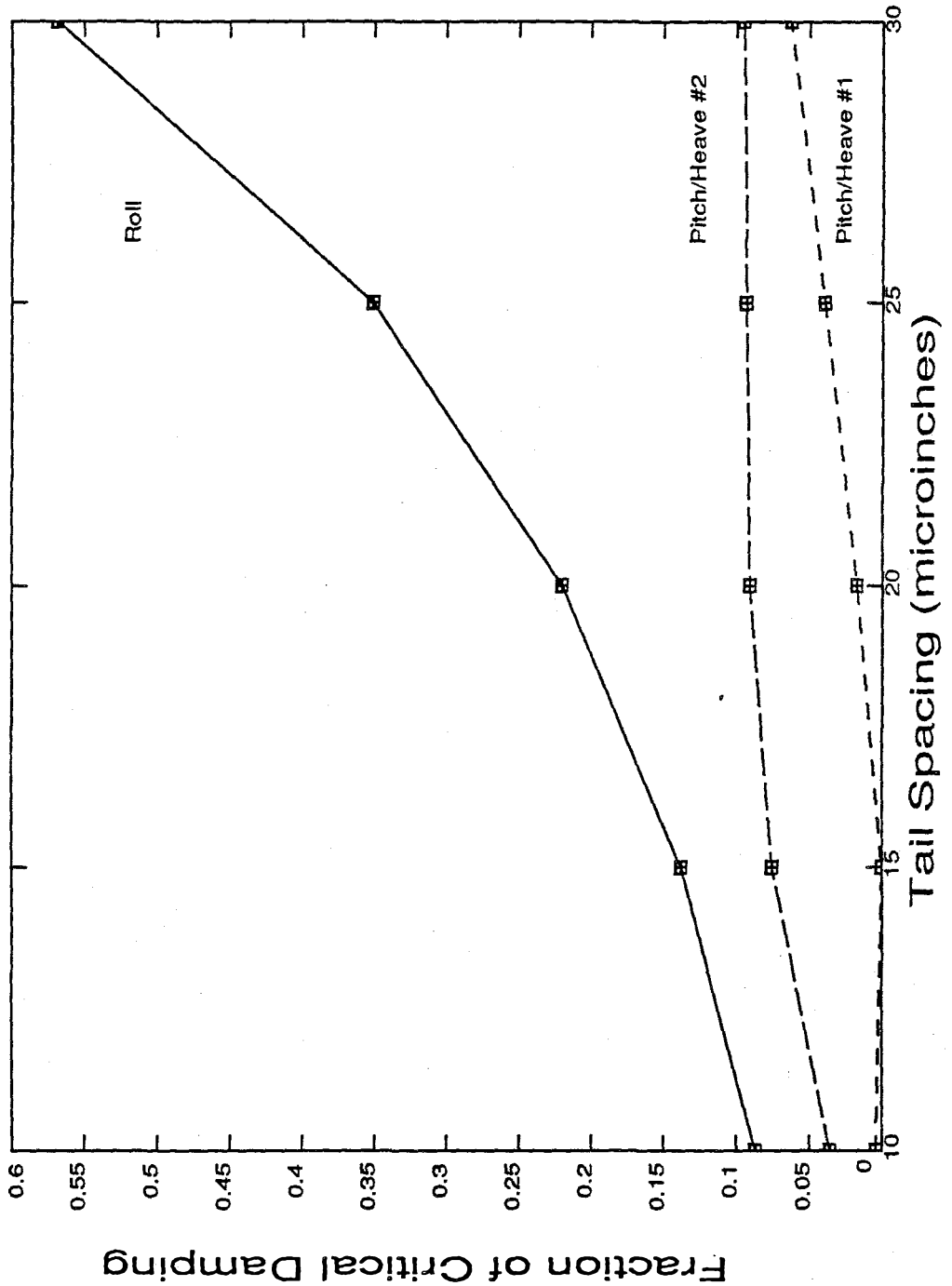

Figure 4.27: Fraction of Critical Damping vs. Tail Spacing, Plane Wedge

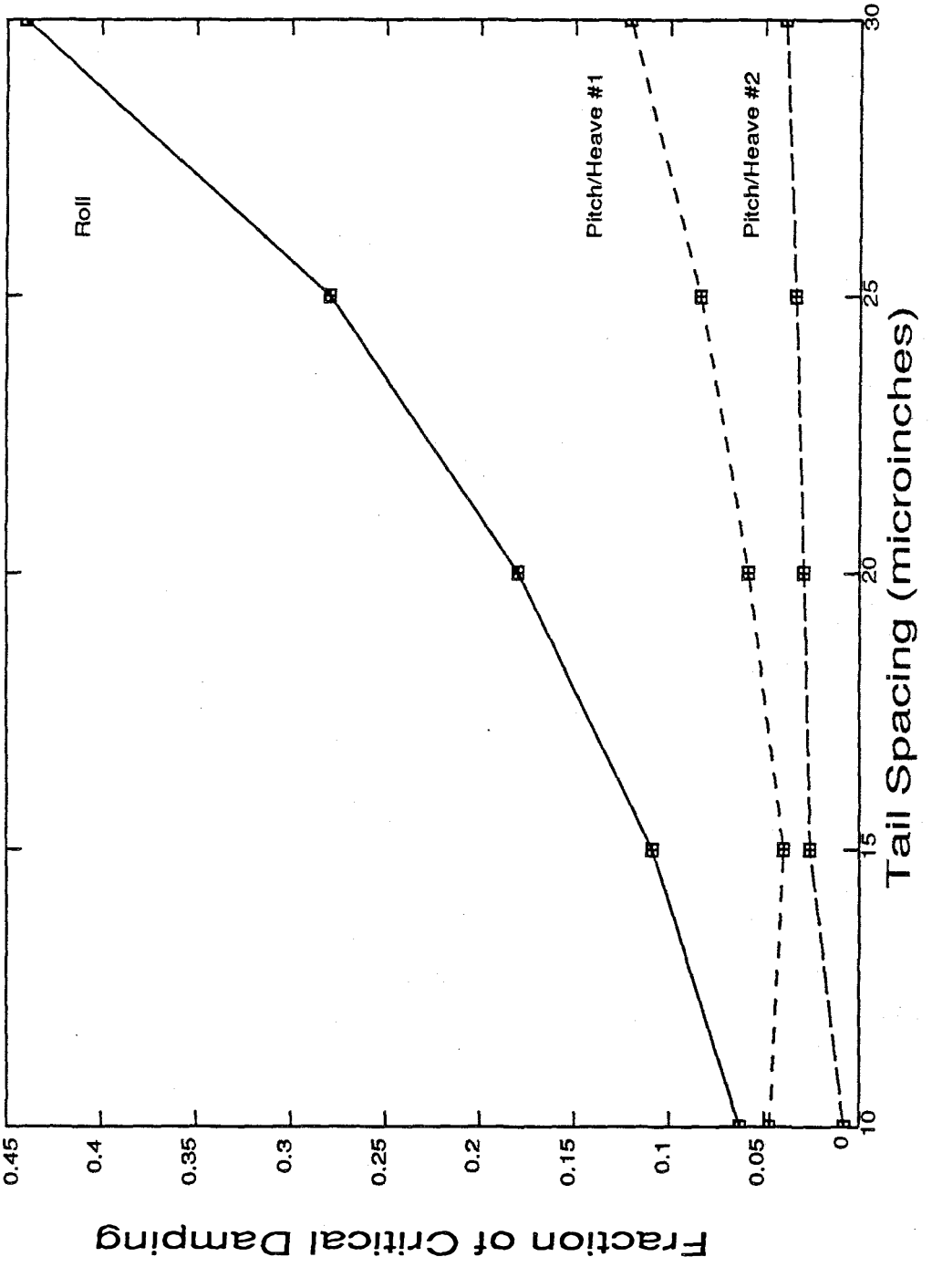

Figure 4.28: Fraction of Critical Damping vs. Tail Spacing, Taper-Flat

slider pad has a very low damping value at a tail spacing of 10 microinches, and shows only marginal improvement when the tail spacing is increased to 30 microinches. The same mode for the taper-flat slider pad also shows slight improvement in damping with increasing tail spacing and has higher overall values than the plane wedge. In the second coupled, pitch-heave mode, both the plane-wedge and taper-flat pads exhibit a value of fraction of critical damping that increases and then levels off, as the tail spacing becomes greater. The overall damping values for the plane wedge are approximately double those of the taper-flat pad for this mode.

The fraction of critical damping for the two coupled pitch-heave modes of the plane-wedge slider is relatively insensitive to pitch angles ranging from 50 to 300 microradians, as seen in Figure 4.29. Figure 4.30 shows the fraction of critical damping as a function of pitch angle for the taper-flat slider pad. The second pitch-heave mode of the taper-flat shows an increase in fraction of critical damping with pitch angle, while the first pitch-heave mode loses damping as pitch angle becomes larger. Experimental observations of taper-flat sliders using optical interferometry indicate incipient pitch instability at pitch angles greater than 300 microradians. This loss of pitch stability at large pitch angles can be deduced from the present analysis.

Yaw angle has also been found, through experimental observations, to cause instability at values greater than approximately 30 degrees. The computed effect of yaw angle on the fraction of critical damping, for the plane wedge and taper-flat slider bearing pads, is illustrated by Figures 4.31 and 4.32. Both pitch-heave modes show a decrease in fraction of critical damping with yaw angle for the plane-wedge slider pad, while, for the taper-flat, the second pitch-heave mode shows a minimum in the damping curve at a yaw angle of approximately 30 degrees. The fraction of critical damping obtained from the present analysis thus serves to predict the loss of slider-bearing stability with increasing yaw angle.

4.3.4 Center of Rotation

The main function of the slider bearing in a magnetic recording system is to maintain a constant spacing between the magnetic read-write transducer and the disk surface. Because of manufacturing constraints, this magnetic transducer is usually placed at the tail of the slider body. The eigenvectors obtained from the modal analysis technique developed here can be used to compute the center of rotation for the two coupled, pitch-heave modes. In

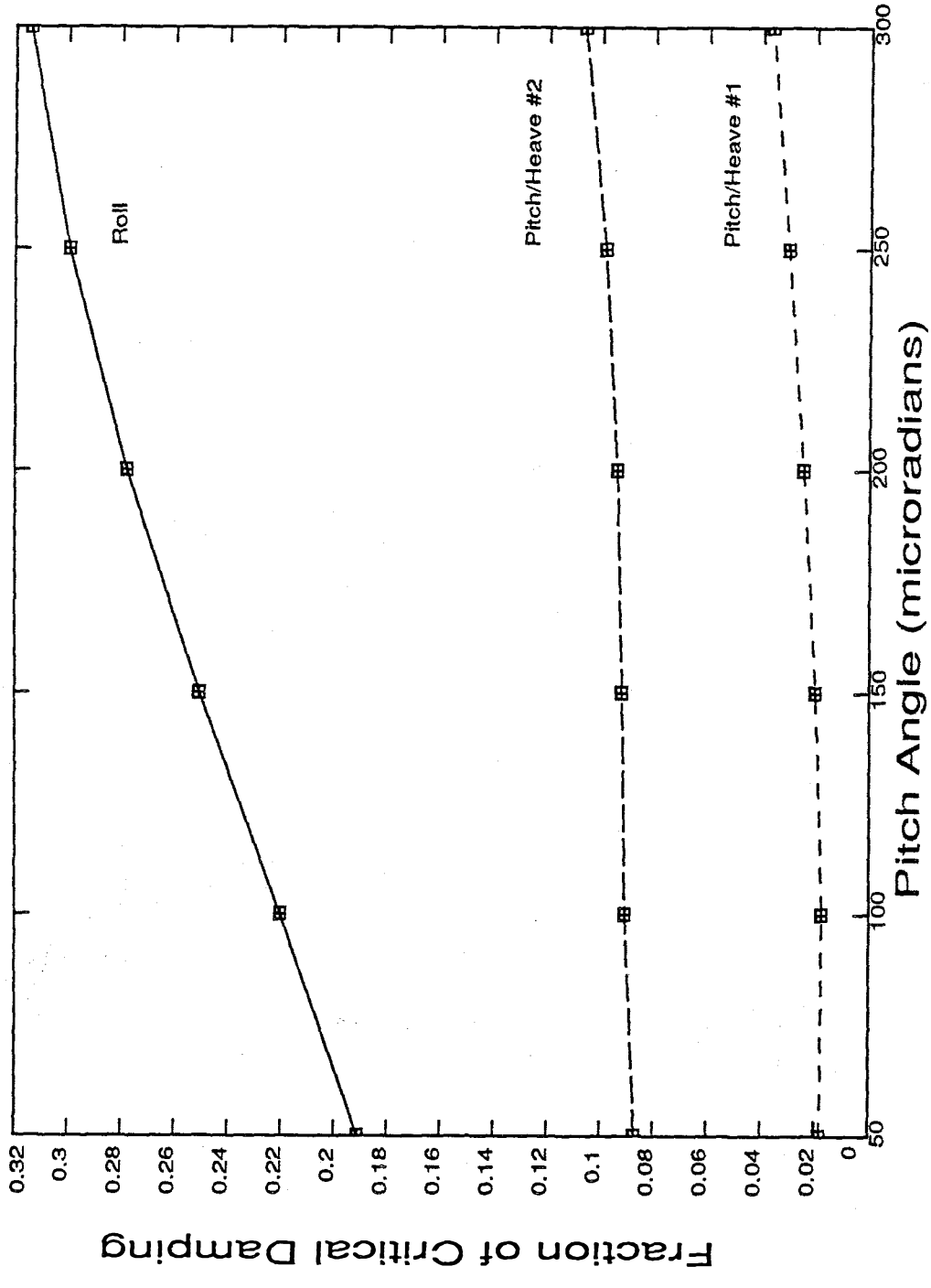

Figure 4.29: Fraction of Critical Damping vs. Pitch Angle, Plane Wedge

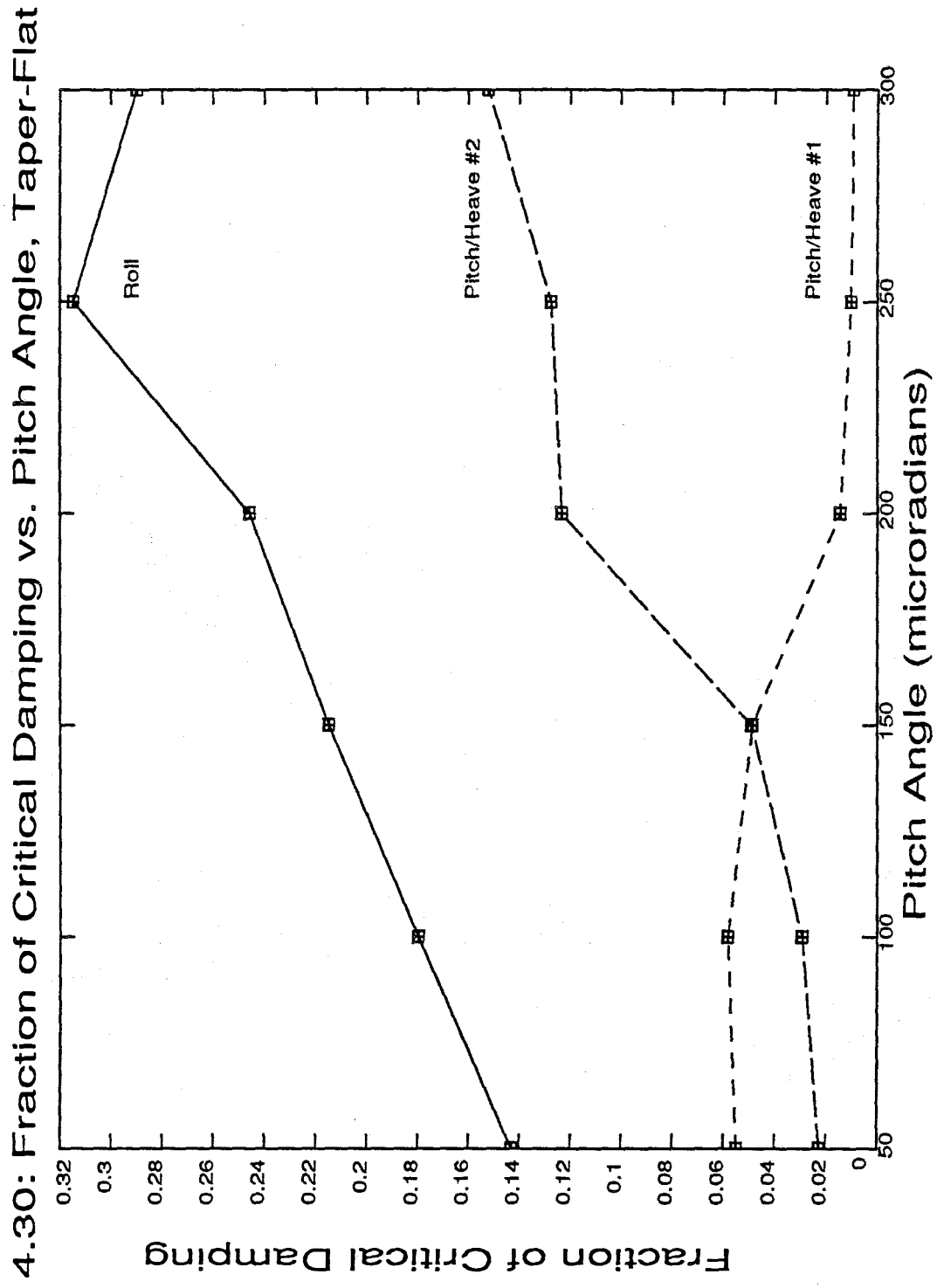

Figure 4.30: Fraction of Critical Damping vs. Pitch Angle, Taper-Flat

Figure 4.31: Fraction of Critical Damping vs. Yaw Angle, Plane Wedge

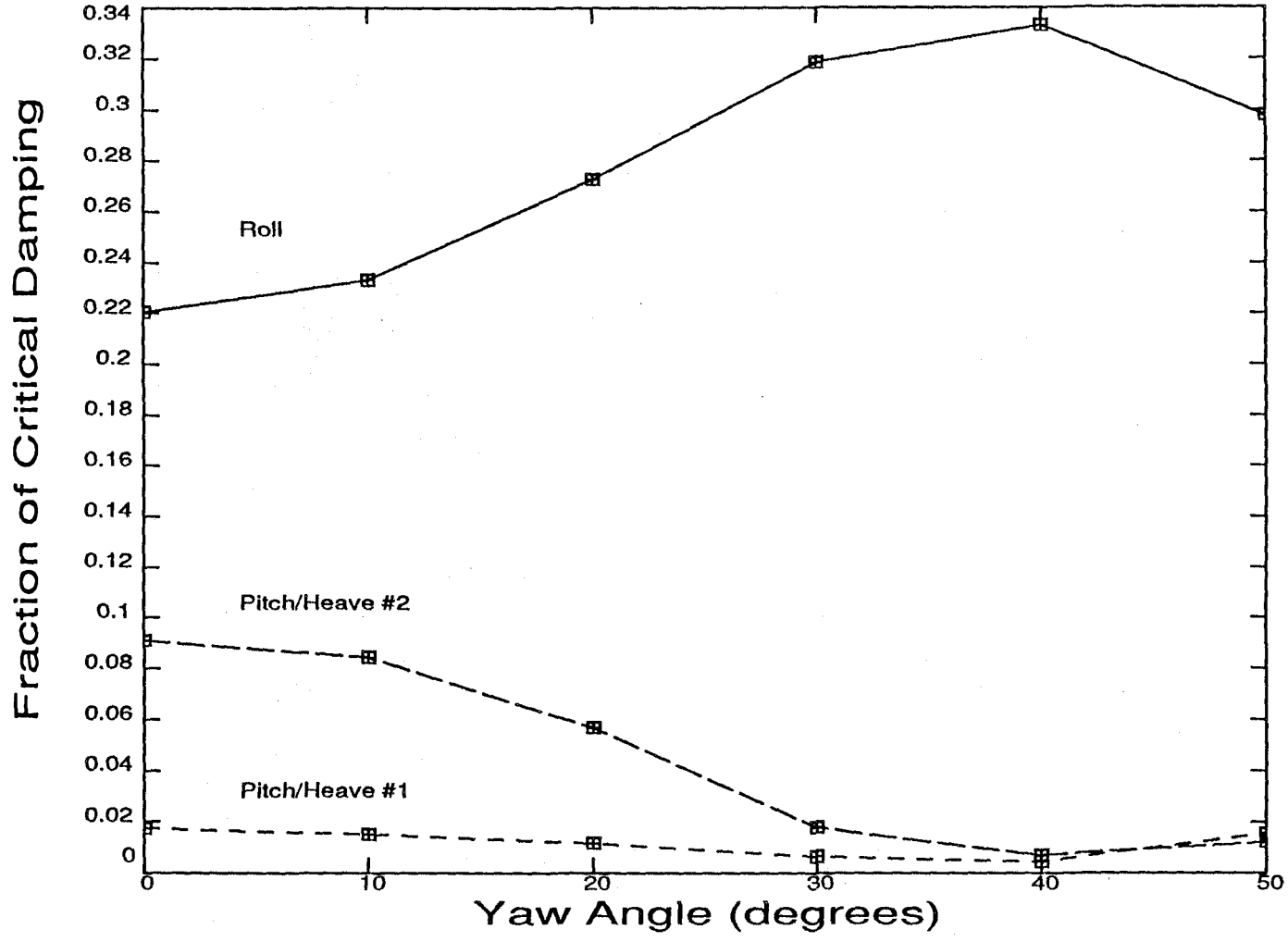

Figure 4.32: Fraction of Critical Damping vs. Yaw Angle, Taper-Flat

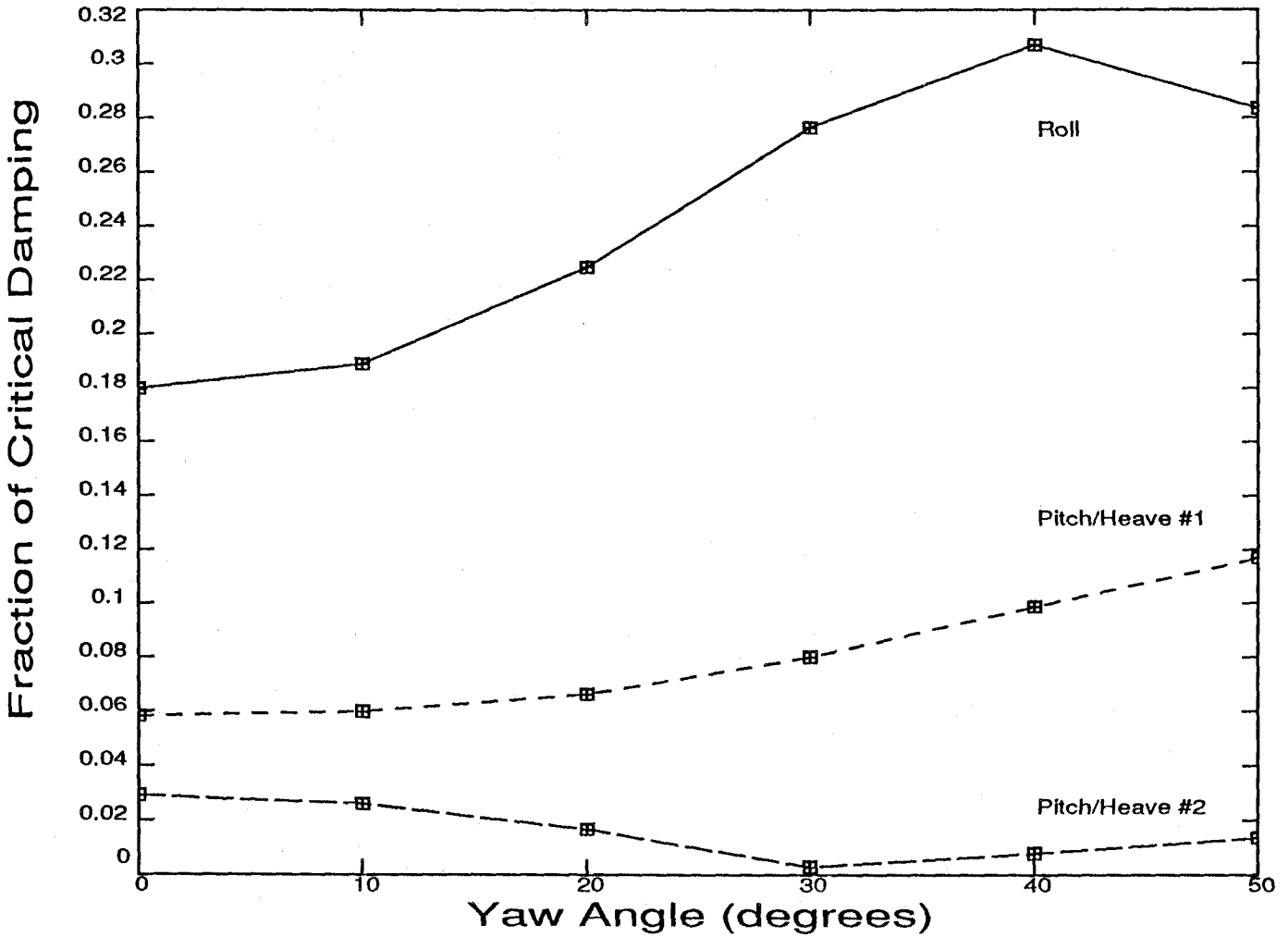

the figures that follow, center of rotation is measured from the tail of the slider pad such that negative values are behind the slider, and positive values are nearer the nose. From a design standpoint, it is desirable to minimize the distance between this center of rotation and the location of the magnetic transducer (usually at the tail). In the ideal situation, both coupled, pitch-heave modes would have a center of rotation of zero for the specific slider geometries considered here.

The effect of tail spacing on the center of rotation for the plane-wedge and taper-flat slider-bearing pads is shown in Figures 4.33 and 4.34. Neither of the coupled pitch-heave modes of the plane-wedge pad shows much change with tail spacing over the range of 10 to 30 microinches. For the taper-flat pad, Figure 4.34, the rotational centers of the two coupled pitch/heave modes move toward the nose and tail of the slider with increasing tail spacing. Excitation of the first pitch/heave mode, with its center of rotation nearer the tail of the slider, would have less effect on the spacing between a tail-mounted transducer and the disk surface than excitation of the second pitch/heave mode.

Pitch angle also has a more pronounced effect on the center of rotation for the taper-flat slider pad than for the plane wedge, as seen from Figures 4.35 and 4.36. For both slider geometries, decreasing pitch angle causes the rotational centers of the two pitch/heave modes to move towards opposite ends of the slider. In the plane-wedge slider, the center of rotation of the highest frequency mode is nearest the nose of the slider, while it is nearest the tail for the taper-flat geometry.

Yaw angle affects the center of rotation for the plane-wedge and taper-flat slider pads as depicted in Figures 4.37 and 4.38. For the plane wedge, Figure 4.37 shows the center of rotation moving away from the tail with increasing yaw angle for both of the coupled, pitch-heave modes. The same effect is shown in Figure 4.38 for the taper-flat slider pad.

4.4 The Model 2314 Slider

A very early slider design used by IBM Corporation in its disk drives was the Model 2314 slider bearing, shown in Figure 4.39. This slider bearing used a simple spherical surface, with two holes added to reduce the pressure, and thereby decreased the load required to hold the slider at a reasonable distance from the disk surface. Unlike more recent slider designs that are in contact with the stationary disk and "take off" during

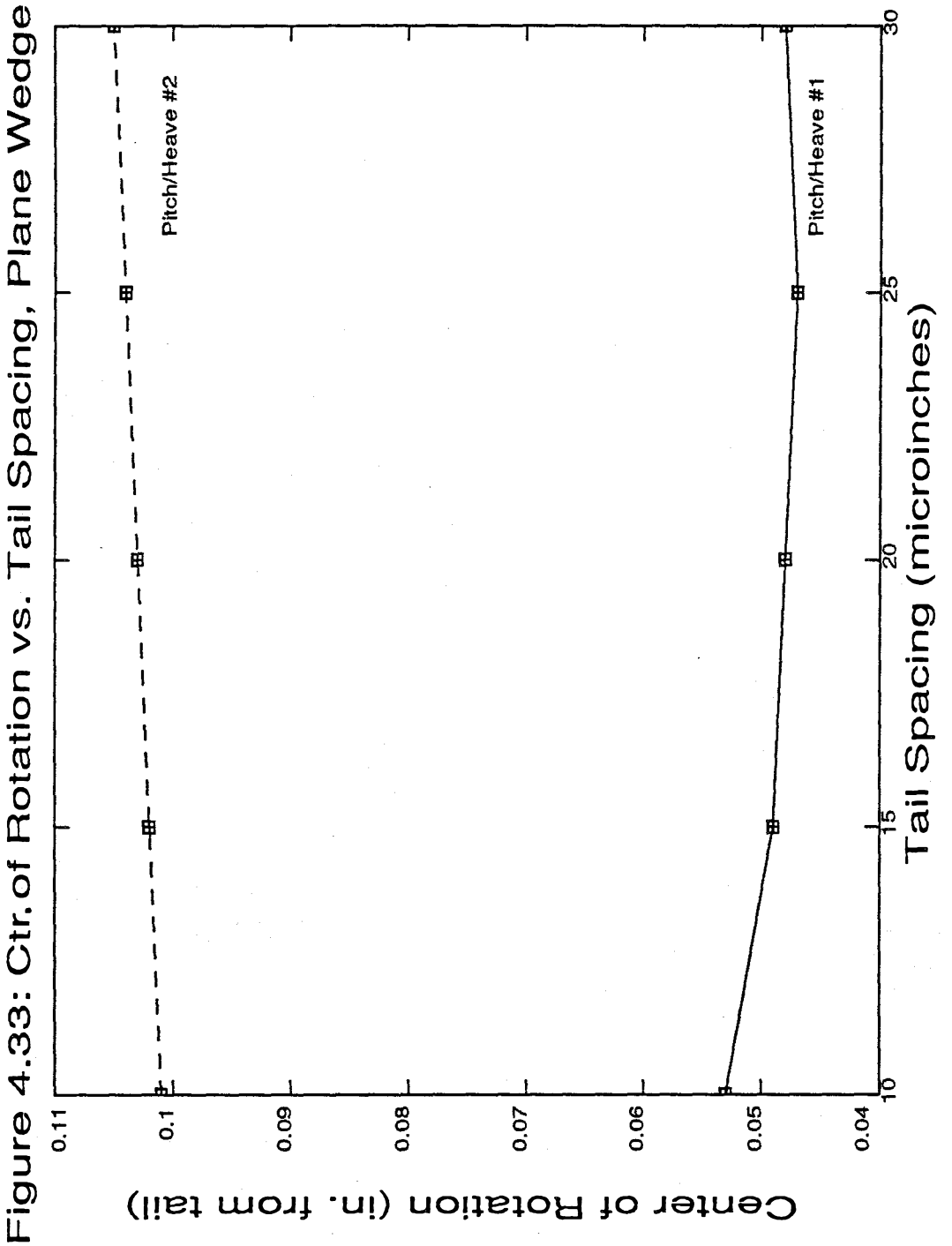

Figure 4.33: Ctr. of Rotation vs. Tail Spacing, Plane Wedge

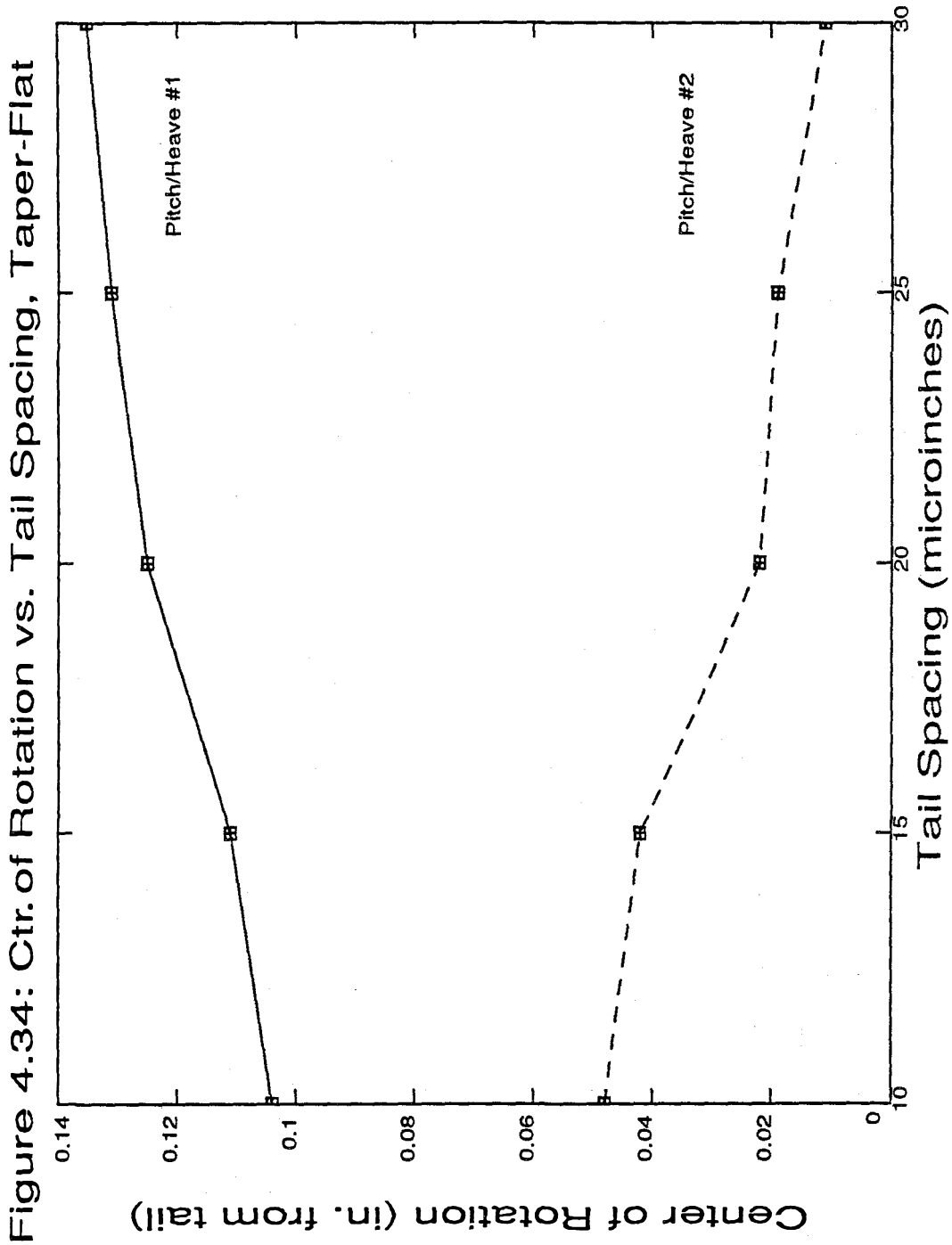

Figure 4.34: Ctr. of Rotation vs. Tail Spacing, Taper-Flat

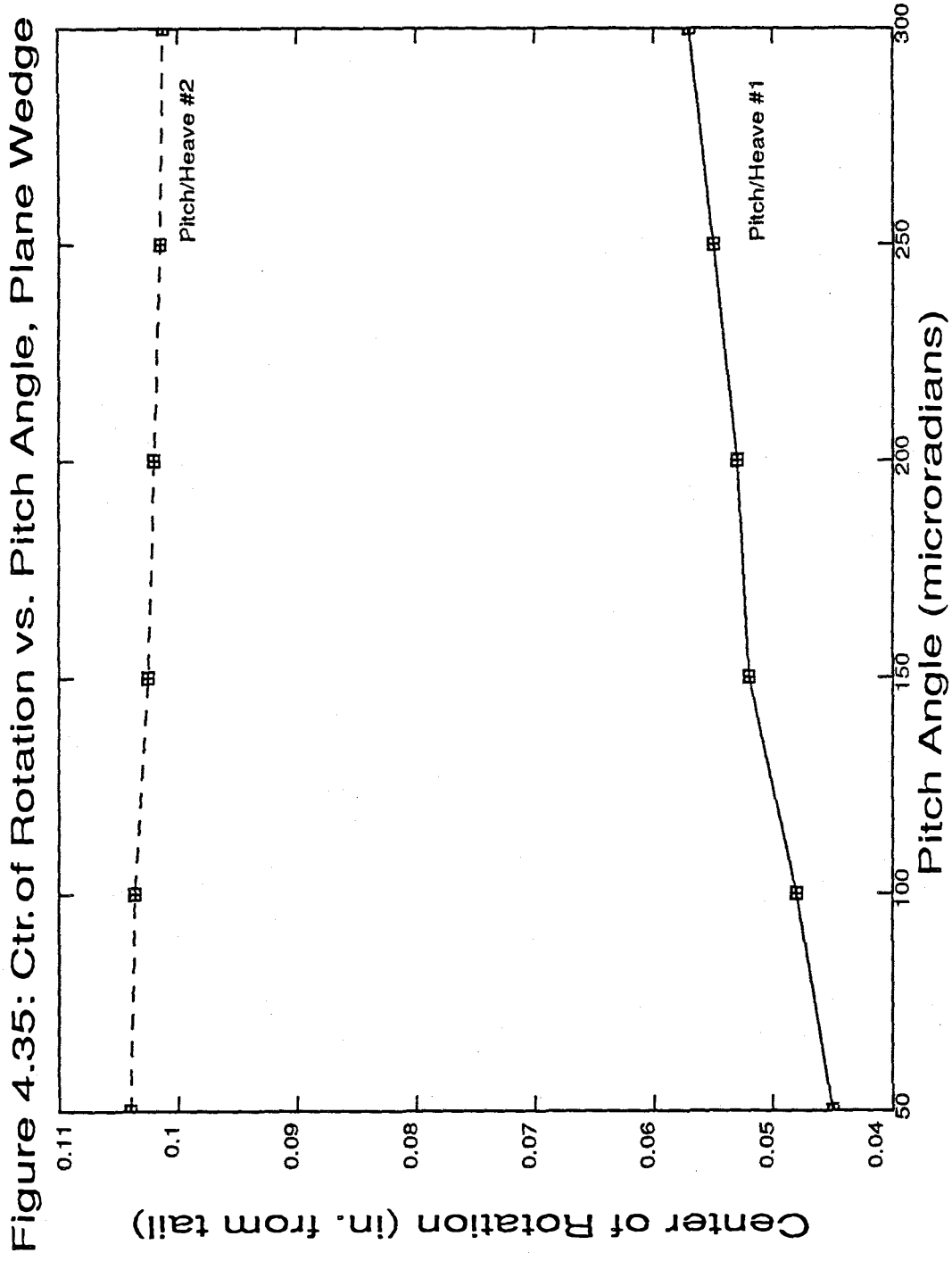

Figure 4.35: Ctr. of Rotation vs. Pitch Angle, Plane Wedge

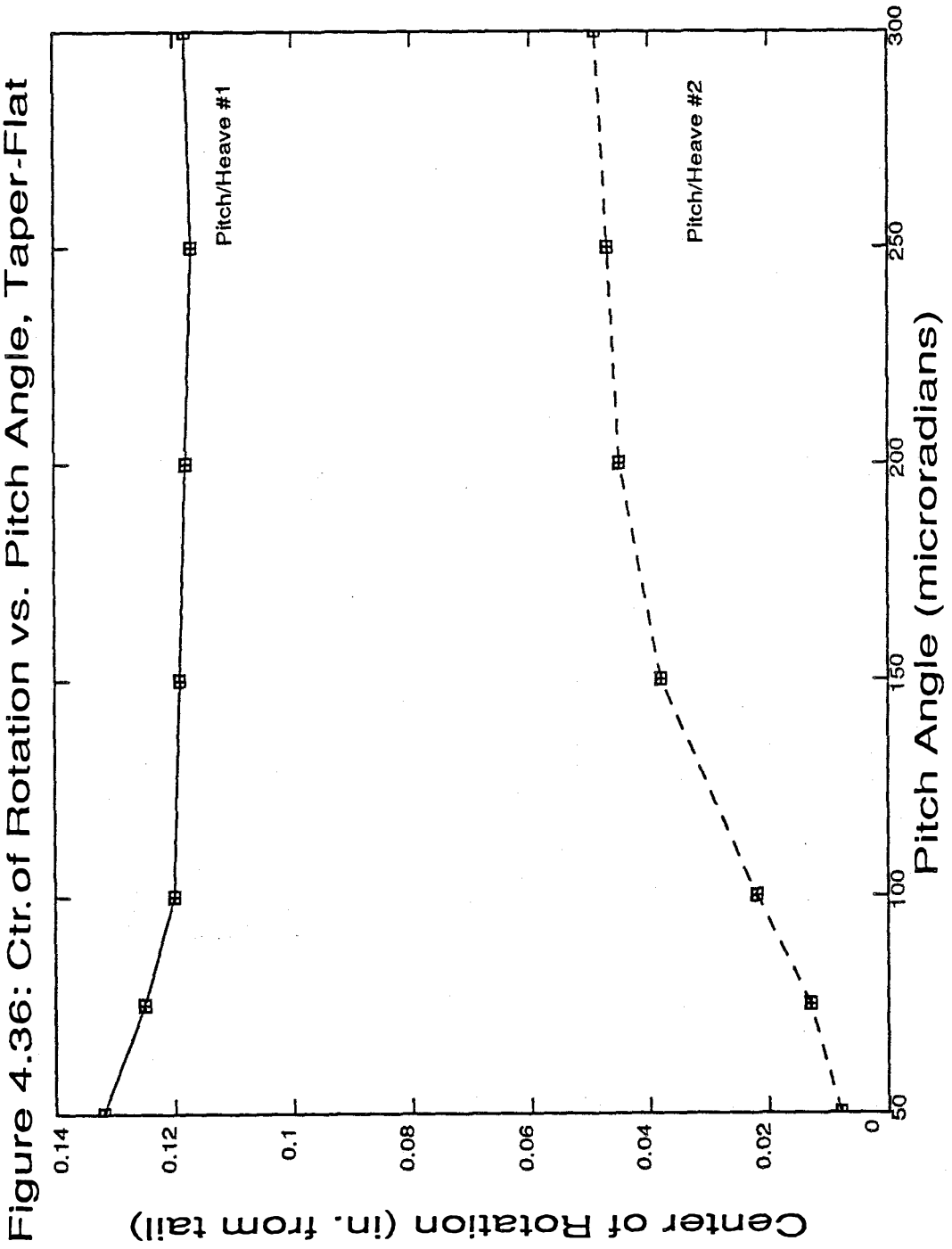

Figure 4.36: Ctr. of Rotation vs. Pitch Angle, Taper-Flat

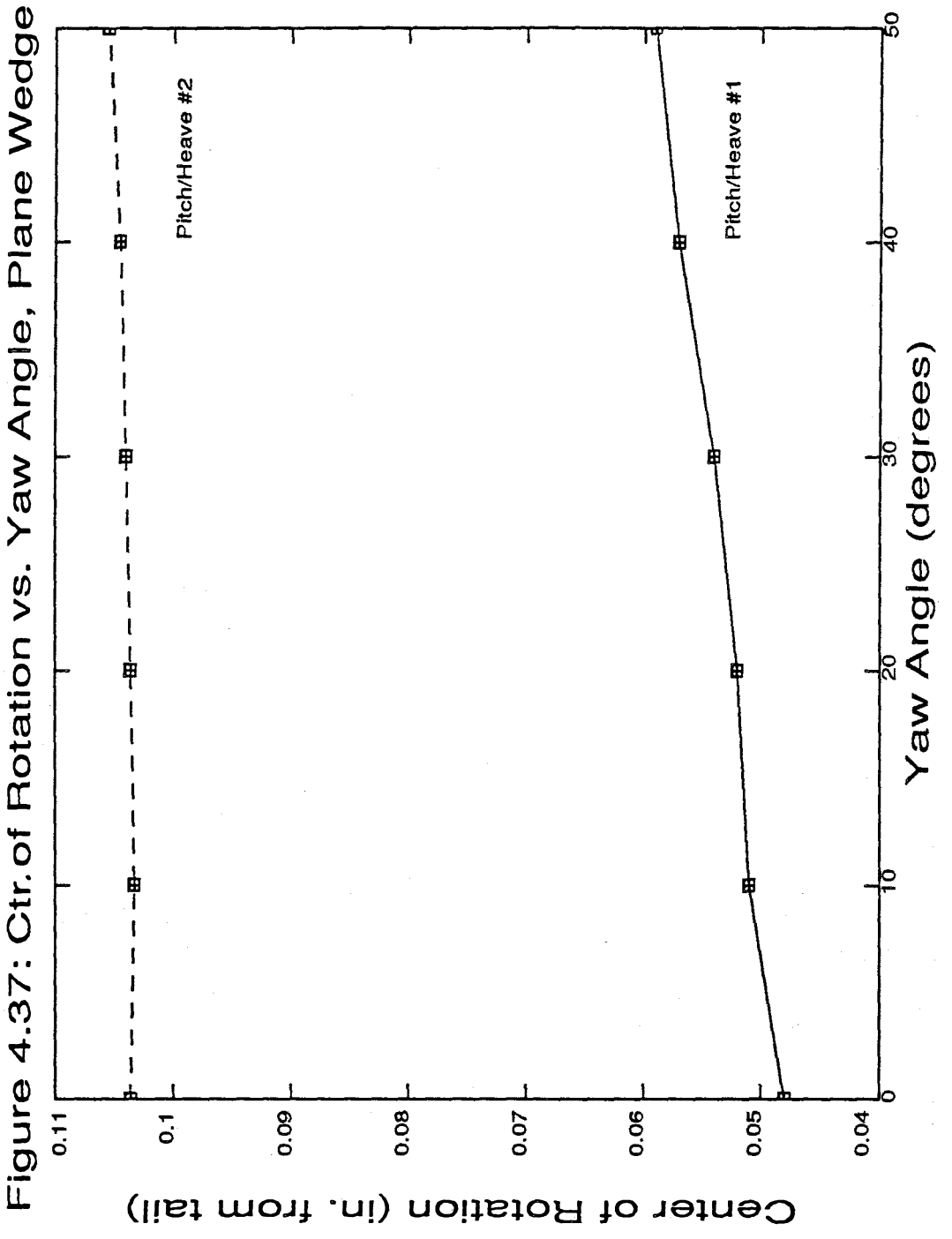

Figure 4.37: Ctr.of Rotation vs. Yaw Angle, Plane Wedge

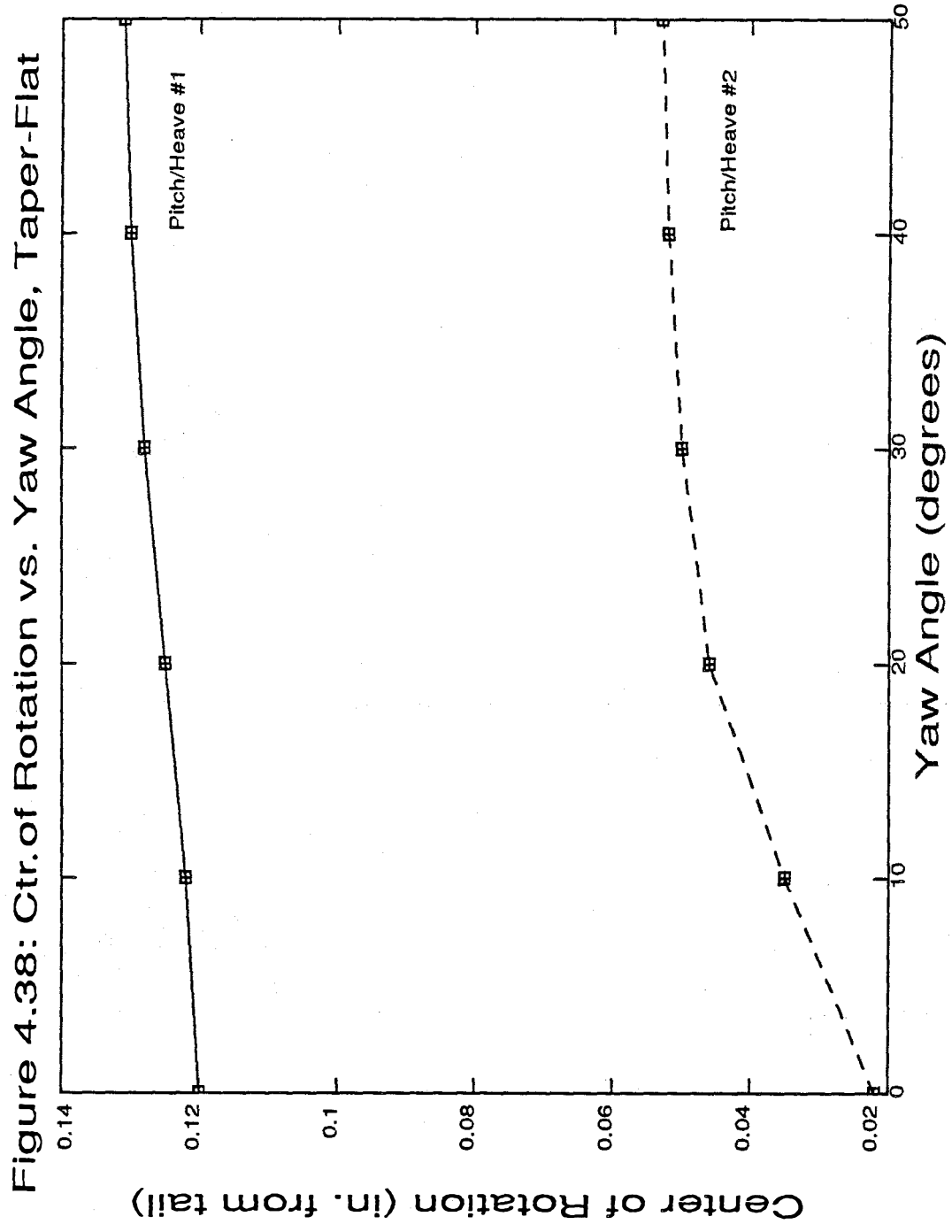

Figure 4.38: Ctr. of Rotation vs. Yaw Angle, Taper-Flat

FIGURE 4.39: MODEL 2314 SLIDER

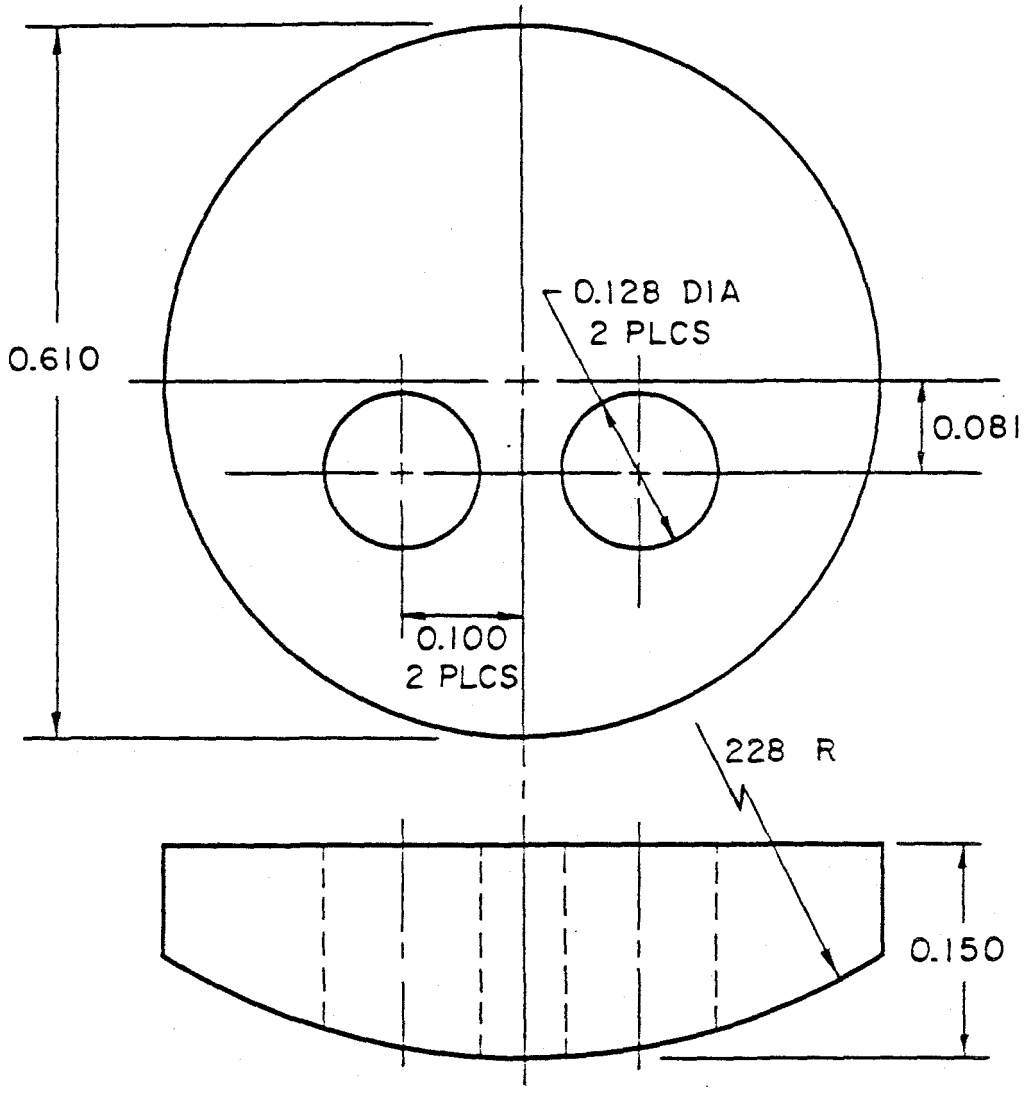

Nominal Operating Parameters:

Surface Speed:	1200 inches/sec
Min. Spacing:	90 μ inches
Pitch Angle:	300 μ radians
Load:	358 grams
Center of Press:	.350 inches from rear

spin-up, the model 2314 was designed to be loaded, by means of a cam mechanism, against a moving disk surface.

Because of the lower data densities recorded on the disk, the dynamics of this slider design were somewhat less critical than the dynamics of its more modern counterparts. Nevertheless, it is interesting to examine this slider to aid in establishing correlation between observed performance and the predictions of the present analytical techniques.

The table below summarizes the dynamic analysis of the Model 2314 slider bearing, which was computed at the following nominal conditions:

Minimum Spacing: 90 microinches

Pitch Angle: 300 microradians

Surface Speed: 1200 inches/sec

Bearing Number: 95.9 .

Mode No.	Component	Norm. Displ.	Freq. (KHz)	Damping Fraction
1	Heave Pitch Roll	0.177 −1.000 0.000	.68	.099
2	Heave Pitch Roll	0.000 0.000 1.000	.85	.216
3	Heave Pitch Roll	0.643 1.000 0.000	3.27	.184

The nominal pressure distribution for the 2314 slider bearing is shown in Figure 4.40. Unlike the other slider bearings examined so far, this design develops a region of pressure less than ambient near the tail, where the spherical, lapped, surface forms an expanding channel with the disk. The two pressure maxima at either side of the slider pad represent the primary source of static load.

The in-phase and out-of-phase perturbation pressure fields for the first coupled, pitch-heave mode are presented in Figures 4.41 and 4.42. The in-phase pressure peaks are concentrated at the rear edges of the slider pad, and their symmetrical location helps to

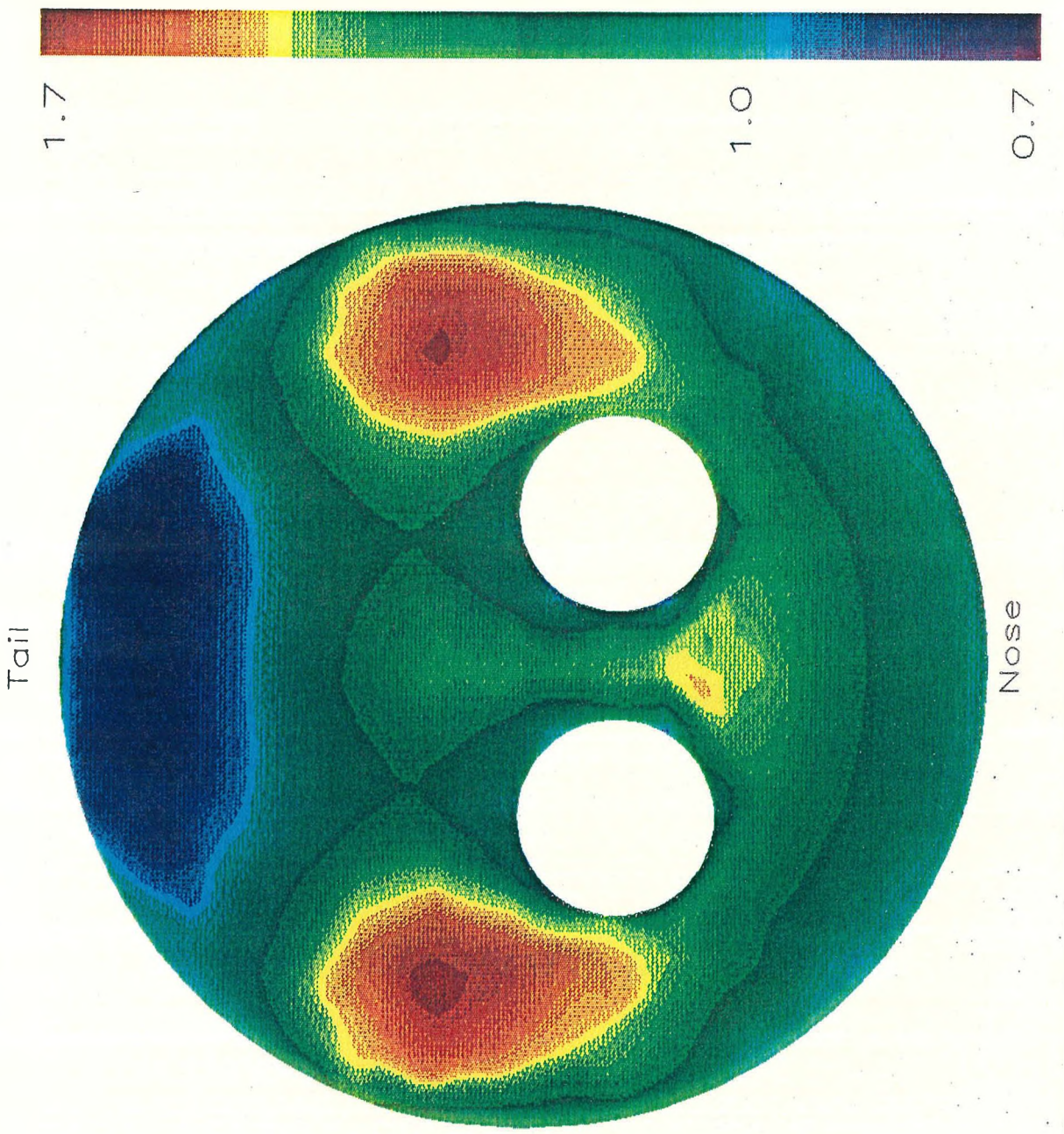

Figure 4.40: 2314 Slider, Static Pressure (atm)

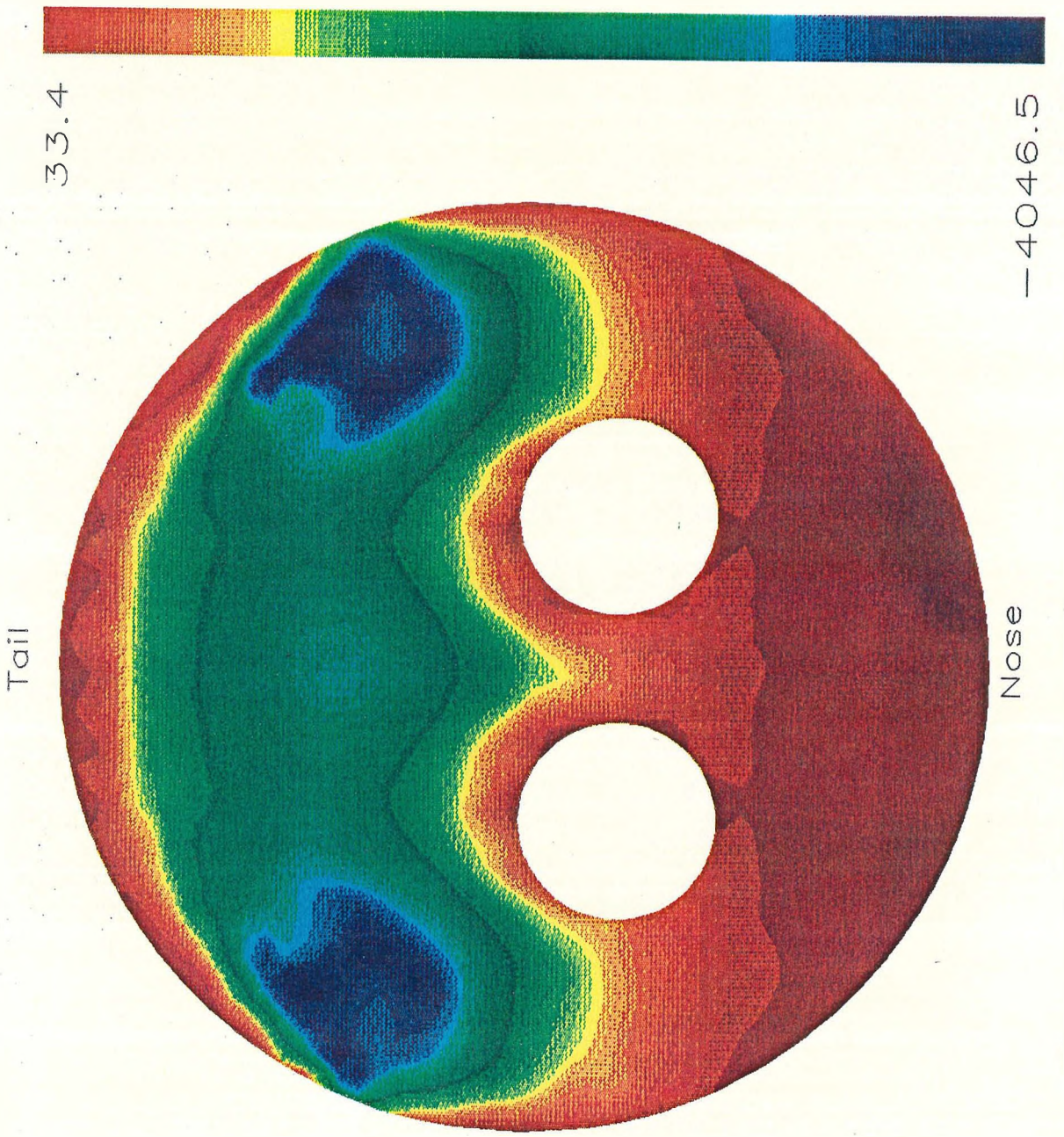

Figure 4.41: 2314 Slider, P–H Mode 1, P1

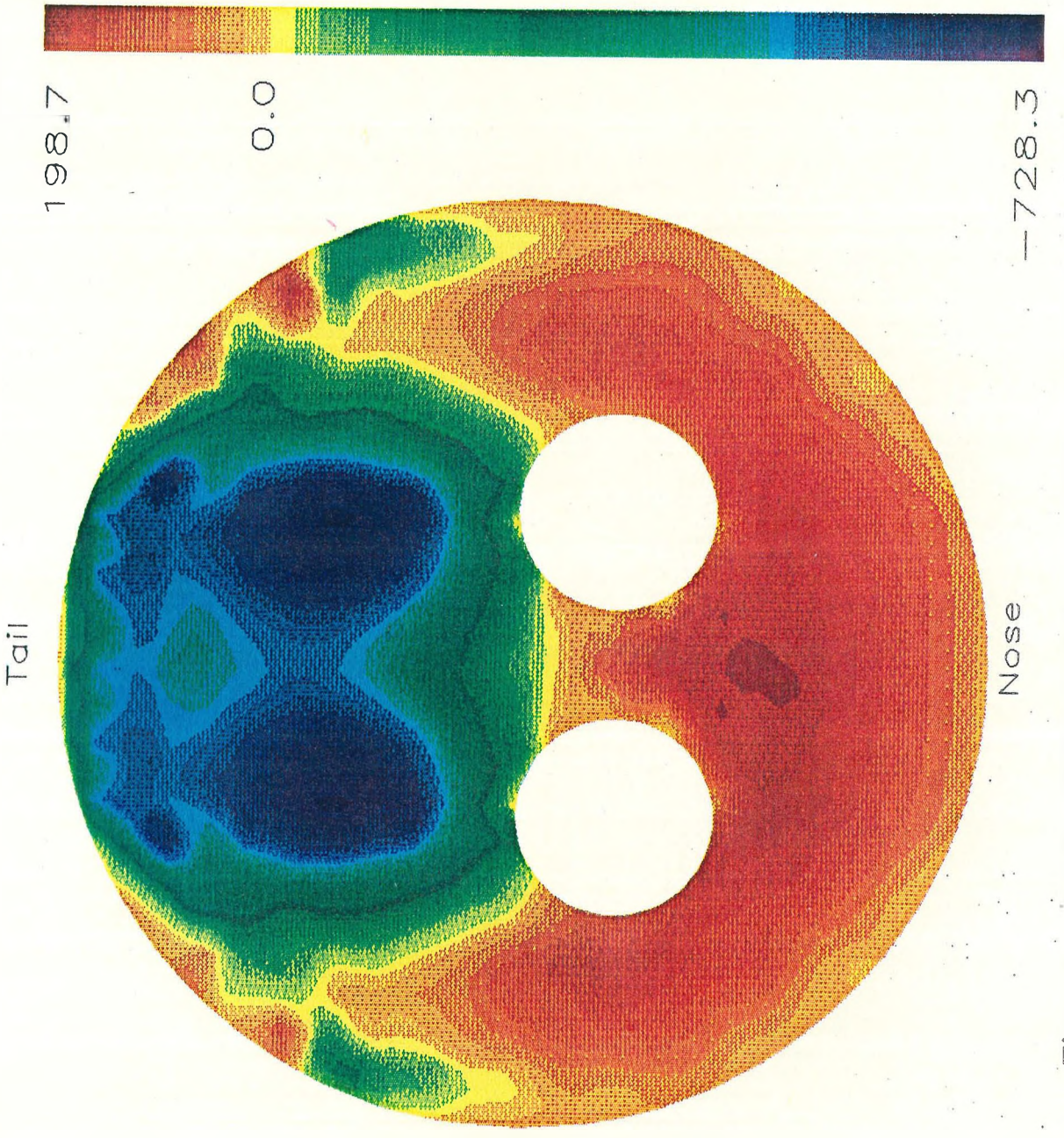

Figure 4.42: 2314 Slider, P–H Mode 1, P2

explain the reduced frequency of this mode. The out-of-phase pressure shows a somewhat more even distribution, with some contribution from the leading portion of the pad, but the largest values are still concentrated near the center portion of the trailing half of the pad.

Perturbation pressure distributions for the roll mode are presented in Figures 4.43 and 4.44. The symmetry and distribution of the pressure peaks for both in-phase and out-of-phase values suggest that the slider bearing should exhibit good roll stability. The slight asymmetry in the values of peak pressure is attributable to computational accuracy.

The second coupled, pitch-heave mode is associated with the perturbation pressure profiles shown in Figures 4.45 and 4.46. While the peak values of in-phase pressure are not as great as in the first pitch-heave mode, the pressure field is more uniformly distributed, resulting in greater stiffness in this mode. Although the out-of-phase pressure peaks appear to be distributed over the entire slider bearing pad surface, there are also large regions of relatively low-pressure values. The resulting fraction of critical damping for this mode is twice that of the first pitch/heave mode.

Experimental observations of the Model 2314 slider show that generally it exhibits good roll stability, but that it has a tendency to "chatter" and become unstable in a pitch/heave mode. This is consistent with the relatively low natural frequency and damping values predicted for the first coupled, pitch/heave mode with the present analysis.

4.5 The Model 3370 Slider

A slider-bearing design widely used in modern disk drives is the IBM 3370 two-rail, taper-flat slider. This slider was designed to carry a magnetic transducer produced by a thin-film vacuum deposition process rather than the conventional wire-wound core. The bearing geometry, shown in Figure 4.47, consists of two separate slider-bearing surfaces, or rails, each of which has a "taper-flat" surface profile. This slider bearing differs from earlier models in that it is designed to rest in contact with the stationary disk surface, and to raise itself up in a stable manner during spin-up. The taper-flat configuration makes this possible, while providing a very stable pressure profile in the slider bearing during operation. This slider bearing is examined at two common nominal operating conditions for which published experimental data exist. The table below shows the nominal operating

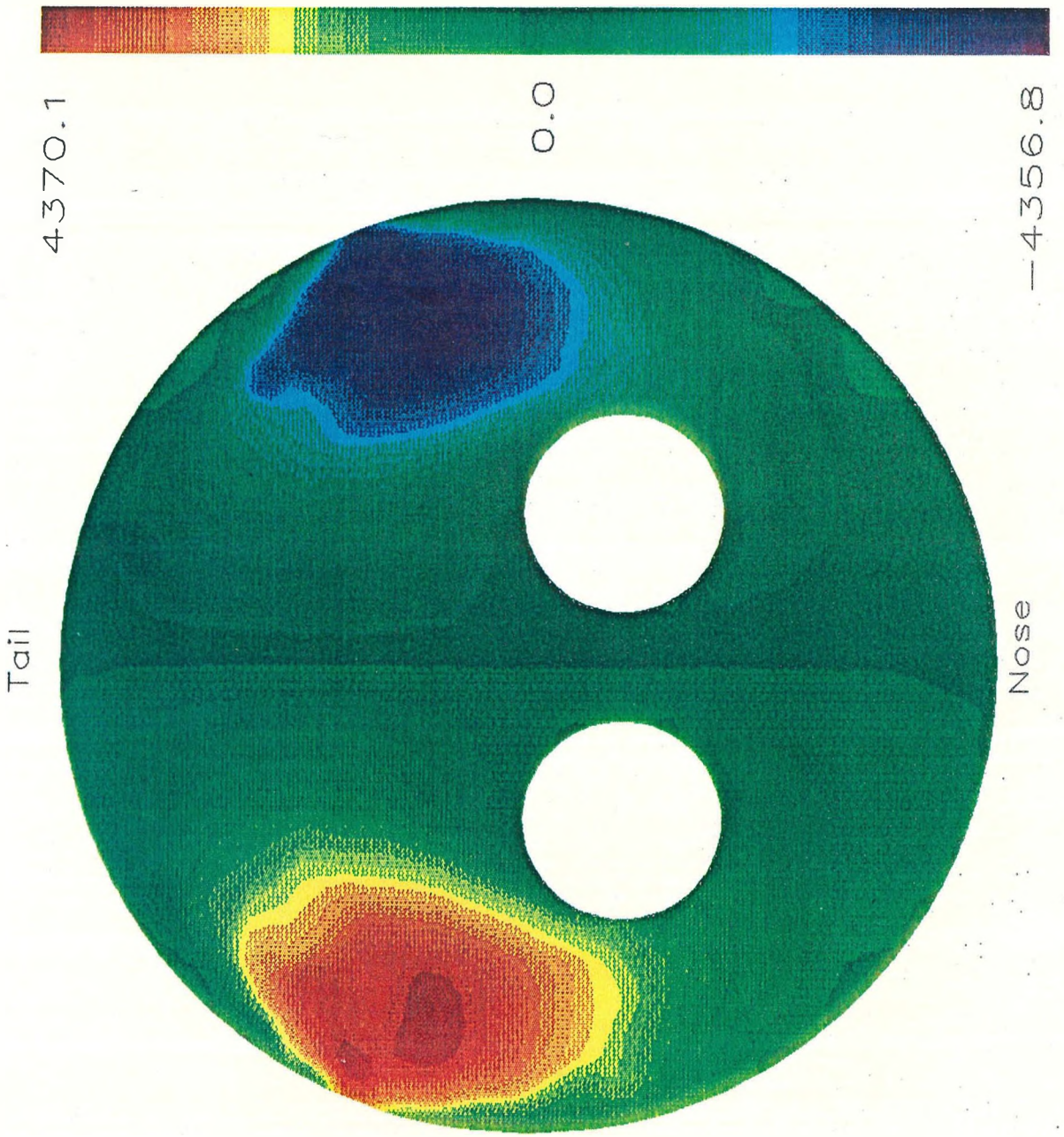

Figure 4.43: 2314 Slider, Roll Mode, P1

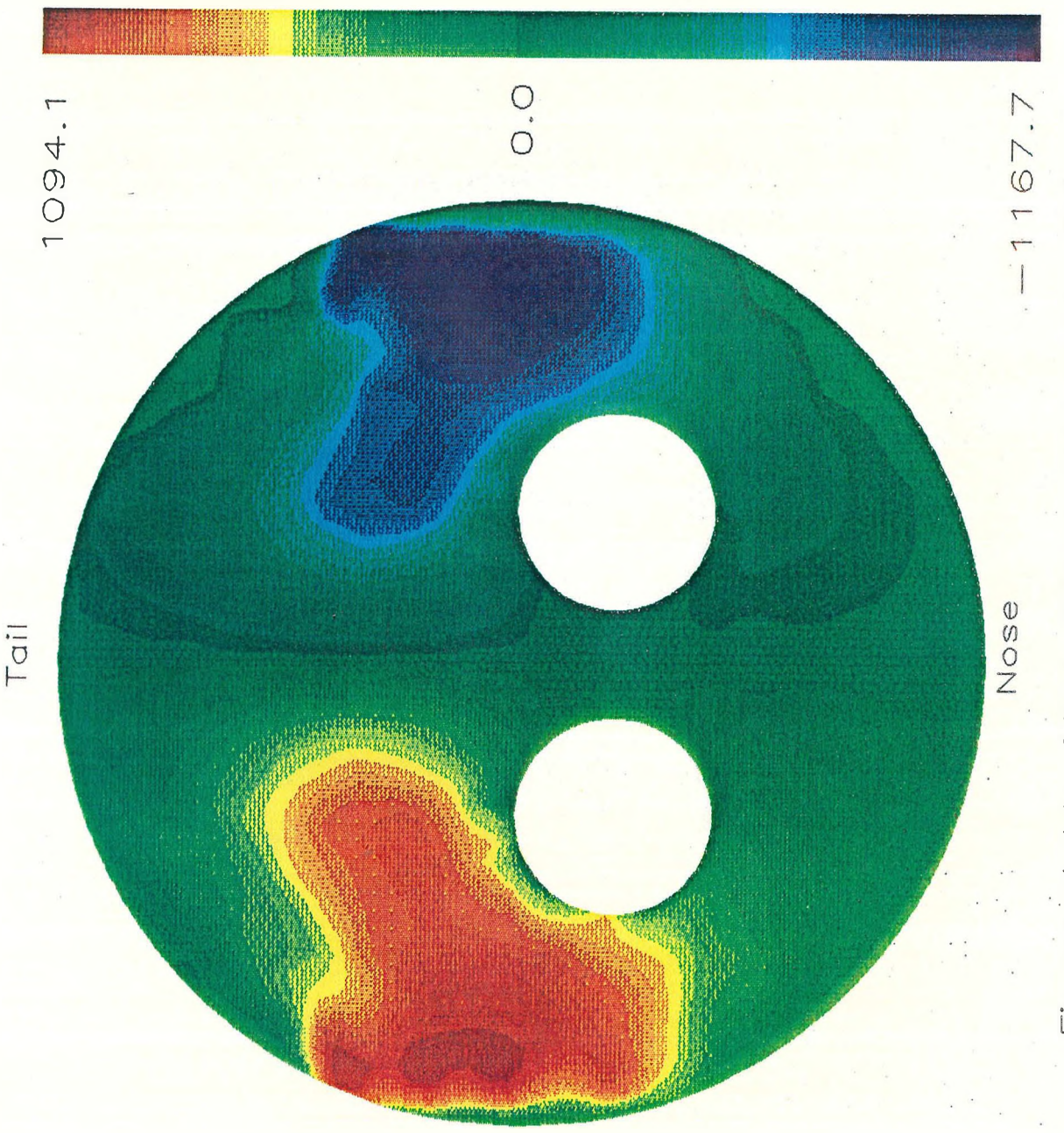

Figure 4.44: 2314 Slider, Roll Mode, P2

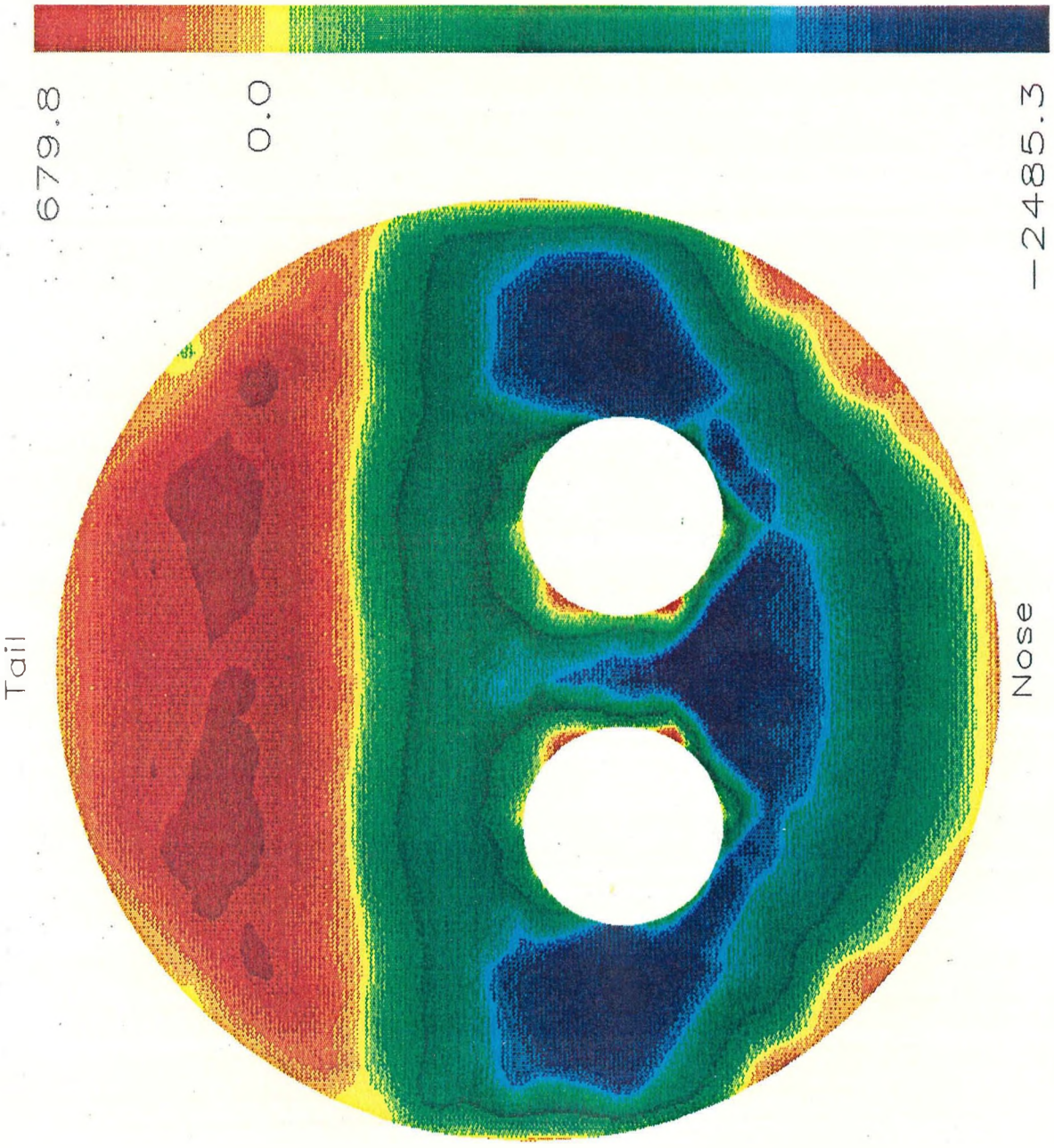

Figure 4.45: 2314 Slider, P–H Mode 2, P1

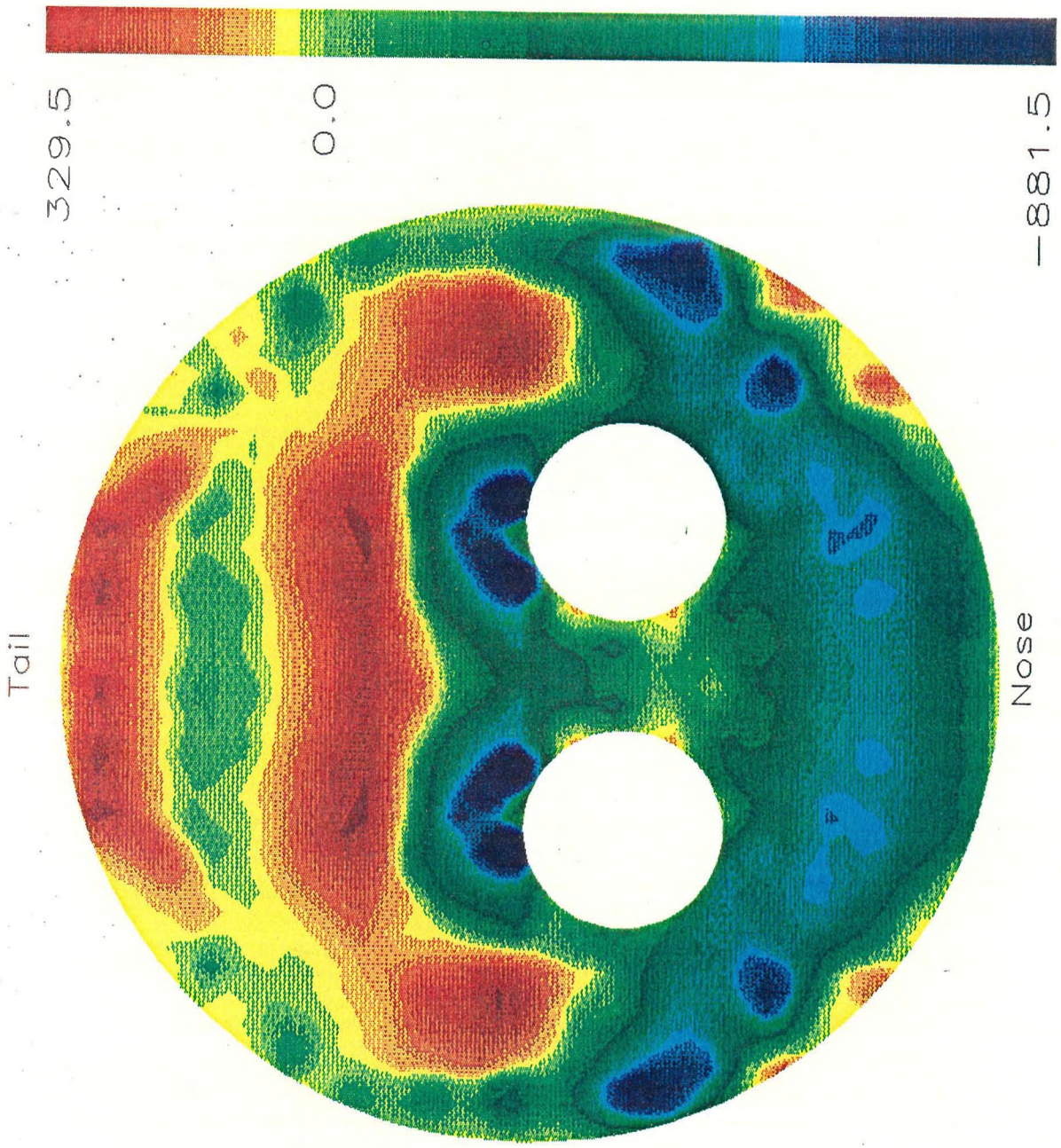

Figure 4.46: 2314 Slider, P−H Mode 2, P2

FIGURE 4.47: MODEL 3370 SLIDER

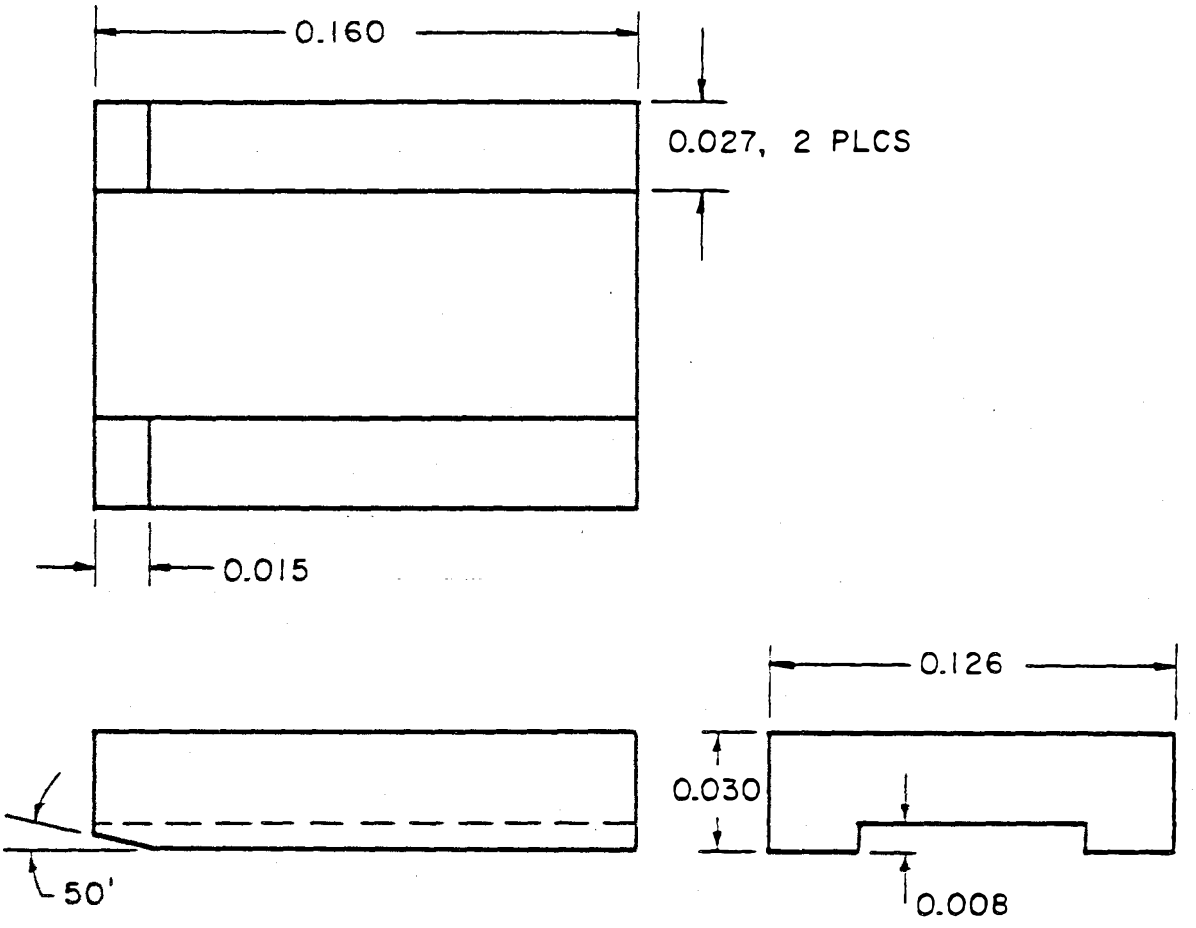

Nominal Operating Parameters:

Inner Radius		Outer Radius	
Surface Speed:	616 inches/sec	Surface Speed:	804.5 inches/sec
Min. Spacing:	19 μ inches	Min. Spacing:	22.9 μ inches
Pitch Angle:	124.2 μ radians	Pitch Angle:	149.5 μ radians
Load:	8.5 grams	Load:	8.7 grams
Center of Press:	.077 inches from rear	Center of Press:	.076 inches from rear

conditions for the dynamic analysis of the Model 3370 slider bearing, as well as the resulting natural frequencies, modal damping, and mode shapes:

Inner Disk Radius		Outer Disk Radius	
Surface Speed	= 616 in/sec	Surface Speed	= 804.5 in/sec
Min. Spacing	= 19.5 microinches	Min. Spacing	= 22.9 microinches
Pitch Angle	= 124.2 microradians	Pitch Angle	= 149.5 microradians
Load	= 8.5 grams	Load	= 8.7 grams
Ctr. of Pres.	= .077 inches from rear	Ctr. of Pres.	= .076 inches from rear
Bearing No.	= 281.47	Bearing No.	= 266.49 .

Dynamic Results at Inner Disk Radius

Mode No.	Component	Norm. Displ.	Freq. (KHz)	Damping Fraction
1	Heave Pitch Roll	0.296 −1.000 0.000	11.74	.117
2	Heave Pitch Roll	−1.000 −0.547 0.000	17.08	.054
3	Heave Pitch Roll	0.000 0.000 1.000	20.48	.071

Dynamic Results at Outer Disk Radius

Mode No.	Component	Norm. Displ.	Freq. (KHz)	Damping Fraction
1	Heave Pitch Roll	0.297 −1.000 0.000	10.40	.173
2	Heave Pitch Roll	−1.000 −0.569 0.000	15.59	.058
3	Heave Pitch Roll	0.000 0.000 1.000	18.65	.075

The above data suggest that the change from inner to outer disk radius flying conditions produces very little change in the dynamic performance of the slider-bearing system. The corresponding natural frequencies show a slight decrease, while the modal damping fractions are increased by a small amount at the outer radius condition. The static and perturbation pressure fields for the inner and outer radius conditions show the same general features, and only the inner radius plots are included for discussion in the remainder of this section.

The nominal static pressure field for the 3370 slider is shown in Figure 4.48. The distribution of the pressure peaks at the four corners of the slider body was intended to increase the stability of the slider-bearing system and is quite different from the Model 2314 design, Figure 4.40, with its two concentrated, centralized pressure peaks.

Figures 4.49 through 4.54 show the in-phase and out-of-phase pressure distributions for the three natural frequencies of the slider-bearing system, corresponding to the values in the table above for the inner radius condition. Both in-phase and out-of-phase perturbation pressures appear to have their peak values located near the corners of the slider body in the first, coupled, pitch-heave mode (Figures 4.49 and 4.50). The center of rotation for this mode is near the geometrical center, and both ends of the slider undergo nearly equal vertical displacement in this predominantly pitching mode.

The perturbation pressures show more localized peaks, near the taper-flat transition, in the second, coupled, pitch-heave mode (Figures 4.51 and 4.52). For this case, the center of rotation is behind the tail, the nose of the slider experiences a larger vertical displacement than the tail, and the perturbation pressure is therefore larger near the nose of the slider.

In each of these first two modes, the out-of-phase perturbation pressure, representing the contribution of the gas bearing to damping, exhibits maximum values along the outside edges of the slider pads. The uncoupled roll mode, Figures 4.53 and 4.54, shows a fairly even distribution of peak values along the outside pad edges as well, with virtually no contribution from the front taper region of the pads. It appears as though regions of the gas film that have high transverse pressure gradients, such as at the outer pad edges of the taper-flat slider, form the largest out-of-phase pressure peaks, and thus make a significant contribution to damping.

Experimental results for the Model 3370 slider were recently reported by Miu (40). Using a laser-doppler vibrometer, Miu obtained dynamic measurements of the slider bear-

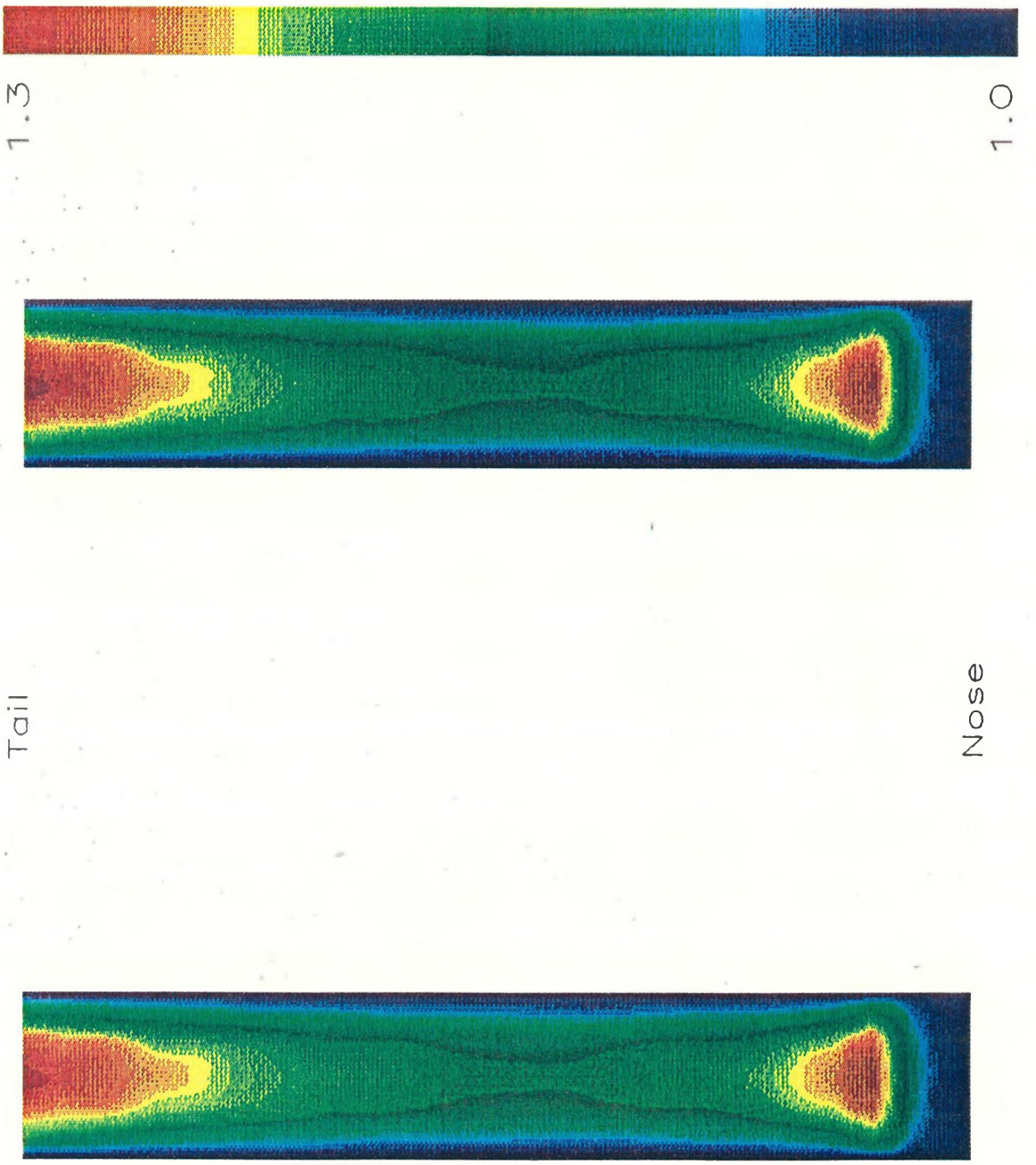

Figure 4.48: 3370 Slider, Static Pressure (atm)

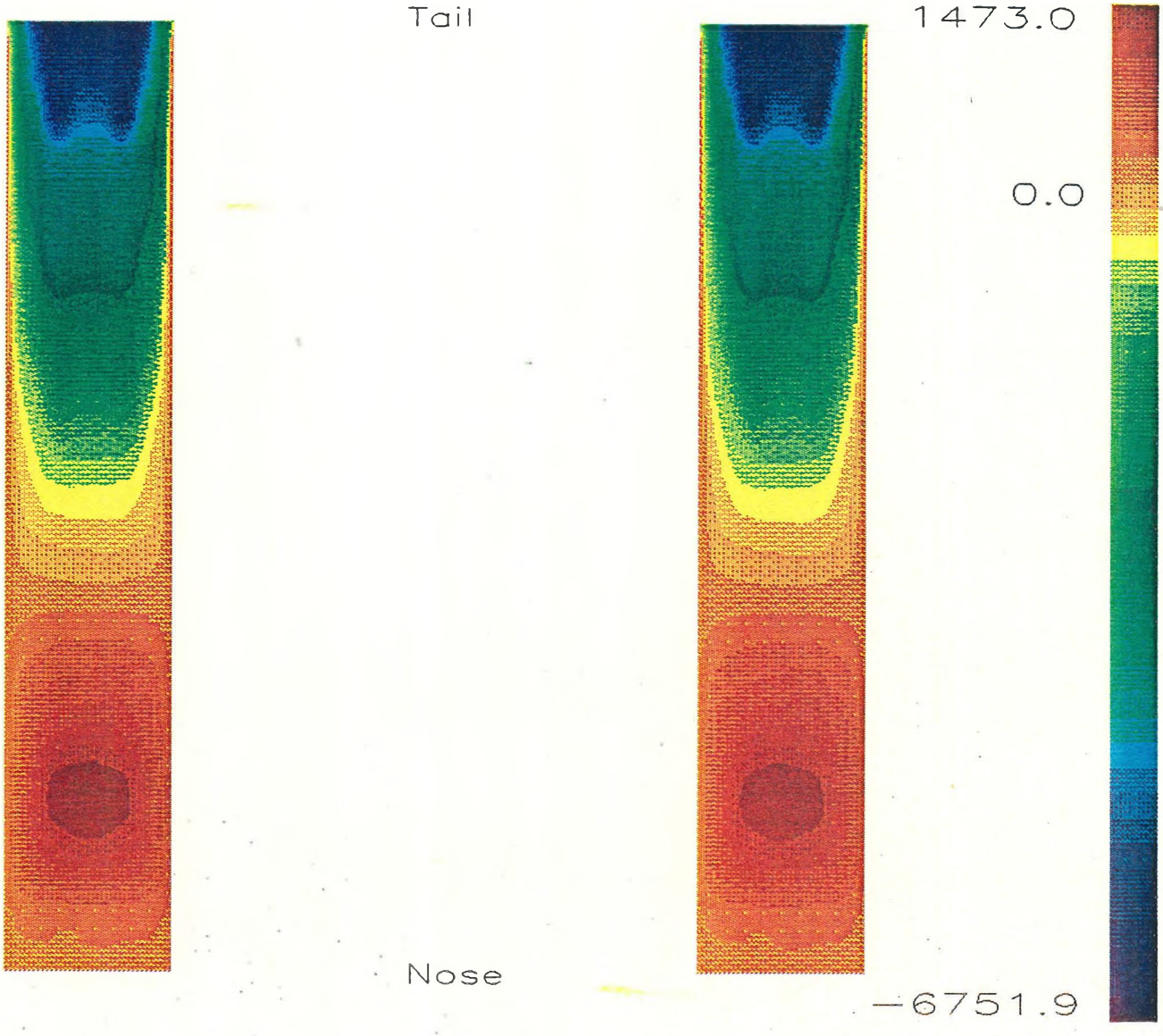

Figure 4.49: 3370 Slider, P—H Mode 1, P1

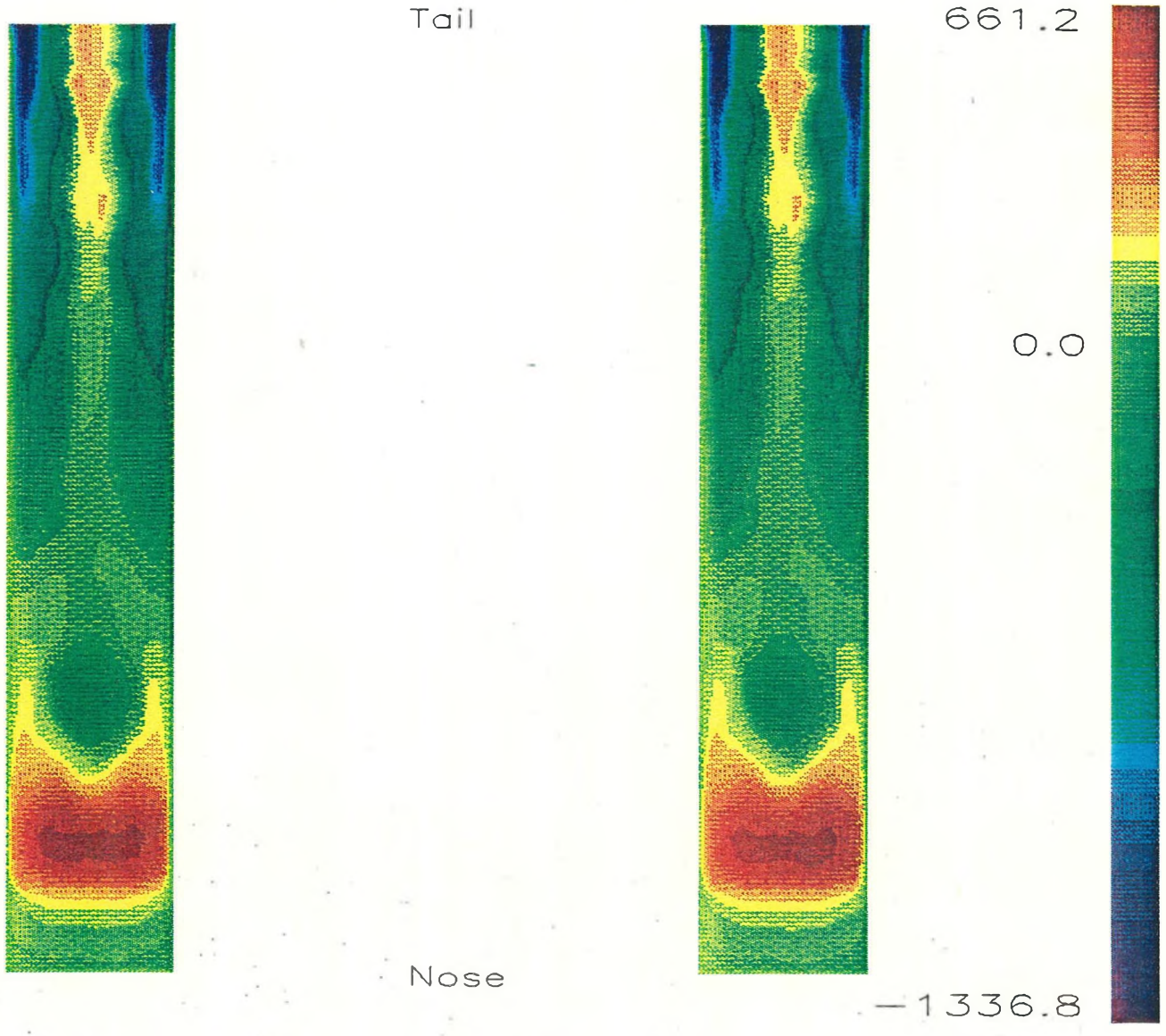

Figure 4.50: 3370 Slider, P−H Mode 1, P2

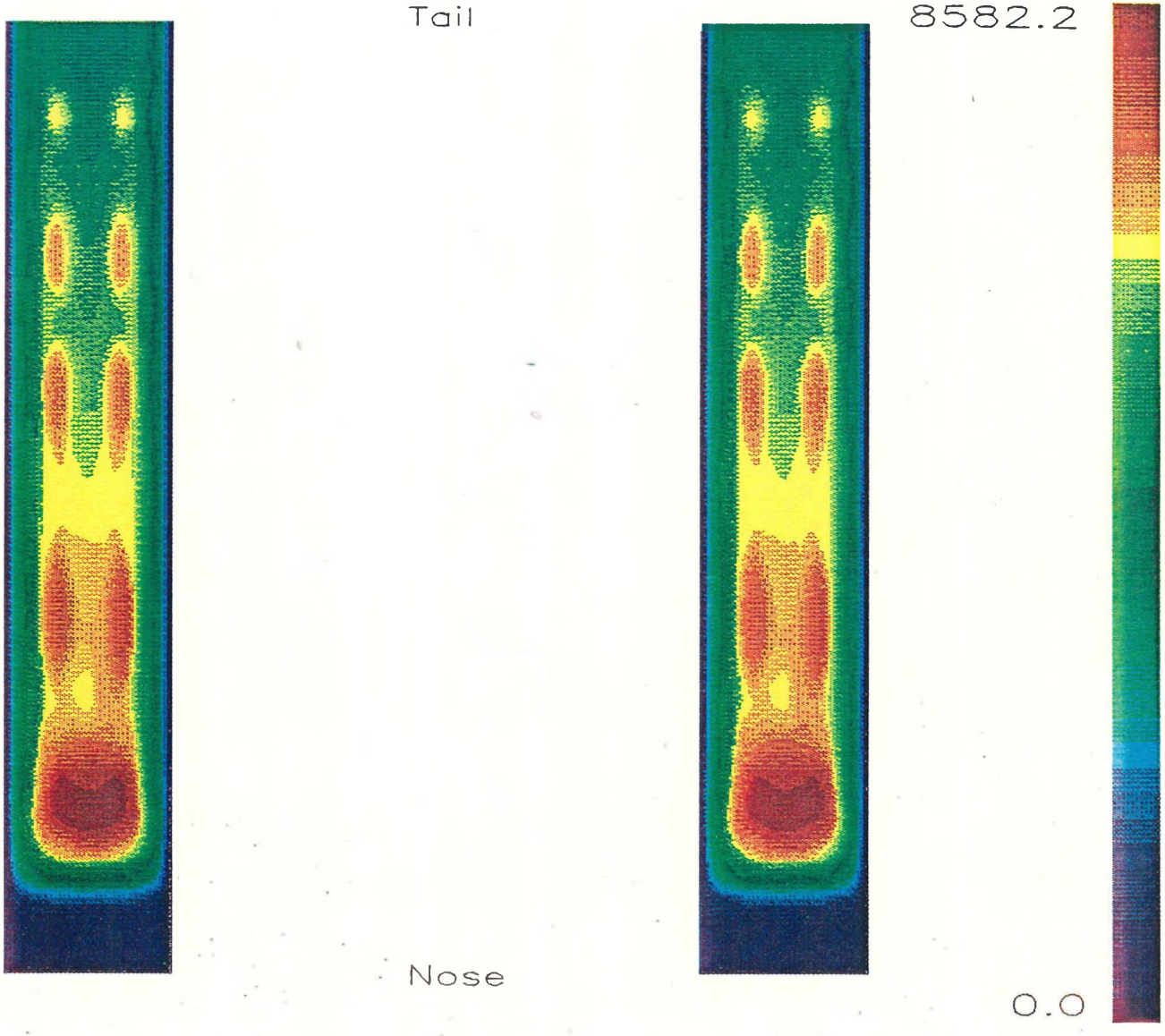

Figure 4.51: 3370 Slider, P–H Mode 2, P1

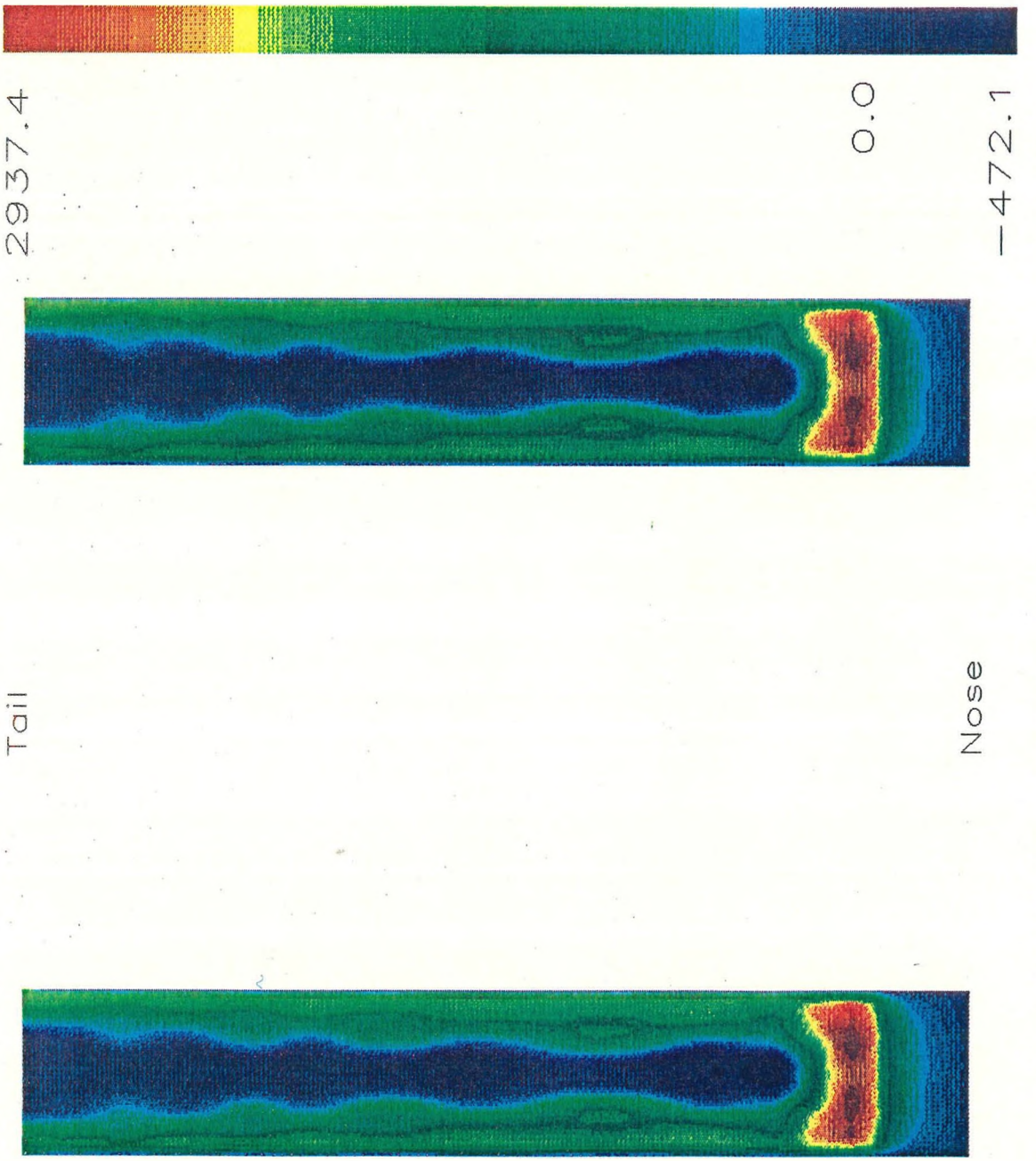

Figure 4.52: 3370 Slider, P—H Mode 2, P2

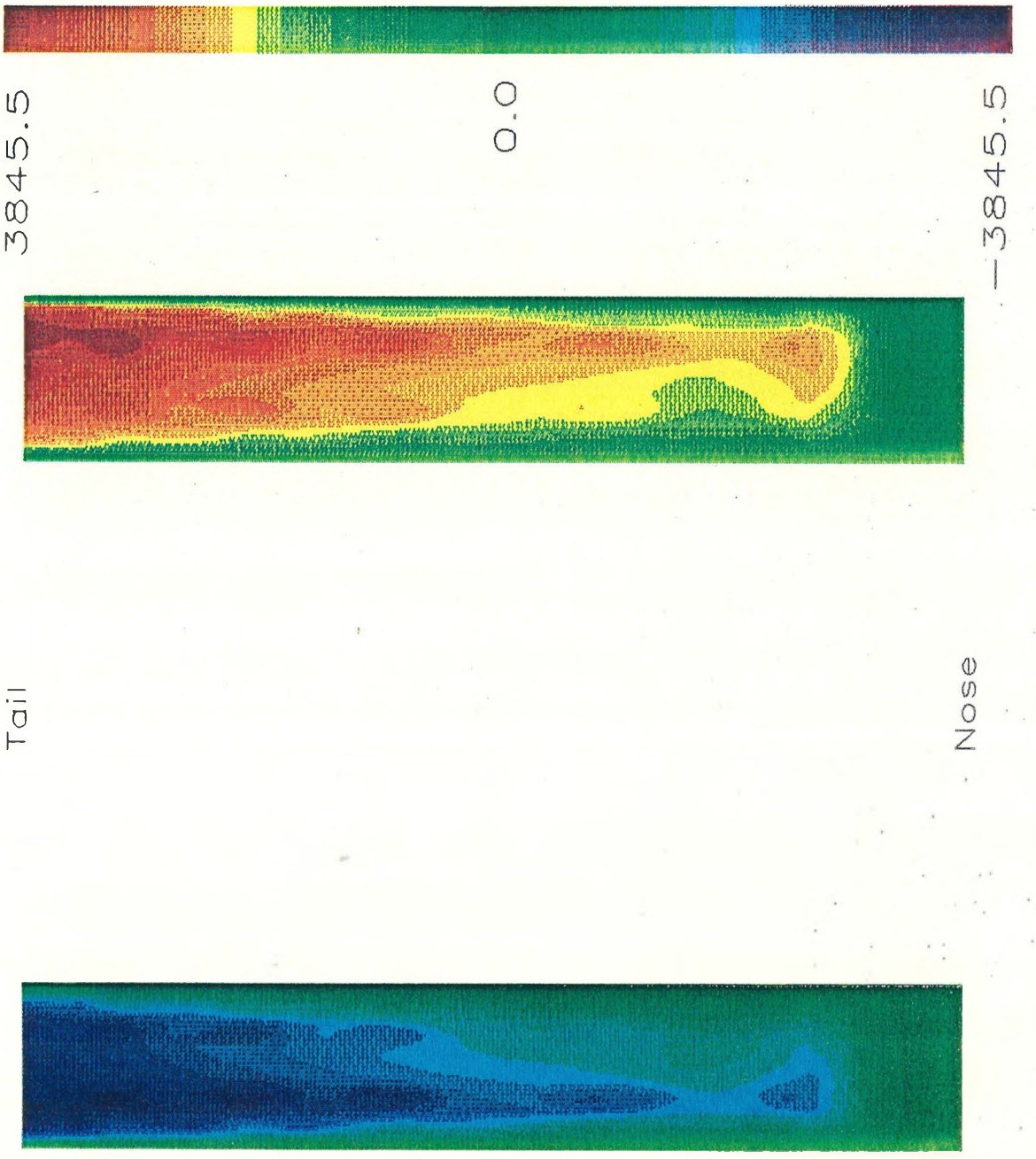

Figure 4.53: 3370 Slider, Roll Mode, P1

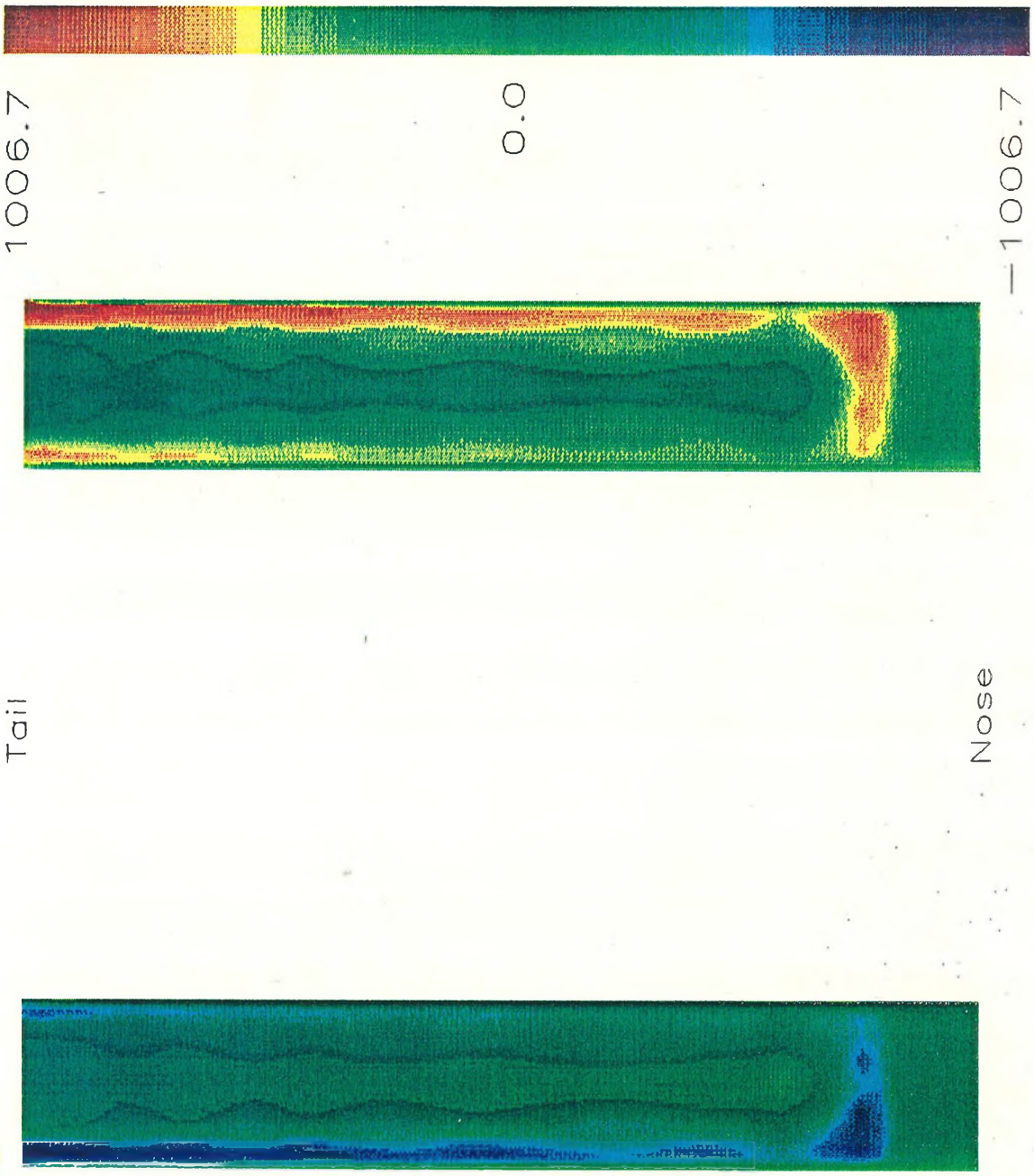

Figure 4.54: 3370 Slider, Roll Mode, P2

ing without interfering with its motion. Although Miu identified two coupled, pitch-heave modes, and an uncoupled roll mode of slider body oscillation, no attempt was made to quantify the mode shapes further. Damping values were also not obtained, but the frequencies are compared with the calculated values from this thesis in the table below.

Theory vs. Experiment

Radius	Mode No.	Computed Frequency	Measured Frequency
Inner	1	11.7	12.0
	2	17.1	18.0
	3	20.5	17.0
Outer	1	10.4	10.0
	2	15.6	15.0
	3	18.7	13.0

Note: First two modes are coupled pitch-heave, third is roll.

4.6 Response to Disk Displacement

The primary function of the slider-bearing system is to maintain a small, constant spacing between the magnetic transducer and the surface of the rotating disk. Displacement of the disk surface may result from several factors, including axial motion of the spindle shaft, vibration of the disk at its natural frequencies, buffeting from air flow in the disk-drive enclosure, or runout because of a deviation from flatness. This latter cause is a primary contributor to vertical displacement of the disk during normal operation.

One of the advantages of the modal analysis approach developed in Chapter 3 is the ability to compute the response to various inputs without solving the complete coupled, time-dependent equations for the gas-bearing and slider system. As an example, consider the response of the Model 3370 slider, under the conditions existing at the inner disk radius defined in Section 4.5, to a sinusoidal vertical displacement of the disk.

The following disk surface displacement is typical of that which might be encountered by the 3370 slider bearing:

$$\{\xi_d(t)\} = \begin{Bmatrix} z_d \\ 0 \\ 0 \end{Bmatrix} \sin \omega_o t \,, \tag{4.1}$$

where

$$z_d = .001''$$

$$\omega_o = 377 \text{ rad/sec} \,.$$

A rotational speed of 3600 rpm is commonly used in disk drives, and thus a disk displacement at 60 Hz (377 rad/sec) was chosen here to represent the fundamental runout frequency.

Because the stiffness and damping matrices, $[K_s]$ and $[C_s]$ in Equation 3.43, are functions of frequency, Equation 3.44 for the forcing function becomes

$$\begin{aligned} Q_r(t) = \omega_o \left\{\hat{\eta}^{(r)}\right\}^T [M]^{-1} \left[C_s^{(r)}\right] \left\{\bar{\xi}_d\right\} \cos\omega_o t \\ + \left\{\hat{\eta}^{(r)}\right\}^T [M]^{-1} \left[K_s^{(r)}\right] \left\{\bar{\xi}_d\right\} \sin\omega_o t \; ; \qquad r = 1,3,5 \end{aligned} \tag{4.2}$$

In evaluating Equation 4.2 numerically, the stiffness and damping matrices are computed from tables generated by the finite element perturbation solution. This is accomplished using cubic splines, as was done for the modal solution described in Chapter 3.

Once a value of $Q_r(t)$ has been obtained for each mode from Equation 4.2, Equation 3.41 can be used to compute the displacement vector for the center of mass of the slider body. The minimum clearance for the slider body is calculated by combining the effects of pitch angle and roll angle in addition to the vertical displacement. This solution assumes zero initial conditions, i.e., that the slider is operating in its equilibrium configuration prior to the beginning of disk displacement. The response consists of a transient and a steady-state portion.

Figure 4.55 shows the initial transient solution for the first millisecond after the disk displacement begins. The transient response has almost completely damped out in this time, and the slider-body displacement has settled into its steady-state behavior. The transient solution shows effectively how the slider responds to a ramp displacement of the disk surface, indicating that it reaches steady-state conditions in less than one-sixteenth of the period of disk rotation.

In order to verify the damping values obtained with the present analysis, results were compared with those from a time-domain, finite-difference model. The finite-difference analysis was sensitive to the boundary condition at the tail, and to the placement of the grid points. The present finite element method did not exhibit either of these sensitivities. With careful grid placement and enforcement of the ambient pressure boundary condition at the tail, the damping values obtained with the two different methods, for the taper-flat slider shown in Figure 4.47, were in close agreement. The present method was also used to analyze the slider modeled by Ono, et al. (35), and good agreement was obtained here as

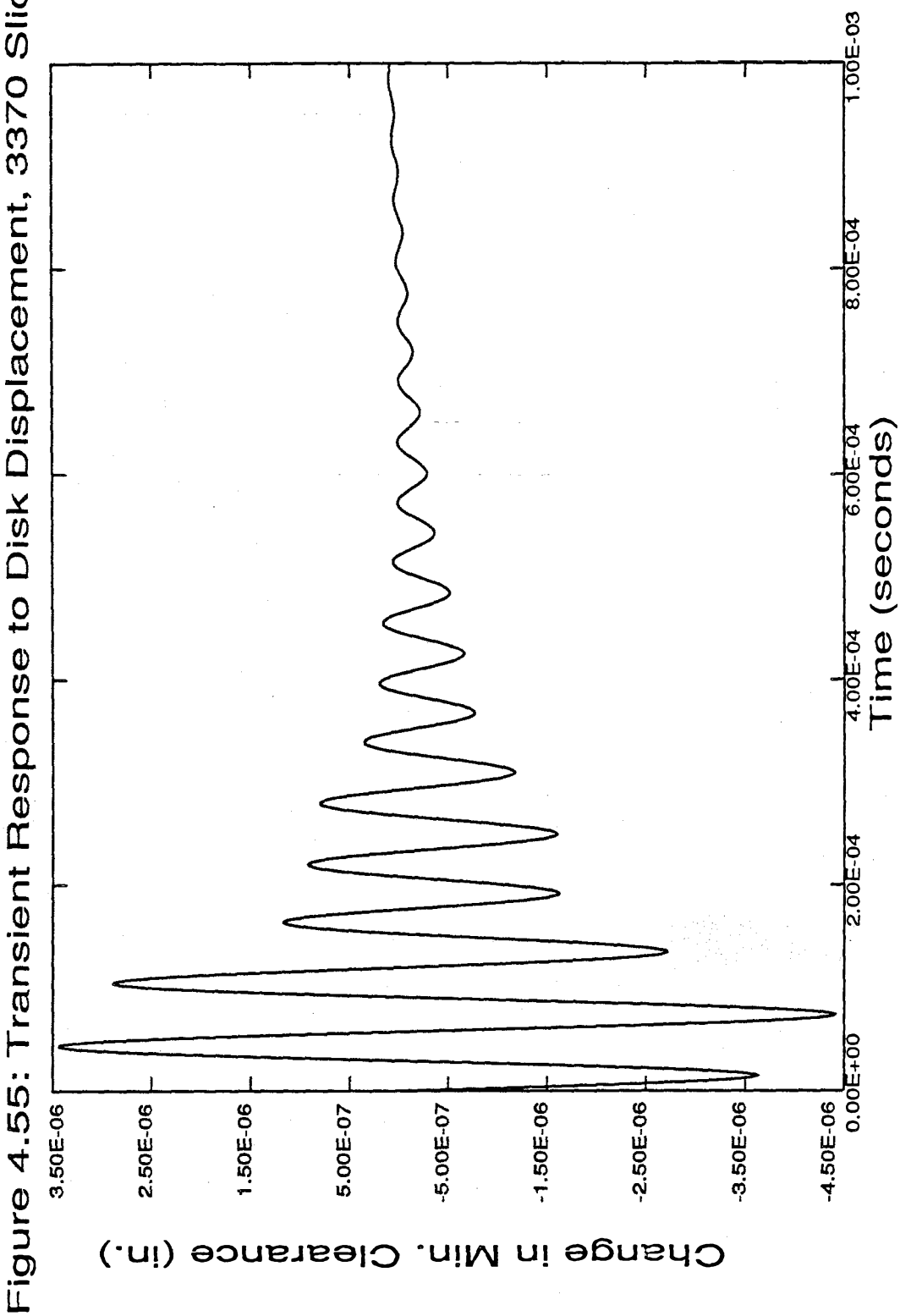

Figure 4.55: Transient Response to Disk Displacement, 3370 Slider

well.

The time-history of minimum slider clearance, for 1 sec $< t <$ 1.016 sec, is shown in Figure 4.56. The steady-state solution for the displacement of the center of mass of the slider body, from which the minimum clearance in Figure 4.56 is obtained, is given in Equation 4.3 below.

$$\begin{aligned}\{\xi_j(t)\} = \sum_{r=1,3,5} \frac{2\{|\eta_r^j|\}}{|g_r^*|} \Bigg[& \cos(\omega_{d_r} t + \phi_r) \Bigg\{ \frac{(A_r\omega_1 - B_r\zeta_r\omega_r)\sin\omega_1 t}{2(\zeta_r^2\omega_r^2 + \omega_1^2)} \\ & + \frac{(B_r\omega_1 + A_r\zeta_r\omega_r)\cos\omega_1 t}{2(\zeta_r^2\omega_r^2 + \omega_1^2)} + \frac{(A_r\omega_2 - B_r\zeta_r\omega_r)\sin\omega_2 t}{2(\zeta_r^2\omega_r^2 + \omega_2^2)} \\ & + \frac{(A_r\zeta_r\omega_r - B_r\omega_2)\cos\omega_2 t}{2(\zeta_r^2\omega_r^2 + \omega_2^2)} \Bigg\} + \sin(\omega_{d_r} t + \phi_r) \Bigg\{ \frac{(A_r\zeta_r\omega_r + B_r\omega_1)\sin\omega_1 t}{2(\zeta_r^2\omega_r^2 + \omega_1^2)} \\ & + \frac{(B_r\zeta_r\omega_r - A_r\omega_1)\cos\omega_1 t}{2(\zeta_r^2\omega_r^2 + \omega_1^2)} + \frac{(A_r\zeta_r\omega_r - B_r\omega_2)\sin\omega_2 t}{2(\zeta_r^2\omega_r^2 + \omega_2^2)} \\ & - \frac{(B_r\zeta_r\omega_r + A_r\omega_2)\cos\omega_2 t}{2(\zeta_r^2\omega_r^2 + \omega_2^2)} \Bigg\} \Bigg]\end{aligned} \tag{4.3}$$

where

$$\begin{aligned} A_r &= \left|\omega_o \{\hat{\eta}^{(r)}\}^T [M]^{-1} [C_s^{(r)}] \{\bar{\xi}_d\}\right| \\ B_r &= \left|\{\hat{\eta}^{(r)}\}^T [M]^{-1} [K_s^{(r)}] \{\bar{\xi}_d\}\right| \\ \omega_{d_r} &= \omega_r\sqrt{1-\zeta_r^2} \\ \omega_1 &= \omega_{d_r} - \omega_o \\ \omega_2 &= \omega_{d_r} + \omega_o \,. \end{aligned}$$

The modal analysis techniques developed in this thesis allow calculation of the response to disk displacement directly, without solution of the complete, coupled, time-dependent equations for the gas-bearing and slider body. The analytical form of the result, equation 4.3, shows how each of the individual modes participates in the total displacement solution. For the example of a 3370 slider and a typical disk surface displacement, the minimum clearance varies by approximately plus or minus 1.5 microinches during a complete rotation of the disk. The transient portion of the solution corresponds to the response of the slider to a ramp displacement of the disk surface. The minimum clearance during the transient portion of the solution decreases by nearly 4.5 microinches at the point of closest approach.

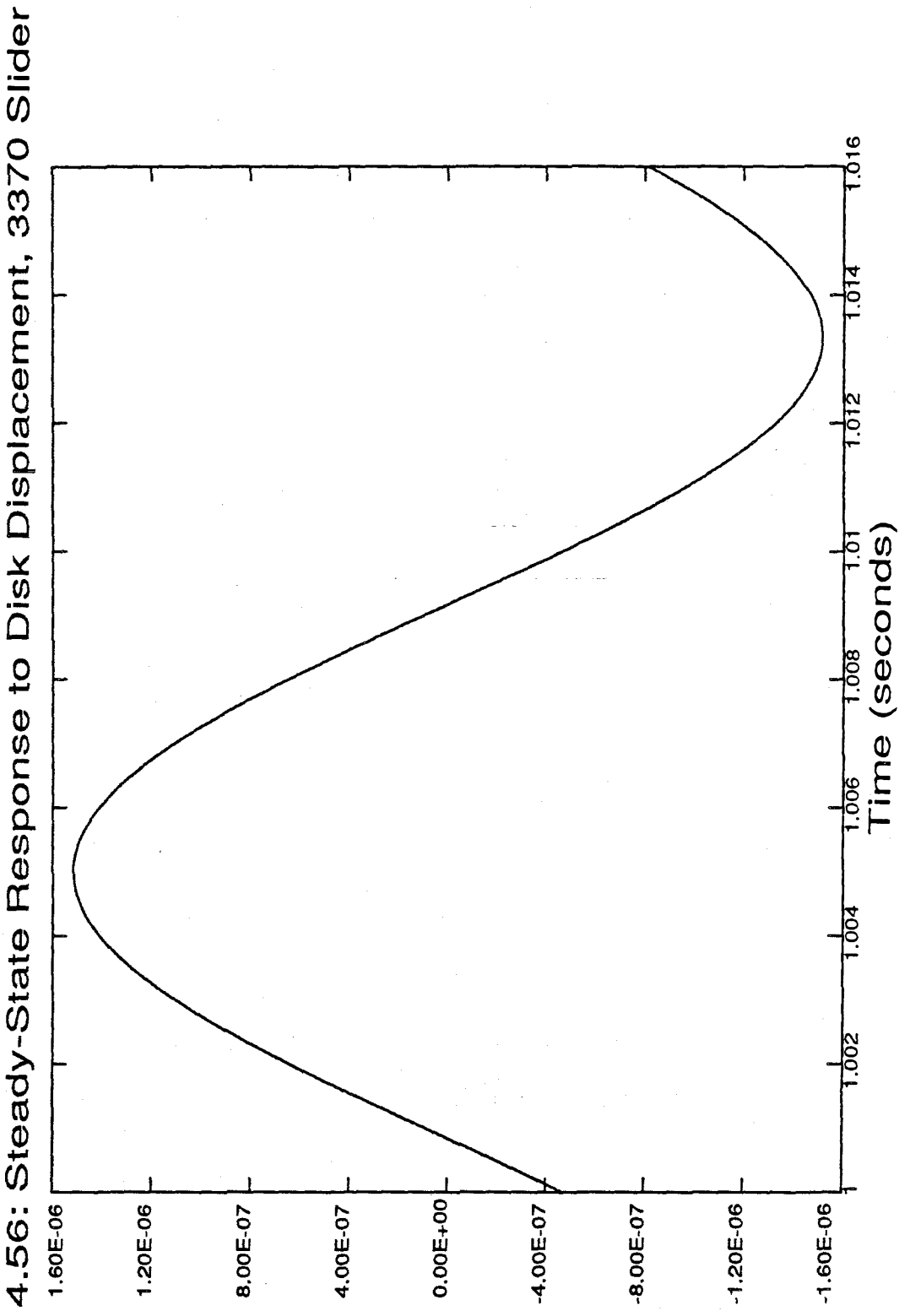

Figure 4.56: Steady-State Response to Disk Displacement, 3370 Slider

4.7 Summary

In this chapter, the perturbation and modal analysis techniques of Chapters 2 and 3 have been applied to several specific slider designs. Plane-wedge and taper-flat slider-pad geometries were compared for both static and dynamic performance as a function of minimum tail spacing, pitch angle, and yaw angle. The methods developed in this thesis were also applied to the IBM models 2314 and 3370 sliders, and the response of the latter slider to a displacement of the disk surface was computed using the forced response model.

The natural frequencies computed for the IBM model 3370 slider design showed good correlation with the values published by Miu (40). The present analysis also agreed with Miu's data in the identification of the uncoupled roll and the coupled pitch/heave modes.

Experimental observations of the taper-flat slider design, using optical interferometry, indicate incipient pitch instability at pitch angles greater than 300 microradians, and for yaw angles approaching 30 degrees. The methods presented in this thesis showed that the fraction of critical damping was greatly reduced for these conditions and thus could be used to predict the unstable behavior.

The IBM model 2314 slider design has been shown experimentally to exhibit good roll stability, but occasionally to fail by oscillating with a pitch/heave motion. The pressure distributions and the values of natural frequency and damping provided by the current method are in agreement with these observations.

As a design tool, the present method was found to be useful in ascertaining the effects of adding an inlet taper to the basic plane wedge slider geometry. Although the taper-flat slider pad was found to have slightly higher natural frequencies and fraction of critical damping, the inlet taper caused the center of rotation for the first coupled pitch/heave mode to move farther from the tail. The fraction of critical damping for the taper-flat design was also found to be more sensitive to increasing pitch angle than the plane-wedge pad, although both experienced a loss of damping with increasing yaw angle. The rotational centers for the coupled, pitch/heave modes of the taper-flat slider pad were more sensitive to tail spacing, pitch angle, and yaw angle than the plane wedge.

The modal analysis technique developed in this thesis provides a method for evaluating the dynamic performance of the slider-bearing system without the necessity of solving

the complete, coupled, time-dependent equations of motion for the slider body and the lubricating gas film. The values obtained for the fraction of critical damping in each mode, and for the center of rotation, are not obtainable with other methods, and have been shown to be useful for determining the dynamic stability of the slider design as well as the optimum location for the magnetic transducer.

CHAPTER 5

SUMMARY AND CONCLUSIONS

5.1 Summary of Current Work

In this thesis, a perturbation method has been developed that simplifies calculation of the dynamic characteristics of a slider-bearing system, while providing additional design information unobtainable with conventional time-domain solutions. Correlation has been established between the present analysis and published experimental data, as well as with analytical solutions for special limiting cases. The method has also been shown to predict experimentally observed instabilities in the Model 3370 and 2314 sliders.

In order to characterize the static and dynamic performance of the entire slider-bearing system, the influence of the lubricating gas film on the slider body must first be determined. In Chapter 2, the finite element method is used to solve Reynolds' equation for the pressure distribution in the gas bearing as a function of bearing geometry, lubricant properties, and operating conditions.

The weighted residual, or Bunov-Galerkin approach, is used for the finite element formulation. The gas bearing is discretized using eight-node, isoparametric, mapped elements and the nonlinear term in Reynolds' equation is replaced by the first two terms of a Taylor series expansion. The resulting iterative scheme shows good convergence, over a wide range of bearing numbers, for the static solution.

The dynamic characteristics of the gas bearing are determined using a linear perturbation of the slider about its equilibrium operating position. The perturbation pressure that results has components which are both in phase and out of phase with the perturbation in film geometry. Integration of the in-phase perturbation pressure over the surface of the slider gives rise to the stiffness matrix. The integral of the out-of-phase perturbation pressure similarly provides information for computation of the damping matrix. The linear, periodic perturbation used reduces the determination of the in-phase and out-of-phase pressure distributions to the solution of two coupled, second-order, linear partial differential equations containing terms that depend on the static solution of Reynolds' equation. These equations are written in partitioned matrix form and are solved non-iteratively by a single matrix inversion.

The solutions for stiffness and damping as a function of frequency have been examined for some limiting cases of special interest. When the present method is applied to the problem of the 1-D isothermal squeeze film, the results obtained show excellent agreement with the analytical results reported by Langlois. Analysis of the 1-D plane wedge slider at a high bearing number produced the interesting result that the damping goes to zero, and the stiffness is a function of pivot placement and inlet spacing only.

The development of the equations of motion and the formulation of the corresponding eigenproblem have been discussed in Chapter 3. The problem is made more difficult by the fact that the system exhibits general damping, and that it has non-symmetric stiffness and damping matrices which are frequency-dependent.

The damping is incorporated into the eigenproblem formulation by using generalized velocities as auxiliary variables and reformulating the equations of motion with 2N generalized coordinates. The resulting eigenvalues are complex and contain information on both the damped natural frequency and the fraction of critical damping in each mode.

The dynamical matrix resulting from the 2N space formulation is non-symmetrical. By using a similarity transformation based on both the left and the right modal matrices, the equations of motion are uncoupled. Each eigensolution represents the damped natural frequency, the fraction of critical damping, and the mode shape for one of the natural modes of the slider-bearing system. This information is not obtainable with existing methods.

Because the dynamical matrix is also frequency-dependent, the equations of motion are not completely uncoupled by the modal matrices composed of eigenvectors. For the cases examined in this thesis, however, the largest off-diagonal term is usually less than 10% of the smallest diagonal term, and the method provides reasonable results.

The uncoupled equations of motion for the forced problem are simple, first-order ordinary differential equations that are solved, in Chapter 3, for the case of periodic disk surface displacement, and for the case of a random force applied to the slider body.

The analytical techniques that have been developed here are applied to some common slider designs in Chapter 4. Data published by Miu for the IBM model 3370 slider, obtained with a laser-doppler vibrometer, show excellent correlation with the results obtained with the current model for the natural frequencies, and for the identification of the three principal

modes.

Results for the fraction of critical damping are found to be consistent with the experimentally observed behavior of several common slider designs. The taper-flat slider design has been found, using optical interferometry, to be unstable at large pitch angles, and the present analysis predicts this instability by means of a low fraction of critical damping in the coupled, pitch/heave mode of oscillation.

Yaw angles of 30 degrees or more also produce unstable behavior, according to experimental observations. Both plane-wedge and taper-flat slider pads were found, using the present techniques, to have very low damping under these conditions.

Using the eigenvectors for the two, coupled pitch/heave modes which that were identified for the plane-wedge and taper-flat slider pads, the center of rotation for slider oscillation has been computed. This information, which is not obtainable with other methods, is useful for determining the optimal location for the magnetic transducer in order to minimize variations in transducer/disk spacing.

The modal analysis methods presented here apply only to small, linearized displacement of the slider body from its equilibrium operating condition, and are only approximate because of the frequency dependence of the dynamical matrix. Nevertheless, the current techniques have been shown to agree well with experimentally observed behavior, and to provide information on modal damping, modal center of rotation, and the relationship of slider bearing geometry with stiffness and damping properties that cannot be obtained with existing methods.

5.2 Recommendations for Future Work

During the course of this research, several areas have been identified that warrant further investigation. A few of these are summarized below.

1) **Improved method for mean-free-path corrections to Reynolds' equation at high Knudsen numbers:** The correction attributed to Burgdorfer (51) has been used with good results for many years, but the higher Knudsen numbers of current slider designs require further improvements to the theory. Gans (55) has done some important recent work in this area.

2) **Use of upwinding method to improve static pressure solutions at high bearing**

number: At extremely high bearing numbers, the first-order terms of the Reynolds' equation dominate, and the equation can satisfy only the leading edge boundary condition. This results in an oscillatory pressure solution near the trailing edge. Hughes (77) has suggested a simple scheme for developing upwind finite elements, using a modified integration scheme for the high bearing number elements, thus showing some promise in reducing this oscillation while maintaining solution accuracy.

3) **Localized velocity in the static pressure solution:** As the overall diameter of disks used for magnetic storage becomes smaller, the variation in linear disk surface speed over the area of the slider-bearing pad becomes more significant. Taking this effect into account on an element-by-element basis would improve solutions for the newer configurations.

4) **Increase in the number of degrees of freedom for the dynamical model:** Experimental data from Miu (40) have shown the response of the 3370-style slider bearing to be composed principally of pitch rotation, roll rotation, and vertical translation. An increase in the number of degrees of freedom in the dynamical model might be of interest, particularly if bearing friction forces, and hence in-plane coupling of gas bearing and slider, were introduced into the model.

5) **Inclusion of gas-bearing frictional forces:** Using the velocity distributions computed in Chapter 2, it is relatively simple to compute the frictional forces exerted by the gas bearing on the slider body. The inclusion of these forces affects the torque generated about the pivot point, and thus may provide interesting additional information on the coupling between the gas bearing and the slider body.

6) **Improvements to the similarity transform used to decouple the equations of motion:** Further research may result in an improved method of dealing with the non-linearity of the eigenproblem and constructing the modal matrix for transforming the equations of motion.

7) **Inclusion of roughness effects for the disk surface:** Patir and Cheng (45); White, et al. (47); and Gans (50) have all contributed to the theory of surface roughness effects and the Reynolds' equation. These effects become more important as the slider-bearing spacing is reduced, and inclusion of roughness in the gas-bearing theory may improve accuracy at low clearances.

REFERENCES

I. EVOLUTION OF DISK DRIVE STORAGE SYSTEMS

1. Stevens, L. D., "The Evolution of Magnetic Storage," *IBM Journ. of Res. Dev.*, Vol. 25, No. 5, Sept. 1981, 663–675.

2. Harker, J. M., Brede, J. W., Pattison, R. E., Santana, G. R. and Taft, L. G., "A Quarter Century of Disk File Innovation," *IBM Journ. of Res. Dev.*, Vol. 25, No. 5, Sept. 1981, 677–689.

3. Bredin, H., "Tribology and the Design of Magnetic Storage Systems," *Mechanical Engineering*, March 1985, 80–83.

II. HISTORICAL DEVELOPMENT OF LUBRICATION THEORY

4. Petroff, N. P., "Friction in Machines and the Effect of the Lubricant," *Eng. Journ. St. Petersburg*, 1883, Vol. 1, 71–140; Vol. 2, 227–279; Vol. 3, 377–436; Vol. 4, 435–464.

5. Tower, B., "First Report in Friction Experiments," *Proc. Inst. Mech. Eng.*, Nov. 1883, 623–666; "Second Report," *ibid*, 1885, 58–70.

6. Reynolds, O., "On the Theory of Lubrication and Its Applications to Mr. Beauchamp Tower's Experiments Including an Experimental Determination of the Viscosity of Olive Oil," *Phil. Trans.*, Vol. 177 (i), 1886, 157–234.

7. Kingsbury, A., "Experiments with Air Lubricated Bearing," *Journ. of Amer. Soc. of Naval Engrs.*, Vol. 9, 1897.

8. Harrison, W. J., "The Hydrodynamical Theory of Lubrication with Special Reference to Air as a Lubricant," *Trans. Camb. Phil. Soc.*, Vol. 22, No. 3, 1913, 39.

9. Rayleigh, Lord, "Notes on the Theory of Lubrication," *Phil. Mag.*, Vol. 35, No. 1, 1918.

10. Pinkus, O., "The Reynold's Centennial: A Brief History of the Theory of Hydrodynamic Lubrication," *ASME Journ. of Trib.*, Paper 86-TRIB-22, 1986.

III. MODERN DEVELOPMENT OF LUBRICATION THEORY

General Numerical Techniques

11. Milne, A. A., "On the Effect of Lubricant Inertia in the Theory of Hydrodynamic Lubrication," *J. Appl. Mech.*, No. 81, 1958, 239–244.

12. Gross, W. A., "A Gas Film Lubrication Study: Part I, Some Theoretical Analyses of Slider Bearings," *IBM Journ. of Res. Dev.*, Vol. 3, No. 3, July 1959, 237–255.

13. Michael, W. A., "A Gas Film Lubrication Study: Part II, Numerical Solution of the Reynolds Equation for Finite Slider Bearings," *IBM Journ. of Res. Dev.*, Vol. 3, No. 3, July 1959, 256–259.

14. Elrod, H. G., "A Derivation of the Basic Equations for Hydrodynamic Lubrication with a Fluid Having Constant Properties," *Q. Appl. Math.*, Vol. 27, No. 4, 1960, 349–359.

15. Gross, W. A., **Gas Film Lubrication**, John Wiley and Sons, New York, 1962.

16. Michael, W. A., "Approximate Methods for Time-Dependent Gas-Film Lubrication Problems," *J. Appl. Mech.*, Dec. 1963, 509–517.

17. Castelli, V. and Stevenson, C. H., "Semi-Implicit Numerical Methods for Treating the Time-Transient Gas-Lubrication Equation," *ASME Journ. of Lubr. Tech.*, Paper 67-LUB-18, 1967.

18. Castelli, V. and Pirvics, J., "Equilibrium Characteristics of Axial-Groove Gas-Lubricated Bearings," *ASME Journ. of Lubr. Tech.*, April 1967, 177–196.

19. Coleman, R. L. and Snider, A. D., "Linearization for Numerical Solution of the Reynolds Equation," *Trans. ASME*, Paper 68-LUB-12, 1968, 1–2.

20. Castelli, V. and Pirvics, J., "Review of Numerical Methods in Gas Bearing Film Analysis," *ASME Journ. of Lubr. Tech.*, Vol. 90, No. 4, Oct. 1968, 777–792.

21. Fuller, D. D., "A Review of the State of the Art for the Design of Self-Acting Gas-Lubricated Bearings," *ASME Journ. of Lubr. Tech.*, Jan. 1969, 1–16.

22. Elrod, H. G. and McCabe, J. T., "Theory for Finite-Width High Speed Self-Acting Gas-Lubricated Slider (and Partial Arc) Bearings," *Journ. of Lubr. Tech.*, No. 91, 1969, 17–24.

23. Coleman, R. L., "A Brief Comparison of the Accuracy of Time-Dependent Integration Schemes for the Reynolds Equation," *ASME Journ. of Lubr. Tech.*, Vol. 94, No. 4, Oct. 1972, 330–334.

24. Tseng, R. C. and Talke, F. E., "Transition from Boundary Lubrication to Hydrodynamic Lubrication of Slider Bearings," *IBM Journ. of Res. Dev.*, No. 18, 1974, 534–540.

25. Tipei, N., "Flow Characteristics and Pressure Head Build-Up at the Inlet of Narrow Passages," *ASME Journ. of Lubr. Tech.*, Vol. 100, Paper 77-LUB-23, Jan. 1978, 47–55.

26. Gross, W. A., et al., **Fluid Film Lubrication**, John Wiley and Sons, New York, 1980 (extension and revision of 1962 work).

27. White, J. W. and Nigam, A., "A Factored-Implicit Scheme for the Numerical Solution of the Reynolds Equation at Very Low Spacings," *ASME Journ. of Lubr. Tech.*, Vol. 102, Jan. 1980, 80–85.

28. Rohde, S. M., "Computation Techniques in the Analysis and Design of Fluid Film Bearings," TRIBOLOGY, Chapter 6. Ed. A. Z. Srezi, 1981.

29. White, J. W., "Flying Characteristics of the 3370-Type Slider on a 5 1/4" Disk: Part I, Static Analysis," TRIBOLOGY AND MECHANICS OF MAGNETIC STORAGE SYSTEMS, ASLE Special Publication SP-16, 1984, 72–76.

30. Boncompain, R., Fillon, M. and Frene, J., "Analysis of Thermal Effects in Hydrodynamic Bearings," *ASME Journ. Lubr.*, Paper 85-TRIB-21, 1985.

31. Buckholz, R. H., "The Effect of Lubricant Inertia Near the Leading Edge of a Plane Slider Bearing," *ASME Journ. Trib.*, Paper 86-TRIB-32, 1986.

Dynamics and Stability Considerations

32. Lund, J. W., "Calculation of Stiffness and Damping Properties of Gas Bearings," *Journ. of Lubr. Tech.*, No. 90, 1968, 793.

33. Tang, T., "Dynamics of Air-Lubricated Slider Bearings for Non-Contact Magnetic Recording," *ASME Journ. of Lubr. Tech.*, Vol. 93, No. 2, April 1971, 272–278.

34. Ono, K., "Dynamic Characteristics of Air-Lubricated Slider Bearing for Non-Contact Magnetic Recording," *ASME Journ. of Lubr. Tech.*, Vol. 97, No. 2, April 1975, 250–260.

35. Ono, K., Kogure, K., and Mitsuya, Y., "Dynamic Characteristics of Air-Lubricated Slider Bearings Under Sub-Micron Spacing Conditions," *Bull. of JSME*, Vol. 22, No. 173, Nov. 1979, 1672–1677.

36. Tagawa, N., "Submicron Spacing of Air-Lubricated Slider in a Disk File with Swinging Arm Actuator," *IEEE Trans. Mag.*, Vol. Mag-17, No. 6, Nov. 1981, 2745–2747.

37. White, J. W., "Dynamic Simulation of the Zero-Load Slider Bearing," *IEEE Trans. Mag.*, Vol. Mag-19, No. 5, Sept. 1983, 1668–1670.

38. White, J. W., "Flying Characteristics of the 3370-Type Slider on a 5 1/4" Disk: Part II, Dynamic Analysis," TRIBOLOGY AND MECHANICS OF MAGNETIC STORAGE SYSTEMS, ASLE Special Publication SP-16, 1984, 77–84.

39. Bouchard, G., Miu, D. K., Bogy, D. B. and Talke, F. E., "On the Dynamics of Winchester and 3370-Type Sliders Used in Magnetic Recording Disk Files," TRIBOLOGY AND MECHANICS OF MAGNETIC STORAGE SYSTEMS, ASLE Special Publication SP-16, 1984, 85–89.

40. Miu, D. K., "Dynamics of Gas-Lubricated Slider Bearings in Magnetic Recording Disk Files; Theory and Experiment," Ph.D Thesis, UC Berkeley, May 1985.

41. Tagawa, N. and Hashimoto, M., "Submicron Spacing Dynamics for Flying Head Slider Mechanisms Using Building Block Approach," *IEEE Trans. Mag.*, Vol. Mag 21, No. 5, Sept. 1985, 1506–1508.

42. Mizoshita, Y., Aruga, K. and Yamada, T., "Dynamic Characteristics of a Magnetic Head Slider," *IEEE Trans. Mag.*, Vol. Mag-21, No. 5, Sept. 1985, 1509–1511.

43. Ohkubo, T., et al., "Accurate Measurement and Evaluation of Dynamic Characteristics of Flying Head Slider for Large-Capacity Fast-Access Magnetic Disk Storage," IEEE Intermag Conference, 1987, Tokyo, Japan.

44. Ponnaganti, V., Kane, T. R. and White, J. W., "Dynamics of Head-Disk Contact/Impact in Magnetic Recording," IEEE Intermag Conference, 1987, Tokyo, Japan.

Surface Roughness Effects

45. Patir, N. and Cheng, H. S., "An Average Flow Model for Determining Effects of Three-Dimensional Roughness on Partial Hydrodynamic Lubrication," *ASME Journ. Lubr.*, Vol. 100, Jan. 1978, Paper 77-LUB-17, 12–17.

46. Languirand, M. T. and Tichy, J. A., "The Effect of a Translating High Aspect Ratio Particle in a Plane Slider Bearing, " *ASME Journ. Lubr.*, Paper 82-LUB-13, 1982.

47. White, J. W., Raad, P. E., Tabrizi, A. H., Ketkar, S. P., and Prabhu, P. P., "A Numerical Study of Surface Roughness Effects on Ultra-Thin Gas Films," *ASME Journ. Trib.*, Paper 85-TRIB-6, 1985.

48. Oh, K. P., "The Formulation of the Mixed Lubrication Problem as a Generalized Nonlinear Complementarity Problem," *ASME Journ. Trib.*, Paper 85-TRIB-47, 1985.

49. Sun, D. and Chen, K., "First Effects of Stokes Roughness on Hydrodynamic Lubrication," *ASME Journ. Lubr.*, Paper 76-LUB-12, 1986.

50. Gans, R. F., "On Random Reynolds Roughness," *ASME Journ. Trib.*, Paper 86-TRIB-26, 1986.

Mean-Free-Path Corrections

51. Burgdorfer, A., "The Influence of Molecular Mean-Free Path on the Performance of Hydrodynamic Gas Lubricated Bearings," *J. Basic Eng.*, No. 81, 1959, 94–99.

52. Tseng, R. C., "Rarefaction Effects of Gas-Lubricated Bearings in a Magnetic Recording Disk File," *Journ. of Lubr. Tech.*, Vol. 97, No. 4, 1975, 624–629.

53. Sereny, A. and Castelli, V., "Numerical Solutions of Reynolds Equation with Slip Boundary Conditions for Cases of Large Bearing Number," *ASME Journ. of Lubr. Tech.*, Vol. 101, No. 1, Jan. 1979, 64–66.

54. Mitsuya, Y., "Molecular Mean Free Path Effects in Gas Lubricated Slider Bearings (An Application of the Finite Element Method)," *Bull. JSME*, Vol. 22, No. 167, June 1979, 863–870.

55. Gans, R. F., "Lubrication Theory at Arbitrary Knudsen Number," *ASME Journ. Trib.*, Vol. 107, No. 3, July 1985, 431–433.

56. Mitsuya, Y. and Ohkubo, T., "High Knudsen Number Molecular Rarefaction Effects in Gas-Lubricated Slider Bearings for Computer Flying Heads," *ASME Journ. Trib.*, Paper 86-TRIB-45, 1986.

Experimental Work

57. Brunner, R. K., Harker, J. M., Haughton, K. E., and Osterlund, A. G., "A Gas Film Lubrication Study: Part III, Experimental Investigation of Pivoted Slider Bearings," *IBM Journ. of Res. Dev.*, Vol. 3, No. 3, July, 1959, 260–274.

58. Briggs, R. B. and Herkart, P. G., "Unshielded Capacitor Probe Technique for Determining Disk Memory Ceramic Slider Flying Characteristics," *IEEE Trans. Mag.*, Vol. MAG 7, No. 3, Sept. 1971, 418–421.

59. Lin, C. and Sullivan, R. F., "An Application of White Light Interferometry in Thin Film Measurements," *IBM Journ. of Res. Dev.*, Vol. 16, No. 3, May 1972, 269–276.

60. Lin, C., "Techniques for the Measurement of Air-Bearing Separation: A Review," *IEEE Trans. Mag.*, Vol. MAG 9, No. 4, Dec. 1973, 673–677.

61. Fleischer, J. M., and Lin, C., "Infrared Laser Interferometer for Measuring Air-Bearing Separation," *IBM Journ. of Res. Dev.*, Vol. 18, No. 6, Nov. 1974, 529–533.

62. Sereny, A. and Castelli, V., "Experimental Investigation of Slider Gas Bearings with Ultra-Thin Films," *ASME Journ. of Lubr. Tech.*, Vol. 101, No. 4, Oct. 1979, 510–515.

63. Nigam, A., "A Visible Laser Interferometer for Air Bearing Separation Measurement to Submicron Accuracy," *ASME Journ. of Lubr. Tech.*, Vol. 104, No. 1, Jan. 1982, 60–65.

64. Hsia, Y. T. and Domoto, G. A., "An Experimental Investigation of Molecular Rarefaction Effects in Gas-Lubricated Bearings at Ultra-Low Clearances," *ASME Journ. of Lubr. Tech.*, Vol. 105, No. 1, Jan. 1983, 120–130.

65. Miu, D. K., Bouchard, G., Bogy, D. B., and Talke, F. E., "Dynamic Response of a Winchester-type Slider Measured by Laser Doppler Interferometry," *IEEE Trans. Mag.*, Vol. MAG 20, No. 5, Sept. 1984, 927–929.

66. Bouchard, G., Bogy, D. B., and Talke, F. E., "An Experimental Comparison of the Head/Disk Interface Dynamics in 5 1/4" and 8" Disk Drives," *IBM Journ. of Res. Dev.*, Vol. 29, No. 3, May 1985, 316–323.

67. Best, G. L., "Comparison of Optical and Capacitive Measurements of Slider Dynamics," 1987 IEEE Intermag Conference, Tokyo, Japan.

Special Slider Designs

68. Kogure, K., Fukui, S., Mitsuya, Y. and Kaneko, R., "Design of Negative Pressure Slider for Magnetic Recording Disks," *ASME Journ. Lubr. Tech.*, Vol. 105, July 1983, 496–500.

69. Yoneoka, S., et al., "Fast Take-Off Negative Pressure Slider," IEEE Intermag Conference, 1987, Tokyo, Japan.

IV. THE FINITE ELEMENT METHOD IN LUBRICATION THEORY

70. Reddi, M. M. and Chu, T. Y., "Finite Element Solution of the Steady-State Compressible Lubrication Problem," *ASME Journ. of Lubr. Tech.*, Paper 69-LUB-12, July 1970, 495–503.

71. Wada, S., Hayashi, H. and Migita, M., "Application of Finite Element Method to Hydrodynamic Lubrication Problems (Part I; Infinite Width Bearings)," *Bull. JSME*, Vol. 14, No. 77, 1971, 1222–1233.

72. Wada, S., Hayashi, H. and Migita, M., "Application of Finite Element Method to Hydrodynamic Lubrication Problems (Part II; Finite Width Bearings)," *Bull. JSME*, Vol. 14, No. 77, 1971, 1234–1244.

73. Booker, J. F. and Huebner, K. H., "Application of Finite Element Methods to Lubrication: An Engineering Approach," *ASME Journ. Lubr. Tech.*, Paper 72-LUB-N, Oct. 1972, 313–323.

74. Allaire, P. E., Nicholas, J. C. and Gunter, E. J., "Systems of Finite Elements for Finite Bearings," *ASME Journ. Lubr.*, Paper 76-LUB-13, 1976.

75. Christie, I., Griffiths, D. F., Mitchell, A. R. and Zienkiewicz, O. C., "Finite Element Methods for Second-Order Differential Equations with Significant First Derivatives," *Intl. Journ. Num. Meth. Engr.*, Vol. 10, 1976, 1389–1396.

76. Heinrich, J. C., Huyakorn, P. S., Zienkiewicz, O. C. and Mitchell, A. R., "An 'Upwind' Finite Element Scheme for Two-Dimensional Convective Transport Equations," *Intl. Journ. Num. Meth. Engr.*, Vol. 11, 1977, 131–143.

77. Hughes, T. J. R., "A Simple Scheme for Developing 'Upwind' Finite Elements," *Intl. Journ. Num. Meth. Engr.*, Vol. 12, 1978, 1359–1365.

78. Webster, W. D., "An Isoparametric Finite Element with Nodal Derivatives," *J. Appl. Mech.*, Vol. 48, Paper 81-APM-1, March 1981, 64–68.

79. Huebner, K. H. and Thornton, E. A., **The Finite Element Method for Engineers**, John Wiley and Sons, New York, 1982.

80. Payre, G., De Broissia, M. and Bazinet, J., "An 'Upwind' Finite Element Method via Numerical Integration," *Intl. Journ. Num. Meth. Engr.*, Vol. 18, 1982, 381–396.

81. Garcia-Suarez, C., Bogy, D. B. and Talke, F. E., "Use of an Upwind Finite Element Scheme for Air Bearing Calculations," Center for Magnetic Recording Research, UC San Diego, Tech. Report No. 3, Contract UCB ENG-5730, April 1984.

82. Garcia-Suarez, C., "Static and Dynamic Analyses of Gas Bearings Using Finite Elements," Center for Magnetic Recording Research, UC San Diego, Tech. Report No. 6, Contract UCB ENG-5730, Dec. 1984.

V. THE PERTURBATION METHOD

83. Gross, W. A. and Zachmanaglou, E. C., "Perturbation Solutions for Gas Lubricating Films," *J. Basic Eng.*, No. 83, 1961, 139–144.

84. Langlois, W. E., "Isothermal Squeeze Films," *Q. Appl. Mech.*, Vol. XX, No. 2, 1962, 131–150.

85. Nayfeh, A., **Perturbation Methods**, John Wiley and Sons, New York, 1973.

86. Sereny, A. and Castelli, V., "Perturbation Solution of the 1-D Reynolds Equation with Slip Boundary Conditions," *ASME Journ. of Lubr. Tech.*, Vol. 100, Jan. 1978, 70–73.

VI. MODAL ANALYSIS/UNCOUPLED EQUATIONS OF MOTION

87. Foss, K. A., "Co-Ordinates Which Uncouple the Equations of Motion of Damped Linear Dynamic Systems," *J. Appl. Mech.*, Vol. 25, 1958, 361–364.

88. Caughey, T. K., "Classical Normal Modes in Damped Linear Dynamic Systems," *J. Appl. Mech.*, Vol. 27, 1960, 269–271.

89. Caughey, T. K. and O'Kelly, M. E. J., "Classical Normal Modes in Damped Linear Dynamic Systems," *J. Appl. Mech.*, Vol. 32, Sept. 1965, 583–588.

90. Meirovitch, L., **Analytical Methods in Vibrations**, Macmillan, New York, 1967.

91. Lin, Y. K., **Probabilistic Theory of Structural Dynamics**, Robert E. Krieger, New York, 1967.

92. Kanianthra, J. N. and Speckhart, F. H., "A Technique for Determining Damping Values and Damper Locations in Multi-Degree-of-Freedom Systems," *ASME Journ. Engr. Ind.*, Paper 75-DET-83, 1975.

93. Smith, B. T., Boyle, J. M., Dongarra, J. J., Garbow, B. S., Ikebe, Y., Klema, V. C. and Moler, C. B., **Matrix Eigensystem Routines—EISPACK Guide**, Vol. 6 of Lecture Notes in Computer Science, Springer-Verlag, Berlin, 1976.

94. Jennings, A., **Matrix Computation for Engineers and Scientists**, John Wiley and Sons, Great Britain, 1977.

95. Press, W. H., Flannery, B. P., Teukolsky, S. A. and Vetterling, W. T., **Numerical Recipes—The Art of Scientific Computing**, Cambridge University Press, New York, 1986.